

University of New Hampshire

University of New Hampshire Scholars' Repository

Doctoral Dissertations

Student Scholarship

Spring 2020

Investigating the Spatial and Temporal Scale Variability of Ebullitive Flux from a Subarctic Thaw Pond System

Sophia Burke

University of New Hampshire, Durham

Follow this and additional works at: <https://scholars.unh.edu/dissertation>

Recommended Citation

Burke, Sophia, "Investigating the Spatial and Temporal Scale Variability of Ebullitive Flux from a Subarctic Thaw Pond System" (2020). *Doctoral Dissertations*. 2499.

<https://scholars.unh.edu/dissertation/2499>

This Dissertation is brought to you for free and open access by the Student Scholarship at University of New Hampshire Scholars' Repository. It has been accepted for inclusion in Doctoral Dissertations by an authorized administrator of University of New Hampshire Scholars' Repository. For more information, please contact Scholarly.Communication@unh.edu.

INVESTIGATING THE SPATIAL AND TEMPORAL SCALE VARIABILITY OF
EBULLITIVE FLUX FROM A SUBARCTIC THAW POND SYSTEM

BY

SOPHIA A. BURKE

B.Sc. Environmental Science: Ecosystems, University of New Hampshire, 2013

DISSERTATION

Submitted to the University of New Hampshire

in Partial Fulfillment of

the Requirements for the Degree of

Doctor of Philosophy

in

Earth and Environmental Sciences

May, 2020

This dissertation was examined and approved in partial fulfillment of the requirements for the degree of Doctor of Philosophy in Earth & Environmental Sciences by:

Dissertation Director, Dr. Ruth K. Varner, Professor of Biogeochemistry, Department of Earth Sciences and Earth Systems Research Center

Dr. Michael W. Palace, Associate Professor of Earth Sciences, Department of Earth Sciences and Earth Systems Research Center

Dr. Wilfred M. Wollheim, Associate Professor of Natural Resources and the Environment, Department of Natural Resources and The Environment

Dr. Stephen E. Froking, Research Professor of Earth Sciences, Department of Earth Sciences and Earth Systems Research Center

Dr. Patrick Crill, Professor of Biogeochemistry, Department of Geological Sciences, Stockholm University

On April 30, 2020

Approval signatures are on file with the University of New Hampshire Graduate School.

TABLE OF CONTENTS

TABLE OF CONTENTS	III
LIST OF FIGURES	VI
LIST OF TABLES	XI
ACKNOWLEDGEMENTS	XIII
ABSTRACT	XV
CHAPTER	PAGE
INTRODUCTION	1
I. BACKGROUND.....	1
II. HYPOTHESES.....	4
III. SUMMARY.....	7
CHAPTER 1: LONG TERM MEASUREMENTS OF METHANE EBULLITION FROM THAW PONDS ...	11
1.1 ABSTRACT	11
1.2 PLAIN LANGUAGE SUMMARY	12
1.3 INTRODUCTION.....	13
1.4 METHODS.....	16
1.4.1 Study Site.....	16
1.4.2 Pond Sites.....	18
1.4.3 Ebullition sampling	24
1.4.4 Pond water temperature and meteorological variable collection.....	25
1.4.5 Data processing and analysis	25
1.5 RESULTS	27
1.5.1 Variation in daily bubble flux among ponds.....	27
1.5.2 Monthly and seasonal variation in daily bubble flux	30

1.6 DISCUSSION	33
1.6.1 Spatiotemporal variability in ebullitive emission across ponds.....	33
1.6.2 Pond emissions compared to other sub-habitats	37
1.7 CONCLUSIONS	40
1.8 ACKNOWLEDGMENTS, SAMPLES, AND DATA.....	41

CHAPTER 2: USING UNMANNED AERIAL SYSTEMS TO MONITOR THE CHANGE IN THAW POND SIZE OVER FIVE GROWING SEASONS: IMPLICATIONS FOR CH₄ EBULLITIVE FLUX 43

2.1 INTRODUCTION.....	43
2.2 METHODS.....	46
2.2.1 Study Site.....	47
2.2.2 Measurements of Methane Ebullition from Thaw Ponds.....	47
2.2.3 Imagery Collection.....	49
2.2.4 Orthorectification	51
2.2.5 Georectification	52
2.2.6 Pond Edge Polygons and Water Polygons	53
2.2.7 Statistical Analysis.....	54
2.3 RESULTS	56
2.3.1 Spatial Variability in Pond Area	56
2.3.2 Seasonal Variability in Water Polygon Area.....	58
2.3.3 Fixed Wing vs. Quadcopter Platforms: Water Polygon Area	61
2.3.4 Interannual Variability in Pond Edge Area	62
2.3.5 Pond Area and Ebullitive CH ₄ Emissions	65
2.4 DISCUSSION	71
2.4.1 Using UAS platforms to monitor pond size over time.....	71
2.4.2 Interannual variability in thaw pond size and its impact on CH ₄ emissions.....	74
2.5 CONCLUSIONS	76

CHAPTER 3: USING ACOUSTIC TECHNIQUES TO MONITOR CH₄ EBULLITION IN SUBARCTIC

THAW PONDS.....78

3.1 INTRODUCTION.....78

3.2 METHODS.....80

3.2.1 Field Site81

3.2.2 Monitoring CH₄ ebullition.....83

3.2.3 Laboratory Testing and Calibration85

3.2.4 Acoustic Data Processing and Analysis86

3.2.5 Statistical Analysis.....91

3.3 RESULTS93

3.3.1 Meteorological drivers of CH₄ emissions.....93

3.3.2 Spatial and Temporal variability in bubble detection by trap.....98

3.4 DISCUSSION103

3.4.1 Drivers of CH₄ ebullition103

3.4.2 High resolution monitoring of CH₄ ebullition.....105

3.5 CONCLUSIONS107

LIST OF REFERENCES109

APPENDIX A: CHAPTER 1 SUPPLEMENTARY MATERIALS.....124

A.1 INTRODUCTION.....124

APPENDIX B: CHAPTER 2 SUPPLEMENTARY MATERIALS.....139

APPENDIX C: CHAPTER 3 SUPPLEMENTARY MATERIALS.....152

LIST OF FIGURES

CHAPTER FIGURES	PAGE
Figure i. 1 Schematic showing varying spatial and temporal resolution of sampling techniques	5
Figure 1.1. Orthomosaic image of the Stordalen Mire in northernmost Sweden	18
Figure 1.2 Daily bubble flux ($\text{mg CH}_4 \text{ m}^{-2} \text{ d}^{-1}$) and pond temperature ($^{\circ}\text{C}$) from selected ponds	29
Figure 1.3 Boxplots of all measurements collected over four sampling seasons.....	30
Figure 2.1 Modified from Burke et al. (2019) (Figure 1.1). Orthomosaic image of Stordalen Mire, Sweden ($68^{\circ}22'\text{N}$, $19^{\circ}03'\text{E}$) with pond sites marked.....	50
Figure 2.2 Orthomosaic of Pond F (panel A) with pond edge polygon overlaid (panel B) and water polygon overlaid (panel C).....	54
Figure 2.3 Pond edge area (A.) and water polygon area (B.) of ponds from quadcopter UAS imagery.....	57
Figure 2.4 Variability in water polygon area among months	59
Figure 2.5 Variability in water polygon area (m^2) across the sampling season (day of year).....	60
Figure 2.6 Comparison of pond edge polygon area from fixed-wing imagery collected in July to the average pond edge polygon area.....	62
Figure 2.7 Variability in pond edge polygon area among different sampling seasons from both quadcopter and fixed wing imagery.....	63

Figure 2.8 Variability in pond edge area by sampling season from both quadcopter and fixed wing imagery. 64

Figure 2.9 Modified from Burke et al. (2019) (Figure 1.3). Median daily ebullitive flux calculated across an eight-day moving window that is centered around each flight date during the 2016 – 2018 sampling seasons. 66

Figure 2.10 Water polygon area from quadcopter imagery among the different pond types. 68

Figure 2.11 Water polygon area of differing pond types by month. 69

Figure 2.12 Median pond edge area (m²) compared to median annual ebullitive flux (mg CH₄ m⁻² d⁻¹) of the seven ponds in this study. 70

Figure 3.1 Modified from Burke et al. (2019) (Figure 1.1). A.) Aerial image of Stordalen Mire with ponds H and C outlined in orange. 82

Figure 3.2 Diagram of acoustic bubble trap system deployed in pond C and pond H. .. 84

Figure 3.3 Number of detections across the different time bins (sec) of the detection dataset after initial filtering (zero detections removed). 89

Figure 3.4 Time series of two-hour averages (apart from total precipitation, which is two-hour totals) of all meteorological variables 96

Figure 3.5 Scatterplots showing the relationship between bubble detections and A.) T_{air}, B.) SWR, and C.) predicted bubble detections 97

Figure 3.6 Violin plot showing the distribution of bubble detections measured on a daily basis between traps 98

Figure 3.7 Time series of total bubble detections every two hours and the volume of gas collected in mL.....	100
Figure 3.8 Diel variability in average bubble detections and SWR, T_{air} , and WS on an hourly basis across the study period	102
APPENDIX A FIGURES	PAGE
Figure A.1 Images of each pond measured in this study	126
Figure A.2 Measured daily CH ₄ emissions (mg m ⁻² d ⁻¹) for each pond at the Stordalen Mire, Abisko Sweden. (Supplementary Figure S2 in Burke et al., 2019).....	127
Figure A.3 Measured daily CH ₄ flux from ponds B, C, E, and H respectively during the 2014 field season compared to pond temperature (°C), and atmospheric pressure (mbar)	128
Figure A.4 Measured daily CH ₄ flux from ponds B, C, E, and H respectively during the 2015 field season compared to pond temperature (°C), and atmospheric pressure (mbar)	129
Figure A.5 Boxplot of variability in daily bubble flux (mg CH ₄ m ⁻² d ⁻¹) between months.	130
Figure A.6 Boxplot of variability in daily bubble flux (mg CH ₄ m ⁻² d ⁻¹) between sampling seasons.	131
Figure A.7 Boxplot of variability in daily bubble flux (mg CH ₄ m ⁻² d ⁻¹) for each pond within months.	132
Figure A.8 Boxplot of variability in daily bubble flux (mg CH ₄ m ⁻² d ⁻¹) within ponds between sampling seasons.	133

APPENDIX B FIGURES

PAGE

Figure B.1 Comparison of Contour line delineation of ponds using digital elevation models created using AgiSoft Photoscan. 139

Figure B.2 Water polygon area (m²) of each pond in the study compared to the total precipitation accumulation (mm) in the eight days leading up to the UAS flight. 140

Figure B.3 Relationship between water polygon area and total precipitation accumulation before flight separated by pond. 141

Figure B.4 Water Polygon area of quadcopter imagery collected during the growing season at Stordalen Mire during the 2016, 2017 and 2018 growing seasons, separated by month. 142

Figure B.5 Comparison of water polygon area measured from fixed wing imagery collected in July compared to the average water polygon area measured from quadcopter imagery collected throughout the growing season 143

Figure B.6 Pond edge polygon area from quadcopter imagery among the different pond types. 144

Figure B.7 Pond edge area of differing pond types by sampling season from imagery collected using the quadcopter UAS and fixed wing airplane. 145

Figure B.8 Annual ebullitive flux (mg CH₄ m⁻²) compared to pond edge area (m²) from both quadcopter and fixed wing imagery of the seven ponds in this study. 146

Figure B.9 Updated boxplots from Burke et al. (2019) to include all of the ebullitive measurements collected between 2012-2018 represented as daily bubble flux (mg CH₄ · m⁻² · day⁻¹). 147

Figure B.10 Updated boxplots from Burke et al. (2019) of variability in daily bubble flux
($\text{mg CH}_4 \text{ m}^{-2} \text{ d}^{-1}$) between months collected 2012-2018 sampling seasons. 148

Figure B.11 Updated boxplots from Burke et al. (2019) showing the variability in daily
bubble flux ($\text{mg CH}_4 \text{ m}^{-2} \text{ d}^{-1}$) between sampling seasons. 149

APPENDIX C FIGURES **PAGE**

Figure C.1 MATLAB spectrogram of the raw data (A.) and the magnitude of the 99th
quantile (dB) (B.) from a six-minute acoustic file 153

Figure C.2 Time series of bubble detected on a ten-minute timescale between 14 June
and 16 June, 2018 154

Figure C.3 Time series of bubble detected on a ten-minute timescale between 27 June
and 29, June, 2018 155

Figure C.4 Timeseries of cumulative bubble detections (solid line) and cumulative
volume collected 156

Figure C.5 Scatterplot showing the relationship between bubble detections and average
WS (m s^{-2}). 157

LIST OF TABLES

CHAPTER TABLES	PAGE
Table 1.1 Characteristics of ponds sampled at Stordalen mire.....	21
Table 1.2 Temporal and spatial variability in CH ₄ bubble flux.....	32
Table 1.3 Summary of meteorological data across the study period	33
Table 2.1 Modified Table from Burke et al. (2019) (Table 1.1). Physical characteristics of ponds sampled at Stordalen Mire, Abisko, Sweden between 2016 – 2018.....	49
Table 3.1 Summary of acoustic detections from the 2018 sampling season that occurred more than half a second apart after filtering out noise due to sampling and precipitation events.....	90
Table 3.2 Summary of measured meteorological data during the study period: 6 June – 8 August 2018.....	94
Table 3.3 Summary of the minimum, maximum, mode and cumulative of bubble detections on a daily scale for each month in the 2018 sampling season.....	99
APPENDIX A TABLES	PAGE
Table A.1 Pond water table depth (WTD, cm) and dissolved oxygen (DO, mg L ⁻¹) from 22 July 2013 and from the average of weekly surveys conducted during 2014 field season.	134
Table A.2 Association between SWR, T _{air} , T _{pond} , and ΔP ₅ on ebullitive flux using Kendall’s rank correlation test. (Supplementary Table S2 in Burke et al., 2019)....	134
Table A.3 Pairwise comparisons across months within each pond	135

Table A.4 Pairwise comparisons across ponds within months	136
Table A.5 Pairwise comparisons across sampling seasons within ponds	137
Table A.6 Pairwise comparisons across ponds within sampling seasons from a Dunn's Test following the Bonferroni method ($\alpha = 0.05$).....	138

APPENDIX B TABLES

PAGE

Table B.1 Table of mean tie point residuals for each image collected with the quadcopter during the 2016,2017 and 2018 field seasons.....	150
Table B.2 Monthly summary of meteorological variables for 2016 - 2018.	151

APPENDIX C TABLES

PAGE

Table C.1 Generalized linear mixed effects results for models 1-5.....	158
Table C.2 Linear model results for models 6.	159

ACKNOWLEDGEMENTS

I would like to thank first and foremost my advisor Ruth Varner for being an incredible mentor and friend throughout my undergraduate and graduate schooling. You provided me and so many others with the opportunity to work and learn in the ever welcoming and supportive Trace Gas Biogeochemistry Lab. You have brought me along on some amazing adventures in Sweden, Finland and Northern Canada and encouraged me to go out on my own to New Zealand and Brazil, each experience teaching me so much about myself as a person and as a scientist. I would not have ventured out with such an open heart and mind if not for your encouragement. I would like to thank my committee members Michael Palace, Steve Frolking, Wil Wollheim and Patrick Crill for their support and encouragement during my dissertation. I would also like to thank Alix Contosta, fellow lead of the Trace Gas Biogeochemistry Lab, for being so key in my enjoyment of coding and understanding of statistical analyses necessary for this work. I would like to acknowledge the Swedish Polar Research Secretariat and Abisko Scientific Research Station in Abisko, Sweden, in particular Niklas Rakos and Annika Kristoffersson, for providing logistical support, housing, laboratory space, field assistance that was essential for the completion of this work. I would also like to acknowledge the Sweden Integrated Carbon Observation System (ICOS), in particular Jutta Holst, for providing meteorological data. A special thanks to the IsoGenie Project for providing a space on their database for archiving the data collected and code produced during this dissertation project. Thank you to Dawn Zitney, Wellness Educator at UNH, for being an integral part of my wellness journey throughout graduate school.

And lastly a very special shout out to my dear friends and family for cheering me on during this wild ride. I love you all more than I can say.

This work has been funded in part by the following grants: the Northern Ecosystems Research Experience for Undergraduates program (NERU – REU site EAR#1063037, PI Varner); NSF Macrosystems Biology grant (NSF EF #1241037, PI Varner); NASA IDS grant (NASA IDS #NNX17AK10G, PI Varner); the Genomic Science Program of the United States Department of Energy Office of Biological and Environmental Research, Grants (DE-SC0010580 and DE-SC0016440); the University of New Hampshire Dissertation Year Fellowship; the New Hampshire Space Grant Consortium (NASA Grant # NNX15AH79H); a grant from University of New Hampshire’s Hamel Center for Undergraduate Research SURF-Abroad program; and a grant from the Malmberg Scholarship Program which is supported by the endowment established by Cornelia Malmberg through a generous bequest from her estate.

ABSTRACT

INVESTIGATING THE SPATIAL AND TEMPORAL SCALE VARIABILITY OF EBULLITIVE FLUX FROM A SUBARCTIC THAW POND SYSTEM

By

Sophia A. Burke

University of New Hampshire

Arctic regions are experiencing more rapid warming than other parts of the world, leading to destabilization of carbon (C) that has been sequestered in permafrost, especially in peatlands where the C content of the peat is very high. More frequent incidence of thaw in permafrost peatlands is leading to the development of small thaw ponds that are known to be sources of methane (CH₄) to the atmosphere, yet there is a lack in long-term studies of CH₄ emission from these formations. This is of concern because CH₄ has thirty-two times the global warming potential of carbon dioxide over a one-hundred-year timescale (Holmes et al., 2013). At a site in northern Sweden, we have collected over 3000 measurements of CH₄ ebullition, or bubbling, from eight small thaw ponds (<0.001 km²) differing in physical and hydrological characteristics over seven growing seasons (2012-2018).

We found ebullitive emission to be highly variable over space and time, with an average emission rate of 21.9 mg CH₄ m⁻² d⁻¹. Between 2012 and 2015, ebullitive emission was weakly correlated with environmental conditions like atmospheric

pressure and temperature and potentially more influenced by the physical characteristics of the ponds themselves. Based on their rates of daily ebullitive emission, the ponds fell into four statistically significant groups which appeared to differ from each other based on physical characteristics among the ponds within each group. This grouping, further called pond types, distinguishes ponds from one another based on vegetation presence, pond depth, and hydrologic connectivity to neighboring fen areas (or lack there-of). Type 1, with the lowest daily ebullitive emissions measured, are the shallowest ponds, they are hydrologically isolated have low instances of sedge vegetation (*Carex spp.* and *Eriophorum spp.*) and have *Sphagnum spp.* mosses present within them. Type 2 ponds, which emit more ebullitive CH₄ than type 1, are deeper, have more sedge vegetation present and are hydrologically isolated. Type 3 ponds are this highest emitting on a daily scale and are the deepest, with more sedge vegetation present than type 3 yet remain hydrologically isolated. Type 4, are shallower than type 3, have no *Sphagnum spp.* present, are surrounded by sedge vegetation and connected to a neighboring fen area allowing water to flow. Based on our findings, and the available literature, we estimate that small ponds (< 0.001 km²) emit between 0.2 and 1.0 Tg of CH₄ through ebullition over an estimated 149 ice-free days. Using acoustic techniques, we determined that on a sub-daily timescale CH₄ emission rates varied significantly over space and time within a single pond with diel variability in bubbling rate following that of air temperature, shortwave radiation and wind speed. Using remotely collected imagery from an unmanned aerial system (UAS) platform of seven ponds collected over five sampling seasons (2014 — 2018) we found pond edge and water

area varied significantly between ponds as well as over time, with water area varying significantly between pond types. Annual ebullitive flux was highest in ponds that ranged in pond edge area of 50 – 150 m² with smaller and larger ponds emitting less, however this relationship is likely more related to physical differences between the ponds, rather than differences in overall size.

This work supports the importance of long-term studies that take advantage of a range of spatial and temporal scale sampling techniques in order to adequately capture the variability in CH₄ ebullition from these highly dynamic formations. Not only are high resolution measurements of CH₄ ebullition important, but the tandem monitoring of pond size and other physical characteristics that distinguish ponds from one another are also important to better understand the observed CH₄ emissions. With an increase in the number of long-term studies such as this, we will be better able to model CH₄ emissions from thawing permafrost ecosystems in the future.

INTRODUCTION

I. Background

Peatlands in the northern hemisphere contain large amounts of soil carbon (C) due to saturated conditions and low temperatures that result in slow rates of decomposition (Gorham, 1991). Peatlands are estimated to contain 50% of the world's organic C (Tarnocai et al., 2009) with those in the northern hemisphere containing an estimated 547 GtC of soil organic carbon (OC) (Yu et al., 2010). At high latitudes, much of this high C content soil or peat is located in permafrost regions where the ground is permanently frozen further stabilizing this C. Over the past several decades, rising atmospheric temperatures have led to increased thawing in permafrost regions, resulting in the liberation of C for decomposition into carbon dioxide (CO₂) and methane (CH₄) (Callaghan et al., 2010; Schuur et al., 2008; Stocker et al., 2013). Though CO₂ is the most studied radiatively important trace gas and is responsible for much of the observed atmospheric warming, recent studies have shifted the focus to CH₄ due to its much stronger global warming potential (thirty-two times that of CO₂; Holmes et al., 2013).

Methane is produced only in anoxic environments, and therefore is the least energetic way to decompose organic matter (Bell, 1969). Once CH₄ is formed belowground, it can then be released to the atmosphere via three important transport mechanisms: diffusion through the saturated peat, plant mediated transport, and ebullition or bubbling (Bastviken et al., 2011; Coulthard et al., 2009; Fechner-Levy &

Hemond, 1996), with ebullition considered an important yet the least understood pathway (Coulthard et al., 2009; Walter et al., 2006). Ebullition has been observed to occur in at least two modes: low background bubbling that occurs on a more or less constant level (Goodrich et al., 2011) and more irregular episodic events that are larger in volume and can be more difficult to monitor (Rosenberry et al., 2003). Episodic ebullition events are often triggered by environmental conditions such as changes in hydrostatic pressure due to decreasing water level and/or atmospheric pressure or varying levels of incoming solar radiation (Goodrich et al., 2011; Weyhenmeyer, 1999; Wik et al., 2014).

Wetlands are the largest natural source of CH₄ to the atmosphere (Saunois et al., 2016) and in high latitude regions, permafrost thaw can result in CH₄ emissions by giving rise to the formation of small ponds and lakes due to the slumping and degradation of peat surfaces and subsequent filling with water (Bouchard et al., 2014; Negandhi et al., 2013; O'Donnell et al., 2011). Very small ponds (surface area < 0.001 km²), formed by thermokarst in permafrost regions, have been studied in various subarctic and Arctic areas (e.g. Hamilton et al., 1994; Shirokova et al., 2013). They comprise less than 9% of the area covered by lakes and ponds globally yet they account for over 40% of the hydrodynamically driven diffusive CH₄ emissions from these water bodies (Holgerson & Raymond, 2016). A review of both ebullitive and diffusive emissions from lakes and ponds located above 50°N found that small ponds are a significant source of CH₄ for the northern latitudes (Wik, Varner et al., 2016). However, few of the reviewed studies focused on ebullition (Hamilton et al., 1994) and even fewer

presented multiple seasonal measurements (Laurion et al., 2010) therefore further study of ebullitive flux from small ponds are needed to provide quantitative understanding of the emissions and any feedbacks to warming of these ecosystems.

Vegetation shifts and hydrologic change associated with pond formation has direct effects on C cycling in permafrost ecosystems. The increased wetness observed due to the thawing of permafrost peat (O'Donnell et al. 2011) can provide new habitat for plants that have an affinity for wetter conditions such as *Eriophorum angustifolium* Honck., *Carex rostrate* Stokes (Malhotra & Roulet, 2015; Malmer et al., 2005) and *Sphagnum* mosses. A common initial colonizer of thawed, wetter areas are *Sphagnum* spp. mosses because they generally prefer lower pH and low nutrient conditions in the absence of flowing water (Gignac et al. 1991; Glaser, Hansen et al., 2004; Vitt & Slack, 1975). Water bodies can then be colonized with sedges (Camill, 1999; Tuittila et al., 2013; Vitt & Slack, 1975). Continued thaw and consequent increase in the size of wet areas can also lead them to them becoming connected to already wet surrounding fens and thus introduce a flow component into these systems (Olefeldt & Roulet, 2012). Changes in vegetation composition have been observed with concomitant increases in CH₄ emissions (Johansson et al., 2006; King et al., 1998; Kutzbach et al., 2004) because vascular plants, such as sedges, colonize newly thawed areas and can become conduits for CH₄ to bypass the oxidation, or CH₄ consumption, zone (Chanton, 2005; Noyce et al., 2014) as well as provide newly fixed C as substrate for methanogenesis (Moore et al., 2011; Wilson et al., 1989). Changes in vegetation and hydrology due to permafrost thaw will impact the production rates and emission of CH₄

and therefore need to be taken into account when modeling these changing ecosystems.

Remote sensing technology offers a unique opportunity to monitor changes in water body size using repeat measurements that could help identify transitions over time. The use of remote sensing in ecological research has increased in recent years due to its enhancement of spatial and temporal resolution (Chambers et al., 2007; Palace et al., 2018). However, remote sensing, particularly using satellites, has limitations due to spatial resolution (Anderson & Gaston, 2013). For example, many satellite platforms have a spatial resolution too large to see water bodies smaller than 0.1 ha (Muster et al., 2012) making them difficult to use in studying temporal changes in thaw ponds. Unmanned aerial systems (UAS), also known as drones, have offered a potential steppingstone between ground-based measurements and satellite imagery due to their much higher spatial resolution (Anderson & Gaston, 2013; Marris, 2013).

II. Hypotheses

The goal of my dissertation research is to better understand the controls on CH₄ emissions from small ponds in permafrost ecosystems and how these features change over time by specifically addressing the following hypotheses (Figure i. 1):

***H1.** Variability in physical characteristics of small ponds (depth, hydrology, sedge dominance) will drive variability in ebullitive flux on a daily and seasonal basis more so than meteorological variability (Chapter 1).*

H2. Remotely sensed pond edge and water area of thaw ponds will vary in response to episodic precipitation events, seasonally and interannually relating to differences in pond type (see H1) (Chapter 2).

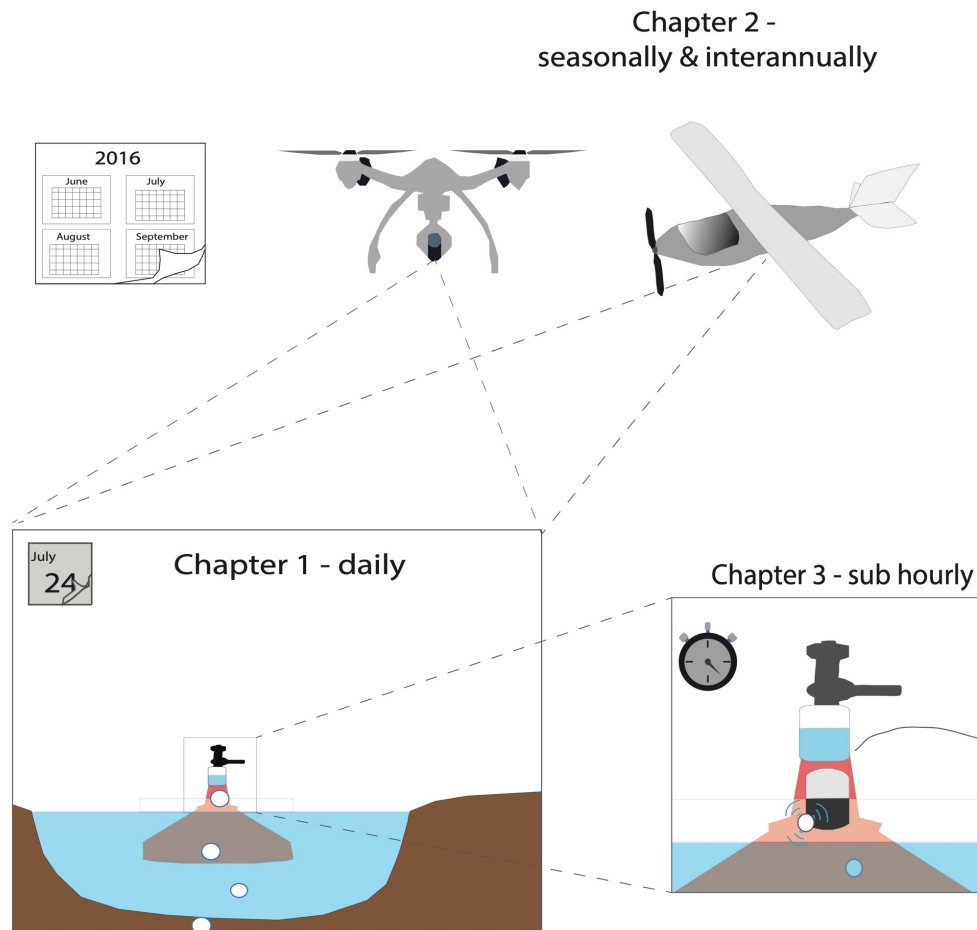


Figure i. 1 Schematic showing varying spatial and temporal resolution of sampling techniques used in each chapter of the dissertation. Chapter 1 focuses on sampling on a daily basis using simple floating funnels, Chapter 2 focuses on seasonal and interannual variability using drone imagery, while Chapter 3 focuses on sub-hourly sampling using hydrophones.

H3. Sub-daily emissions of CH_4 via ebullition will vary spatially and temporally within ponds. Diel fluctuations of emissions within a measurement location will vary according to diel fluctuations in air temperature, incoming solar radiation and wind speed. (Chapter 3).

My dissertation chapters have been formatted for submission to peer-reviewed journals. These three hypotheses have been addressed through the collection of manual measurements of ebullitive CH₄ from eight thaw ponds with bubble traps installed at Stordalen Mire over four field seasons and are discussed in Chapter 2 (H1; Burke et al., 2019). Remotely sensed data collected using UAS technology was used to assess the changes in pond and water area size over time in Chapter 2 (H2). Two of the thaw ponds were equipped with acoustic systems and were used to determine drivers of ebullitive flux on a high temporal scale in Chapter 3 (H1 and H3). As of May 2020, the first chapter of this dissertation has been published in AGU's Journal of Geophysical Research: Biogeosciences. Chapter 2 is in preparation for submission to Remote Sensing of the Environment. Chapter 3 is in preparation for submission to either Hydrology & Earth System Science or Environmental Science & Technology pending co-author comment. The citations for the chapters included in this dissertation are as follows:

1. Burke, S. A., Wik, M., Lang, A., Contosta, A. R., Palace, M., Crill, P. M., & Varner, R. K. (2019). Long-Term Measurements of Methane Ebullition from Thaw Ponds. *Journal of Geophysical Research: Biogeosciences*, 2018JG004786. <https://doi.org/10.1029/2018JG004786>
2. Burke, S. A., Palace, M., Contosta, A. R., Perryman, C., Bennett, K., Rocci, K., Herrick, C., Crill, P. M., & Varner, R. K. In prep. Using unmanned aerial systems to monitor the change in thaw pond size over five growing seasons: Implications for CH₄ ebullitive flux. *Remote Sensing of the Environment*.

- Burke, S. A., Palace, M., Perry, A., Padilla, A., Herrick, C., Contosta, A. R., Weber, T., Crill, P. M., & Varner, R. K. In prep. Using acoustic techniques to monitor methane ebullition in subarctic thaw ponds. *Hydrology & Earth System Science or Environmental Science & Technology*.

The data presented in this dissertation, along with the code used for data processing and analysis will be made available on the IsoGenie project data repository (<https://isogenie-db.asc.ohio-state.edu/index>). Data associated with Chapter 1 is already available online at the data repository (<https://isogenie-db.asc.ohio-state.edu/datasources#fluxes>). Any questions regarding data the data presented in this dissertation can be directed to Sophia Burke (sophieaburke@gmail.com).

III. Summary

This work represents a unique pairing of long-term, high-resolution data using several sampling methodologies that when combined provide insight to the varying spatial and temporal dynamics of CH₄ ebullition in a changing and vulnerable ecosystem. Presented here is a dataset of ebullitive emissions from thaw ponds with over 3000 manual measurements over seven sampling seasons of ebullitive emissions collected on a daily to weekly basis (84% of which were collected within 1–3 days). From 2012-2018, the daily average ebullitive rate of CH₄ from eight ponds was 21.9 mg CH₄ m⁻² d⁻¹. Non-parametric statistical analyses were used to interpret significant relationships in the data. On a daily basis, ebullitive emissions varied significantly by

pond, with the eight ponds falling into four statistically significant groups using non-parametric statistical tests; Kruskal -Wallis sums test for variability and the Dunn's test to determine pairwise comparisons. These groups, further called types, appeared to differ from each other based on observed physical characteristics of vegetation presence, pond depth, and hydrologic connectivity. To assess the importance of meteorological drivers on daily ebullitive flux (e.g. incoming solar radiation [SWR], air temperature [T_{air}], pond temperature [T_{pond}], and air pressure changes over a five-day moving window [ΔP_5]), non-parametric Kendall correlation tests were used. However only weak correlations were observed. This result indicated that meteorological parameters were less important at driving fluxes than apparent physical differences between ponds (types).

In addition to manual flux sampling, two UASs were used to collect high spatial-resolution imagery of seven small thaw ponds over five growing seasons (2014 – 2018). Over this period, 144 images were developed, and two polygons hand delineated for each pond; the first representing the extent of collapsed area (pond edge) and the second representing the extent of water within the pond. Non-parametric Kruskal-Wallis sums tests and Kendall Correlation tests were used to assess the variability in polygon area (both pond edge and water) seasonally and interannually over the study period and to investigate relationships between pond size and CH₄ ebullitive emission. Dunn's tests were used to determine significant pairwise comparisons between variables. Over several growing seasons, pond edge and water area varied significantly between ponds and pond types. Higher annual ebullitive emissions were seen among the smaller thaw

ponds in this study, however this can be attributed to cumulative differences in physical characteristics rather than simply differences in size.

Lastly, this work effectively used a hydroacoustic monitoring system to monitor ebullitive emissions from two thaw ponds during the 2018 growing season. Generalized Mixed Effects modeling (GLMM) was applied to investigate the influence of high temporal-resolution meteorological variables (e.g. T_{air} , SWR, WS; 2-hr averages) on bubble detections from the acoustic system. Results of the GLMM analysis showed that ebullition varied spatially and temporally across the study period within a single pond. Meteorological drivers (SWR, T_{air} and WS) explained little of the variability in acoustic detections across the study period however, sub-daily variability in average bubble emissions appearing to follow diel fluctuations in SWR, T_{air} and WS.

Through the use of multiple measurement techniques, at a variety of different spatial and temporal scales, I have concluded that (1) physical characteristics of ponds explain ebullitive flux variability between ponds, (2) higher ebullitive emissions are seen from smaller ponds, yet this is more related to physical differences between ponds rather than size supporting the first finding, and (3) ebullitive emissions on a sub-daily scale follow diel fluctuations in T_{air} , SWR and WS. These results support the need for monitoring of physical characteristics and areal extent of thaw ponds in tandem with high frequency (e.g. daily and sub-daily), measurements of CH_4 ebullition over multiple seasons due to the dynamic nature of these ecosystems. The effective combination of varying spatiotemporal sampling techniques (manual measurements, UAS imagery collection and acoustic monitoring) is also highlighted, as each technique provides new

ways to expand our understanding of subarctic thaw ponds. While monitoring pond size over time is an important component of modeling CH₄ emissions across the changing Arctic, this work suggests that monitoring other pond characteristics, like pond type, in conjunction with size are important in understanding CH₄ emissions, and how they might change in the future. With the inclusion of the thaw pond classification in Earth system models, in addition to measurements of size, modelers can better represent CH₄ emissions from thaw ponds in models of the changing Arctic.

CHAPTER 1: LONG TERM MEASUREMENTS OF METHANE EBULLITION FROM THAW PONDS¹

1.1 Abstract

Arctic regions are experiencing rapid warming, leading to permafrost thaw and formation of numerous water bodies. Although small ponds in particular are considered hotspots for methane (CH₄) release, long-term studies of CH₄ efflux from these surfaces are rare. We have collected an extensive dataset of CH₄ ebullition (bubbling) measurements from eight small thaw ponds (< 0.001 km²) with different physical and hydrological characteristics over four summer seasons; the longest set of observations from thaw ponds to date. The measured fluxes were highly variable with an average of 20.0 mg CH₄ m⁻² d⁻¹ (median: 4.1 mg CH₄ m⁻² d⁻¹, n = 2063) which is higher than that of most nearby lakes. The ponds were categorized into four types based on clear and significant differences in bubble flux. We found that the amount of methane released as bubbles from ponds was very weakly correlated with environmental variables, like air temperature and atmospheric pressure, and was potentially more related to differences in physical characteristics of the ponds. Using our measured average daily bubble flux plus the available literature, we estimate circumpolar thaw ponds < 0.001 km² in size to emit between 0.2 and 1.0 Tg of CH₄ through ebullition. Our findings exemplify the

¹ This chapter has been published and the full citation is as follows: Burke, S. A., Wik, M., Lang, A., Contosta, A. R., Palace, M., Crill, P. M., & Varner, R. K. (2019). Long-Term Measurements of Methane Ebullition from Thaw Ponds. *Journal of Geophysical Research: Biogeosciences*, 2018JG004786. <https://doi.org/10.1029/2018JG004786>

importance of high frequency measurements over long study periods in order to adequately capture the variability of these water bodies. Through the expansion of current spatial and temporal monitoring efforts, we can increase our ability to estimate CH₄ emissions from permafrost pond ecosystems now and in the future.

1.2 Plain Language Summary

Long term studies of methane emissions from thaw ponds are rare but essential for our understanding of how these ecosystems are responding to Arctic warming. Our study incorporates over 2000 measurements of methane gas, collected over four summer seasons from eight small ponds located within one single peatland in northern Sweden. These ponds formed when frozen soil thawed due to increasing air temperatures. Ponds like this are known to release methane, a strong greenhouse gas, through bubbling, diffusion along a concentration gradient, and transport through plant internal structure, though bubbling is the least understood. We also used photographs collected with a drone to estimate the area of each pond. We found the ponds to vary widely in methane emission over time as well as between ponds. We also found that meteorological variables like air temperature and atmospheric pressure explained little of the variability in bubble flux we measured. Our measurements represent the longest record of bubble measurements from climate sensitive ponds to date and help us to better understand the amount of methane released and what controls it. It is important to include these bodies of water in our understanding of how Arctic areas are changing with increasing air temperatures.

1.3 Introduction

It is essential to quantify sources of atmospheric methane (CH₄) because it is a radiatively important trace gas with thirty-two times the warming potential of carbon dioxide (CO₂) over a 100-year timescale (Holmes et al., 2013). Sources at high latitudes are significant contributors of CH₄ to the atmosphere (Kirschke et al., 2013; Saunio et al., 2016), although the effect of increased Arctic warming on CH₄ release is uncertain. For example, an increase in emissions could occur in conjunction with rising temperatures and permafrost thaw (Schuur et al., 2008), but extensive thaw could alternatively lead to large scale drainage of wetlands and an overall decrease in CH₄ emissions (Avis et al., 2011).

Permanently frozen peatlands in the northern hemisphere alone are estimated to contain between 436 -547 Pg of soil organic carbon (OC; Loisel et al., 2014; Yu et al., 2010). When such peatlands thaw, some of this sequestered OC may become available for anaerobic decomposition processes in which CH₄ is the final byproduct (IPCC, 2013; Laurion et al., 2010; O'Donnell et al., 2011). Once CH₄ is produced in anoxic environments there are three main transport modes to the atmosphere: ebullition (bubbling), hydrodynamic flux (previously called diffusive flux), and plant assisted transport. Ebullition is often dominant but still the least understood (Bastviken et al., 2011; Coulthard et al., 2009; Fechner-Levy & Hemond, 1996). The uncertainty in ebullition is due to highly episodic releases, triggered by environmental conditions such as changes in water level and atmospheric pressure (Goodrich et al., 2011; Weyhenmeyer, 1999), in combination with large spatial variations (Laurion et al., 2010;

Wik et al., 2013), as well as lack of measurements able to account for these heterogeneities (Wik, Thornton, et al., 2016).

Thawing of ice-rich permafrost and the ensuing collapse of peat surfaces can give rise to thermokarst, or subsidence of the land surface due to permafrost thaw (O'Donnell et al., 2011; Zimov et al., 2006), and the formation of water bodies of different sizes (Bouchard et al., 2014; Negandhi et al., 2013; O'Donnell et al., 2011). Very small ponds (defined in this study as those with a surface area $< 0.001 \text{ km}^2$) comprise less than 9% of the total area covered by lakes and ponds globally yet they are estimated to contribute 40% of the hydrodynamically driven diffusive CH_4 emissions from freshwater lakes and ponds worldwide (Holgerson & Raymond, 2016). A review of both ebullitive and hydrodynamic emissions from water bodies located north of 50°N found that small ponds are a significant source of CH_4 for the northern latitudes (Wik, Varner, et al., 2016). However, few of the available studies focus on ebullition and even fewer present multiple seasonal measurements (Wik, Varner, et al., 2016). Therefore, further study of bubble flux from small ponds is needed to provide a quantitative understanding of the emissions and potential feedbacks of the warming of these ecosystems.

Shifts in vegetation species composition and hydrologic change associated with pond formation have effects on OC cycling in permafrost ecosystems. For example, changes in vegetation composition can increase CH_4 emissions (Johansson et al., 2006; King et al., 1998; Kutzbach et al., 2004). When vascular plants colonize newly thawed, wet areas they can become conduits for CH_4 to bypass oxidation that can occur

in oxic zones near the air/water interface (Chanton, 2005; Noyce et al., 2014) as well as provide newly fixed OC as substrate for methanogenesis (Chanton et al., 2008; Malmer et al., 2005). Vascular plants can also transport oxygen to the submerged rooting zone, therefore allowing for oxidation to occur (Laanbroek, 2010; Whalen, 2005). Increased wetness due to permafrost thaw (O'Donnell et al., 2011) can provide new habitat for plants that have an affinity for wetter conditions such as sedge species, e.g. *Eriophorum angustifolium*, *Carex rostrata* (Malhotra & Roulet, 2015; Malmer et al., 2005) and different species of *Sphagnum*. *Sphagnum spp.* are considered a common initial colonizer of thawed, wetter areas due to their preference for lower pH and nutrient conditions in the absence of flowing water (van Breemen, 1995; Gignac et al., 1991; Glaser, Hansen, et al., 2004; Vitt & Slack, 1975). Continued thaw and consequent increase in wetness may not only increase anoxia, providing an ideal environment for methanogenesis (Segers, 1998), but may also lead to these areas becoming connected to already wet surrounding fens and thus introduce a flow component into these systems (Olefeldt & Roulet, 2012). Distinguishing sub-habitats from each other based on vegetation characteristics and hydrology was conducted previously in some subarctic peatlands (e.g. Johansson et al., 2006; Malhotra & Roulet, 2015; Malmer et al., 2005) though very few studies have applied classification schemes to thaw ponds (Kuhn et al., 2018). Changes in vegetation and hydrology can impact the production rates and emission of CH₄ and therefore should be accounted for when modeling these changing ecosystems.

The goal of this study is to improve our understanding of the magnitude and controls on the spatiotemporal variation in daily ebullitive CH₄ emissions from rapidly changing ponds in a highly dynamic permafrost ecosystem. Here we report measurements of ebullitive CH₄ flux, collected over four summer sampling seasons, from eight ponds located in northernmost Sweden.

1.4 Methods

1.4.1 Study Site

We studied eight ponds located within the Stordalen Mire, a sporadic permafrost peatland complex located 10 km east of Abisko in northernmost Sweden (68°21'N, 19°02'E, Figure 1.1). Since 2000, climate trends in northern Sweden have led annual mean temperatures to cross the 0°C threshold, thus destabilizing permafrost (Callaghan et al., 2010). Consequently, rapid permafrost thaw and changes in vegetation cover have been observed in the Stordalen area (Johansson et al., 2006; Malmer et al., 2005). The mire contains the following sub-habitats: palsa plateaus, semi-wet *Sphagnum spp.* dominated areas, wet *Eriophorum spp.* dominated areas, and collapse features due to thaw. Collapse features that accumulate water (Christensen et al., 2004) are classified as thaw ponds. Satellite imagery, focusing on the terrestrial area of Stordalen Mire, reveal the areal extent of hummocks (e.g. cold, dry, raised permafrost mounds) and tall shrubs has decreased by 10% between 1970 and 2000. These areas have been recolonized by more moisture-tolerant vegetation (i.e. graminoids) that consequently release more CH₄ to the atmosphere, resulting in a 48% increase in the

radiative forcing of this site from 1970 to 2000 (Johansson et al., 2006). Some thaw ponds in Stordalen Mire were also included in a recent study by Kuhn et al. (2018), that reported CO₂ and CH₄ emissions from floating chambers. However, the CH₄ measurements in this study were scarce, made on a biweekly schedule, which is far from ideal when investigating ebullition (Wik, Thornton, et al., 2016). Kuhn et al. (2018) distinguished ponds from each other based on vegetation dominance and hydrology but no difference in overall emissions was observed between pond types in this one-season investigation.

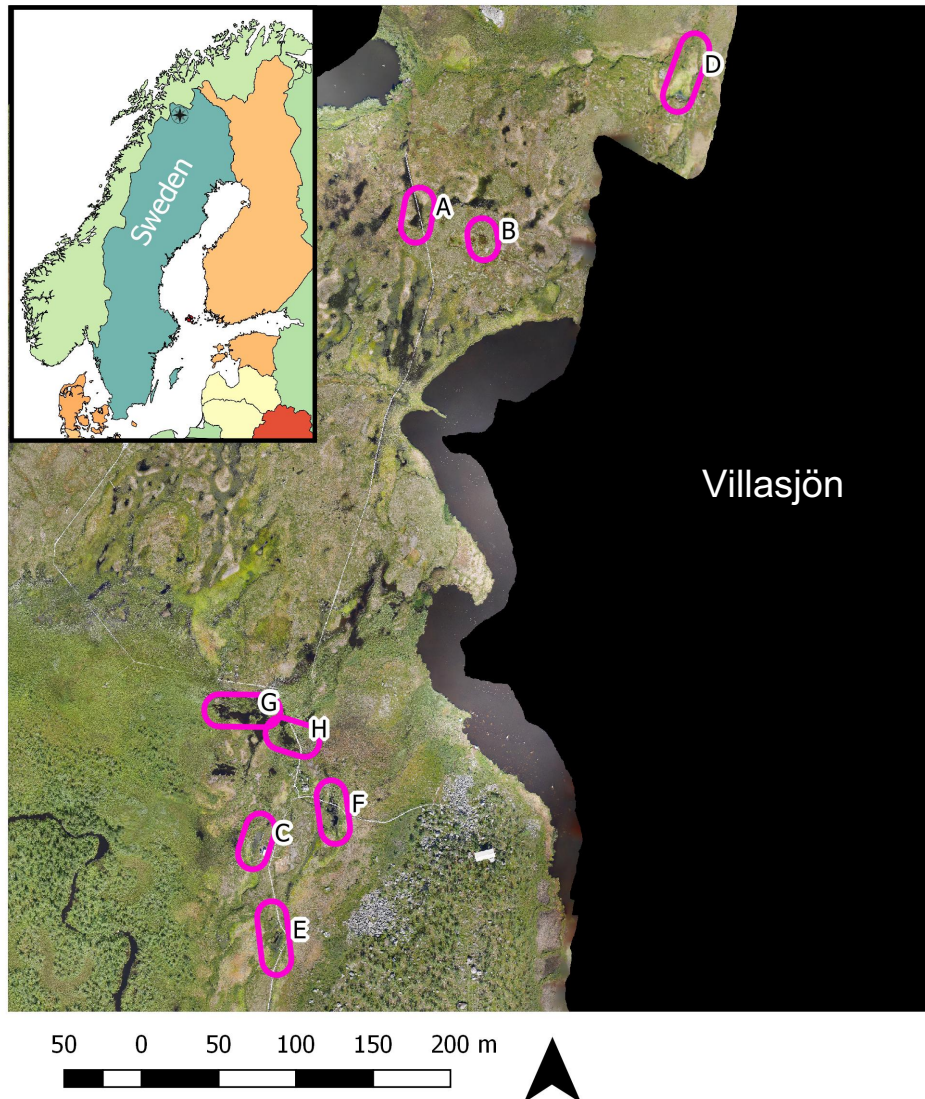


Figure 1.1. Adapted from Burke et al. (2019). Orthomosaic image of the Stordalen Mire in northernmost Sweden, (68°22' N, 19°03' E) taken 12 July 2016 from a collection of images acquired at an altitude of 70 m using an unmanned aerial system (UAS). Ponds measured in this study are labeled with their corresponding letter. Using Google Earth Engine, transect lines were drawn across the length of each pond and 10 m oval shaped buffers (here outlined in magenta) were drawn around each transect. These were used to calculate spatial extent of ponds based on the percent wet area within the buffer. Rough edges show the extent of the stitched images. The general location of lake Villasjön is represented by its label.

1.4.2 Pond Sites

Pond sampling sites were chosen based on their proximity to boardwalks and ease of access so as to minimize mire and sampling disturbance. The following descriptions of the ponds were generally identified during surveys conducted in 2013 and 2014 (see

below and Table 1.1). Such descriptions include water table depth (WTD), relative *Sphagnum spp.* and sedge (e.g. *Eriophorum spp.*, *Carex spp.*) vegetation presence and hydrologic regime. Measurements of WTD presented here are the averaged values of measurements collected over both 2013 and 2014 surveys (see Table A.1 for averaged WTD for 2013 and 2014 separately). At Stordalen Mire, the WTD in *Eriophorum* dominated sites varies much less than in *Sphagnum* dominated sites (Bäckstrand, 2010). We found a similar relationship in the ponds, with those that were shallow and isolated to be more vulnerable to dry-out than those that were connected to neighboring fens. Hydrologic connectivity was determined visually and is supported by flow paths developed previously for this site (see Olefeldt & Roulet, 2012). The abundance of *Sphagnum spp.* and sedge species (*Carex spp.* and *Eriophorum spp.*) were based on comparisons of the vegetation surrounding each pond relative to the other study ponds and was not expressly quantified.

Ponds *A* and *B* – the shallowest ponds in this study (22 cm and 18 cm respectively) and unlike the other ponds, are surrounded by few sedges and are located in the northeast of the mire, on a palsa plateau (Figure A.1).

Pond *C* – positioned with one edge along a collapsed palsa, is hydrologically isolated from neighboring fen areas and contains floating *Sphagnum spp.* It also has an increased presence of *Eriophorum spp.* relative to that of ponds *A* and *B* (Figure A.1).

Pond WTD = 35 cm.

Pond *D* – features collapsing palsa on one side, *Eriophorum spp.* and *Carex spp.* along the opposite and a clay-rich bottom. It is located in the top left corner of the site and abuts a fen area that has water flowing from east to west (Figure A.1). WTD = 41 cm.


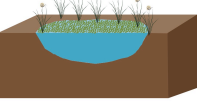
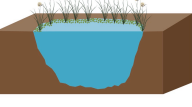
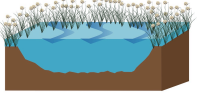
Pond *E* – positioned on a remnant palsa and is hydrologically isolated from the surrounding fen areas. This pond contains significant amounts of floating *Sphagnum spp.* and some *Eriophorum spp.* and *Carex spp.* along the edges (Table 1.1, Figure A.1.E). Observations made of the area since 2003 show that this particular pond began forming around 2007 (P. Crill, unpublished data). Pond *E* is the deepest in this study with a WTD of 85 cm (Table 1.1).

Pond *F* – is hydrologically isolated like pond *E* (Figure A.1.F). It is surrounded by collapsing palsa, with *Carex spp.* and *Eriophorum spp.* present along its edges. WTD = 43 cm.

Pond *G* – contains no *Sphagnum spp.* but is surrounded by sedge species and is connected to a fen that drains the neighboring Lake Villasjön (Figure A.1.G). The water flows west through the fen towards the catchment's main stream (Figure 1.1). WTD = 47 cm.

Pond *H* – positioned between pond *G* and the fen, containing similar vegetation to pond *G* (Figure A.1.H). WTD = 41 cm.

Table 1.1 Characteristics of ponds sampled at Stordalen mire, Abisko, Sweden between 2012-2015. Mean water temperature is the average water temperature measured between 1 June and 30 September between 2014 – 2015 field seasons. Median pH is presented here due to the minimal measurements collected in 2014. Vegetation presence is described as whether or not Sphagnum spp. is present (distinguished by a check mark or an X) and sedge presence (Eriophorum spp. and or Carex spp.) as low, medium or high presence in comparison to ponds A and B. A schematic showing the relative depth, vegetation, and hydrology is shown on the left side of the table. Based on similarities between their physical characteristics, the ponds can be grouped into four pond types: (1) shallow with low sedge presence, (2) intermediate depth and increased sedge presence, (3) deepest and sedge dominated, and (4) intermediate depth, open water and flow through present.

	Pond	n	Surface Area* (m ²)	Average WTD (cm)	Vegetation Present		Other notes	Hydrologic Status ♦	Mean Water Temperature (°C)	Median pH
					Sphagnum spp.	Sedges				
Type 1 	A	67	110	22	✓	<i>Eriophorum spp.</i>	Isolated	11.6	4.1	
	B	196	32	18				12.1	3.8	
Type 2 	C	311	24	35	✓	<i>Eriophorum spp.</i> (increased presence relative to ponds A and B)	collapsing palsa along one edge and a fen on the other Transitioning	10.2	4.3	
	D	289	13	41			Collapsing palsa on one edge, fen on the other, clay bottom	10.0	4.5	
Type 3 	E	289	83	85	✓	<i>Eriophorum spp.</i> and <i>Carex spp.</i> around edge (increased presence relative to ponds C and D)	collapsing palsa surrounding, fen area along one edge Isolated	5.8	3.8	
	F	529	135	43				8.0	4.3	
Type 4 	G	72	451	47	X	<i>Carex spp.</i> and <i>Eriophorum spp.</i> around the edge (increased presence relative to ponds C and D)	Open Water; Connected to adjacent Fen	11.6	NA	
	H	319	161	41				12.2	5.9	

* Image analysis of 2016 UAS image. ♦ Classification based on Olefeldt & Roulet (2012). A pond considered to be **isolated** is surrounded by intact peat and is not connected to any adjacent fen areas. A **transitioning** pond is one that is partly surrounded by intact peat but has the potential to be connected to adjacent fens that receive water from neighboring lakes (i.e. shallow waterlogged peats between the pond and surrounding fen areas). A pond that is considered to be **connected to adjacent fen** are ponds that intersect areas of known flow (Olefeldt and Roulet, 2012).

All eight ponds were sampled for at least two summer seasons during 2012-2015; ponds *C* and *H* were sampled for all four summer seasons, ponds *B*, *D*, *E*, *F* were sampled for three seasons, and ponds *A* and *G* were sampled for only two of the four summer sampling seasons. Pond *A* was subject to drying during the field season more than the other ponds, rendering it too shallow to deploy bubble traps (e.g. this pond was not sampled during the warm and dry summer of 2014) and Pond *G* became too difficult to sample without causing disturbance to the site after two sampling seasons.

Once during the 2013 sampling season, WTD, was manually measured at all our study ponds at a single time period (Table A.1). In 2014, WTD, and dissolved oxygen concentration (DO; mg L⁻¹; YSI Environmental Model 556) were measured weekly between June and September in the surface water of each pond (except for pond *G*, Table A.1). Measurements of active layer depth below each pond were attempted during 2013 and 2014 but the permafrost layer was consistently below the length of the measurement tool (100 cm), therefore those data are not presented here. Measurements of the surface pond water pH (Waterproof Double Junction pHTestr 30, Oakton Instruments) were collected three times during the 2014 sampling season (8 July, 23 July, and 24 August; median value presented in Table 1.1).

To determine the surface area of each of our study ponds (presented in Table 1.1), we used remotely sensed image data collected from an unmanned aerial system (UAS; Triton XL with a Goose autopilot from Robota; <http://www.robota.us/>). The imagery was collected on July 12, 2016 at 11:30 am local time. We flew during this time because vegetation could be easily distinguished, and it overlapped with a period of another

study. More than 700 images were collected over a 26-minute time period using a commercial, handheld RGB camera (Lumix GM-1). The UAS was flown at an altitude of 70 m. Imagery was stitched together using Photoscan Pro 1.2 by AgiSoft (<http://www.agisoft.com/>). We used existing georeferenced UAS imagery data from 2014 (Palace et al., 2018) to georeference the 2016 image (QGIS 2.14 Essen was used for georeferencing). The result was an image with 3 cm resolution and an estimated spatial error of 5 cm (Figure 1.1).

We then used Google Earth Engine to manually delineate transects across each of the eight ponds with each transect featuring a 10-m buffer. Due to the oblong shape of many of the ponds, a 10-m buffer around a delineated center line was used in order to enclose the pond while limiting the inclusion of neighboring ponds. We developed additional bands for pond surface area analysis using texture algorithms in Google Earth Engine (entropy and gray-level co-occurrence matrix, GLCM) on red, green, and blue bands. A kernel of 5 by 5 pixels was used for all texture analysis (Palace et al., 2018). We ran an unsupervised classification using a k-means algorithm on the entire image (Arthur & Vassilvitskii, 2007). We used 15,000 samples randomly selected across the mire with eight classes for the cluster analysis. A cluster was considered a set of connected pixels with a maximum size of 256 pixels and the connection of these pixels with four connected neighbors. Each cluster was then given a class value. From the classified image, we determined that one of the specific classes represented open water (containing no submerged vegetation) based on visual inspection of the original UAS

collected image. Tallies of pixels for each class were extracted for each pond transect, and total surface area of open water was determined for each polygon.

1.4.3 Ebullition sampling

Ebullition of CH₄ from the ponds was measured using bubble traps that were similar in design to those used by Wik et al. (2013). Since we were focused on understanding the drivers of bubble flux through long term monitoring, we did not quantify diffusive or plant mediated flux. They consisted of inverted plastic funnels (30.5 cm diameter) affixed with tubing (10 cm × 1 cm inner diameter) capped with a 60-mL syringe, a three-way stopcock, and sealed with 3M Marine Adhesive Sealant (Fast Cure 5200). The bubble traps were 45 cm tall, from the bottom of the funnel to the top of the stopcock. Two bubble traps were deployed in each pond, with the exception of pond *F* which had four traps due to its oblong shape, for the duration of the field season (June through September). The traps were deployed adjacent to each other and kept afloat using Styrofoam blocks so that the traps would not disturb the bottom of the ponds. Accumulated gas was collected manually from the traps using 10 mL polypropylene syringes. Gas samples collected from the traps were returned to the laboratory at the Abisko Scientific Research Station (ANS) and analyzed for CH₄ mixing ratios within 24 hours of sampling according to the procedure described in Wik et al. (2013), using a gas chromatograph equipped with a flame ionization detector (GC-FID, Shimadzu 2014). Samples were collected from the traps on daily to weekly timescales over four summer sampling seasons; 86.5% of the measurements were made between one and three days apart. A small percentage (11%) of the measurements had a sample period

greater than 3 days ($n = 227$); 91 of these samples (collected mostly in 2014 and 2015) were run on the GC for CH_4 concentrations, likely providing an underestimated mixing ratio for flux calculation. The remaining measurements ($n = 136$, collected in 2012 and 2013) used the volume of gas accumulated multiplied by a moving seasonal average CH_4 concentration to calculate emissions. Wik et al. (2013) found CH_4 dissolution back into the water column in their floating funnels to be minimal if samples were collected within 3 days. The small percentage of our measurements that fall out of this 3-day criteria introduce a minimal source of error into our calculations and likely underestimate therefore providing a conservative estimate of ebullitive emissions for those time periods.

1.4.4 Pond water temperature and meteorological variable collection

Pond water temperature was measured continuously from July 2013 onward using temperature data loggers (HOBO Water Temp Pro v2, model U22-001) that were set to record every five minutes between June and September. In the ponds deeper than 30 cm, we measured temperatures at ~ 10 cm below the water surface and at ~ 5 cm above the bottom of the pond. In ponds that were shallower than 30 cm, only one logger was deployed to measure surface water temperature. Though not the focus of this study, all ponds froze completely during the winter. Meteorological parameters of interest such as air temperature (T_{air}), air pressure (atmp), and incoming shortwave radiation (SWR) were obtained from the ANS weather station (ANS, 2017).

1.4.5 Data processing and analysis

Daily CH₄ bubble flux from each pond was calculated, using code developed in R version 3.3.3 (R Core Team, 2017), following the protocol described in Wik et al. (2013). In our study, however, we used a smaller funnel cross-section area (0.05 m²) when calculating the fluxes. Since samples were not collected every single day throughout the study period, daily flux calculations assume a steady release of gas between the time sampled and previous sampling time. Pond temperature data collected from the HOBO loggers as well as meteorological data of interest were also processed in R to calculate daily averages between 1 June and 30 September of each year in the study (T_{pond} , T_{air} , SWR respectively). In order to explore how large drops in atmospheric pressure may elicit ebullitive events, as shown previously by e.g. Tokida et al. (2007), we calculated the difference between current day atmospheric pressure and the average over the previous five days (i.e., ΔP_5) and used this value in the analyses.

Statistical analysis of daily CH₄ flux measurements was also performed using R. Several steps of data exploration, described by Zuur et al. (2010), were performed to assess both the presence of outliers as well as potential violations of key assumptions in parametric statistical analysis, such as normality, collinearity, equal variance, and autocorrelation. Due to violations of these key assumptions in our data, we chose to analyze our data using non-parametric tests. We performed Kruskal-Wallis sum tests to examine variation in bubble flux as a function of pond, month, sampling season and on the combination of month and sampling season with pond. A post-hoc Dunn's Test of multiple comparisons using the Bonferroni method ($\alpha = 0.05$) was performed to determine pairwise comparisons (dunn.test package; Dinno, 2017). Lastly, we used the

non-parametric Kendall correlation test to investigate the influence of meteorological variables (SWR, T_{air} , T_{pond} , ΔP_5) on bubble flux. Based on the criteria developed by Cohen (1988), we classified correlations as strong, moderate, or weak depending on the value of the Kendall's tau (τ) statistic. According to these criteria, the absolute value of τ , which ranges between -1 and 1, was greater than or equal to 0.5 for strong correlations, between 0.3 and 0.5 for moderate correlations, and between 0.1 and 0.3 for weak correlations (Cohen, 1988). If the absolute value of τ was less than 0.1, we considered the strength of the correlation to be very weak, even if the p -value was statistically significant.

1.5 Results

1.5.1 Variation in daily bubble flux among ponds

Daily bubble flux varied across the sampling seasons in all ponds, with episodic events of high CH_4 flux observed periodically (characterized by short term peaks in flux; Figure 1.2). Some of these episodic events appear to correspond to drops in atmospheric pressure (Figure A.3 & Figure A.4). For some ponds, peaks in bubble flux during the sampling season also appear to follow increases in pond temperature however this was not observed in all ponds (Figure 1.2). Across the entire data set, daily average meteorological parameters (SWR, T_{air} , T_{pond} , ΔP_5) were found to correlate with daily bubble flux ($p < 0.05$, Table A.2). Although these correlations were statistically significant, Kendall's τ values indicated that these correlations were very weak ($-0.13 < \tau < 0.09$, Table A.2). For example, we observed a significant, positive correlation between

SWR and daily bubble flux ($p = 0.001$, Table A.2). We interpreted this correlation as very weak despite its statistically significant p -value because the corresponding τ was -0.05 (Table A.2).

Our eight ponds measured over four sampling seasons had an overall average daily bubble flux of $20.0 \text{ mg m}^{-2} \text{ d}^{-1}$ (Median: $4.1 \text{ mg CH}_4 \text{ m}^{-2} \text{ d}^{-1}$, $n = 2063$). The shallowest ponds in this study (*A* and *B*), were the lowest emitting, with near zero fluxes (*A* & *B* median: $0.0 \text{ mg CH}_4 \text{ m}^{-2} \text{ d}^{-1}$, Table 1.2). Ponds *C* and *D*, both deeper than ponds *A* and *B*, emitted on average 4.5 and $3.6 \text{ mg CH}_4 \text{ m}^{-2} \text{ d}^{-1}$ respectively (*C* median: $0.5 \text{ mg CH}_4 \text{ m}^{-2} \text{ d}^{-1}$, *D* median: $0.1 \text{ mg CH}_4 \text{ m}^{-2} \text{ d}^{-1}$, Table 1.2). The most frequent ebullition came from the deepest isolated ponds (ponds *E* and *F*: daily average of 53.4 and $40.9 \text{ mg CH}_4 \text{ m}^{-2} \text{ d}^{-1}$ respectively, *E* median: $22.5 \text{ mg CH}_4 \text{ m}^{-2} \text{ d}^{-1}$, *F* median: $21.6 \text{ mg CH}_4 \text{ m}^{-2} \text{ d}^{-1}$, Table 1.2). The hydrologically connected ponds (*G* and *H*) emitted on average less than half the amount (*G* median: $6.4 \text{ mg CH}_4 \text{ m}^{-2} \text{ d}^{-1}$, *H* median: $11.7 \text{ mg CH}_4 \text{ m}^{-2} \text{ d}^{-1}$, Table 1.2) emitted by *E* and *F* (11.6 and $26.5 \text{ mg CH}_4 \text{ m}^{-2} \text{ d}^{-1}$ respectively), the deep, isolated ponds. There was no consistent pattern between surface area of ponds and bubble flux in any sampling season (Table 1.1).

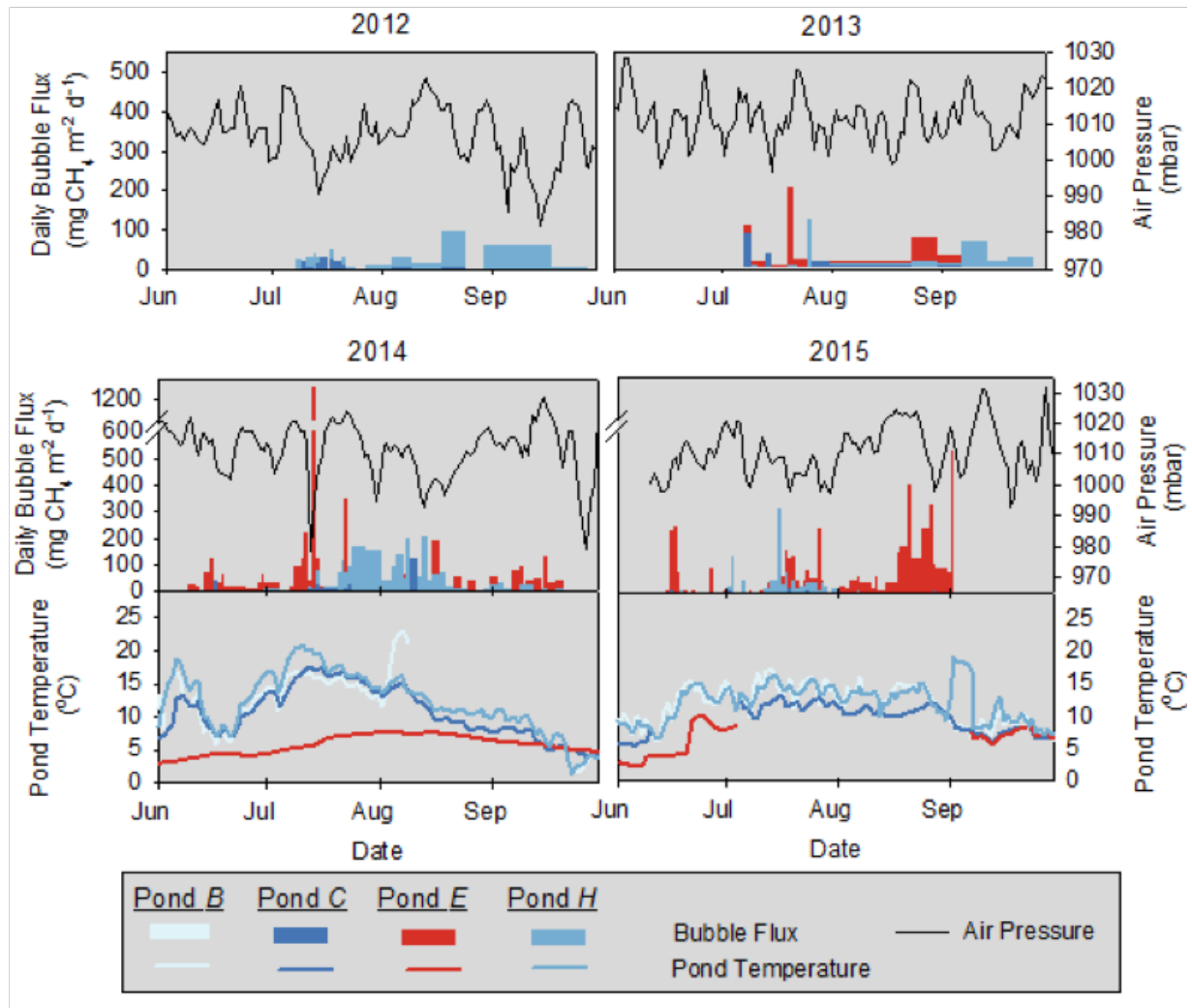


Figure 1.2 Daily bubble flux ($\text{mg CH}_4 \text{ m}^{-2} \text{ d}^{-1}$) and pond temperature ($^{\circ}\text{C}$) from selected ponds due to their statistically significant bubble flux (distinguished by different colored bars and lines respectively) located in the Stordalen Mire, Abisko Sweden. Daily average atmospheric pressure (mbar) for each sampling season is displayed as a black line (ANS, 2017).

During the study period, daily bubble fluxes varied significantly between ponds across the peatland ($\chi^2 = 841.55, p < 0.0001$, Figure 1.3). We classified the ponds into four types, based on the pairing of ponds due to statistical similarity, and found that these four types coincided with apparent differences in physical characteristics between ponds as described above (see Section 1.4.2; Table 1.1).

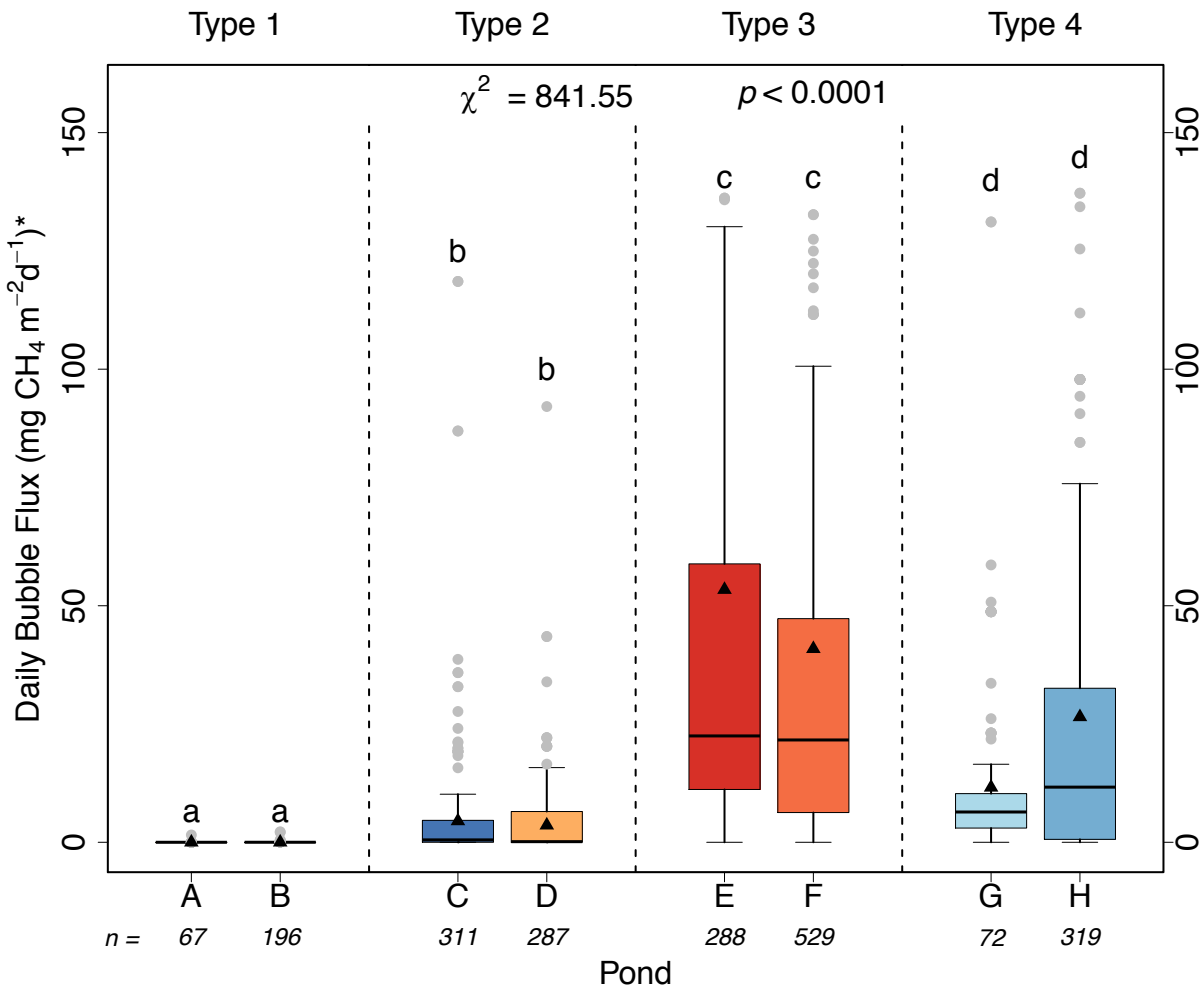


Figure 1.3 Boxplots of all measurements collected over four sampling seasons represented as daily bubble flux ($\text{mg CH}_4 \text{ m}^{-2} \text{ d}^{-1}$). The different colors are used to distinguish ponds from each other. To show the real distribution of the data, the y axis was plotted between 0 and 150 $\text{mg CH}_4 \text{ m}^{-2} \text{ d}^{-1}$, with outliers greater than 140 $\text{mg CH}_4 \text{ m}^{-2} \text{ d}^{-1}$ omitted from this figure. The number of measurements collected at each pond over the study period are in italics below each pond label. Solid triangles represent the mean daily bubble flux of each pond across the study period. Dark lines across each box represent median values and small grey circles represent outliers. Lowercase letters represent significant differences between ponds. Results of the Kruskal-Wallis rank sum test noted as χ^2 and p . Ponds are divided up into types 1 through 4 based on their statistically different fluxes and these types appear to correspond to physical differences (depth, vegetation presence, hydrology; see Table 1.1).

1.5.2 Monthly and seasonal variation in daily bubble flux

When combining all pond emissions over the study period, the highest monthly average of bubble flux across all sampling seasons occurred in July (24.5 $\text{mg CH}_4 \text{ m}^{-2} \text{ d}^{-1}$, Table 1.2) followed closely by August (20.8 $\text{mg CH}_4 \text{ m}^{-2} \text{ d}^{-1}$, Table 1.2). The lowest mean daily bubble flux occurred in September (14.2 $\text{mg CH}_4 \text{ m}^{-2} \text{ d}^{-1}$, Table 1.2). Looking

across sampling seasons, the lowest average daily bubble flux occurred during the 2013 sampling season ($10.7 \text{ mg CH}_4 \text{ m}^{-2} \text{ d}^{-1}$, $n = 314$, Table 1.2) coinciding with one of the warmest and rainiest and therefore cloudiest field seasons of the study (Table 1.3). We saw the highest average daily bubble flux during the 2015 sampling season ($28.5 \text{ mg CH}_4 \text{ m}^{-2} \text{ d}^{-1}$; Table 1.2) and conditions were cooler, less rainy, and clearer (Table 1.3).

We examined the monthly and full sampling season variability in the median bubble flux (see median values in Table 1.2), modeling each alone and in combination with each pond. As single factors, both month and sampling season were significant predictors of flux (month: $p < 0.0001$, Figure A.5, sampling season: $p < 0.0001$, Figure A.6). Pairwise comparisons of monthly medians showed that bubble flux in June was significantly different to that of July, August, and September (Figure A.5). This indicates that while the average daily bubble flux was highest in July, there appeared to be more days where bubble flux was zero in July, August and September, than in June. We also found that bubble flux varied significantly among most sampling seasons, except between 2013 and 2014 (Figure A.6).

Table 1.2 Temporal and spatial variability in CH₄ bubble flux across ponds, months and sampling season shown using arithmetic mean, range, median and 10th to 90th percentile. Ponds are listed in order by Type (1-4). Total numbers refer to the mean bubble flux across the four sampling season study period. Average daily CH₄ flux from each pond was calculated by averaging the daily flux from individual bubble traps in each pond to generate one daily flux per pond from each summer sampling season. N represents the number of samples collected.

	n	Daily Bubble Flux (mg CH ₄ m ⁻² d ⁻¹)			
		Mean	10th to 90th Percentile	Range	Median
Pond					
A	66	0.0	0 to 0	0.0 to 1.5	0.0
B	196	0.0	0 to 0.1	0.0 to 2.2	0.0
C	311	4.5	0 to 8.6	0.0 to 118.5	0.5
D	287	3.6	0 to 7.6	0.0 to 92.1	0.1
E	288	53.4	3.3 to 131.3	0.0 to 1257.1	22.5
F	524	40.9	1.8 to 93.4	0.0 to 1132.5	21.6
G	72	11.6	1 to 24.6	0.0 to 131.1	6.4
H	319	26.5	0 to 68	0.0 to 308.6	11.7
Month					
June	462	15.2	0 to 24.4	0 to 1132.5	0.0
July	874	24.5	0 to 67.6	0 to 1257.1	3.7
August	517	20.8	0 to 62.1	0 to 400.0	6.5
September	210	14.2	0 to 48.7	0 to 524.8	4.4
Sampling Season					
2012	117	17.3	0.6 to 62.1	0.0 to 131.1	5.0
2013	314	10.7	0 to 24.7	0.0 to 206.1	6.4
2014	689	24.9	0 to 68.5	0.0 to 1257.1	4.4
2015	943	28.5	0 to 87.2	0.0 to 1132.5	0.0
Overall					
Total	2063	20.0	0 to 58.8	0.0 to 1257.1	4.1

We also examined whether individual ponds behaved differently on a monthly and seasonal sampling season basis and found both of these interactions to be significant (month \times pond: $p < 0.0001$, Figure A.7, sampling season \times pond: $p < 0.0001$, Figure A.8). Though there were a few exceptions, daily bubble flux in ponds found not significantly different from each other across the whole study period (Figure 1.3) also did not significantly differ from one another within months or sampling seasons (see Table A.3 through Table A.6 for p values).

Table 1.3 Summary of meteorological data across the study period. Average incoming shortwave radiation (SWR, $W m^{-2}$), average air temperature (T_{air} , $^{\circ}C$) and total precipitation (P, mm) were calculated from data collected at the Abisko Weather Station (ANS, 2017). Average values were calculated across data spanning 1 June to 30 September of every summer sampling season.

	2012	2013	2014	2015
SWR ($W m^{-2}$)	142.9	145.8	176.3	162.54
T_{air} ($^{\circ}C$)	8.3	10.6	10.7	9.4
P (mm)	153.9	197.9	160.9	171.3

1.6 Discussion

1.6.1 Spatiotemporal variability in ebullitive emission across ponds

Our dataset is the longest record (four-sampling seasons) of high frequency measurement of CH_4 ebullition from thaw ponds. These data allow us to identify drivers of the spatial and temporal variability in bubble flux in very small, high latitude water bodies. Such analyses have not been possible since previous studies relied on few measurements over a short study period (Hamilton et al., 1994; Negandhi et al., 2013) or derive bubble flux indirectly from floating chambers (Kuhn et al., 2018; Laurion et al., 2010).

Wik et al. (2014) determined sediment temperature and incoming solar energy to be significant drivers of ebullitive CH₄ flux from lakes. These drivers are partly explained by the observed variability of emission with lake depth (Varadharajan & Hemond, 2012). In our case, SWR and T_{pond} were found to correlate with daily bubble flux. Because τ values varied between -0.13 and 0.09 (Table A.2), we interpret these correlations to be very weak (Cohen, 1988). This is unexpected since all of the ponds measured in our study are shallower than the shallow zones of the neighboring lakes (85 cm vs. 1.3 m; Wik et al. 2014). Although the ponds heat more rapidly, they also cool off faster due to a lower heat capacity. Hence, their water temperature is more variable on a daily basis (Figure 1.2) than those measured in the lakes (Wik et al. 2013). The apparent higher temperature sensitivity of the ponds could be due to their very shallow nature and less dense sediment (Wik et al., 2018), which could limit rapid gas pocket formation and thus promote a more erratic ebullition versus temperature pattern.

In peatland ecosystems where ebullitive events have been observed with high frequency measurements, water table and atmospheric pressure changes often seem to trigger the release of CH₄ bubbles (Glaser, Chanton, et al., 2004; Goodrich et al., 2011; Tokida et al., 2007). In lakes adjacent to our study ponds, long-term seasonal observations showed a doubling of bubble flux during periods of dropping atmospheric pressure over periods of increasing atmospheric pressure (Wik et al., 2013). Through the visual inspection of daily average bubble flux and atmospheric pressure, we found that large episodic bubbling events occurred in our ponds but were not always associated with changes in atmospheric pressure (Figure A.3-Figure A.4). Large

episodic events were not observed in all ponds at the same time, though events seen in higher emitting ponds (i.e. pond *E*, Figure A.3 and Figure A.4) appeared to be more associated with atmospheric pressure events than the lower emitting ponds (i.e. pond *B*, Figure A.3 and Figure A.4). These findings suggest that the CH₄ production rates below ground are higher and more important at these sites to fully saturate pore waters and recharge the pond sediments with bubbles in between episodic events (Weyhenmeyer, 1999; Wik et al., 2014). For this study, we did not collect high frequency WTD (though such measurements have been collected at this site; Persson et al., 2012). We believe the influence of fluctuating WTD on bubble flux is an area that should be explored further. Previous research at this site by Bäckstrand et al. (2010) showed that through manual measurements collected across the growing season that, WTD varied much more in sites dominated by *Sphagnum spp.* than by *Eriophorum spp.* dominated sites. We saw a similar relationship in the ponds with two isolated *Sphagnum* dominated ponds (*A* and *B*) drying out mid-sample season to the point where we could no longer sample. The variable WTD at these two ponds could partly explain why they had the lowest daily bubbly flux of all the ponds in this study.

Kuhn et al. (2018) recently classified 52 ponds in the Stordalen Mire and in nearby Storflaket bog into four types, based on dominant vegetation and hydrologic status, and determined there was no significant difference in bubble flux between pond types. In our study, we instead grouped the ponds into four types based on the statistical differences in daily bubble flux and found these statistical differences appeared to coincide with the ponds' apparent physical differences (Table 1.1, Figure 1.3). While we did not

quantitatively measure vegetation species composition, we did observe differences in vegetation between ponds (Table 1.1). Type 1 ponds likely exhibited the lowest CH₄ flux observed since they were underlain by permafrost and potentially had drier conditions exhibited by their low incidence of sedges compared to *Sphagnum* (Malhotra & Roulet, 2015; Malmer et al., 2005). Type 2 ponds were located on collapsing palsa margins in close proximity to flow through fens. The proximity to a collapsed palsa of this pond type indicates a potential increase in the decomposition rate of the thawed OC and increased OC lability, which is known to lead to increased CH₄ emissions (Chanton et al., 2008; Hodgkins et al., 2014). The pond type with higher bubble flux could have been influenced by the presence of sedges (types 2 and 3, Table 1.1) which may have increased available substrate for decomposition (Johansson et al., 2006; Kutzbach et al., 2004; Malmer et al., 2005). Alternatively, they may have also reduced bubble flux due to sedge roots transporting CH₄ to the atmosphere through their aerenchymous tissue (Noyce et al., 2014). We saw lower median bubble flux in June compared to July, August and September (Figure A.5), similar to what was seen in nearby lakes (Wik et al., 2013). This likely is indicative of the lower early season CH₄ production rates due to lower temperatures and the time-lag required to build up enough below ground CH₄ to form bubbles (Zeikus & Winfrey, 1976). Type 4 ponds had lower fluxes than type 3 but were within the same depth range. However, they had no *Sphagnum spp.* present and were connected to an adjacent fen allowing water to flow through them (i.e. pH of pond $H = 5.9$; Table 1.1) indicative of a flow-through fen (Chasar et al., 2000). The presence of flow through these water bodies could potentially affect the residence time of OC

within the system (Olefeldt & Roulet, 2012; Striegl & Michmerhuizen, 1998), increasing the chance of the water column remaining oxic (the average DO of pond *H* measure in 2014 was one of the highest we measured in this study, Table A.1). Oxygenation of the water column could also reduce the rate of deposition and burial of OC compared to other more isolated ponds in the study (Lundin et al., 2016; Olefeldt et al., 2013), which could further explain the lower fluxes measured at type 4 compared to type 3 ponds.

With significant changes in vegetation cover observed at Stordalen mire (Malmer et al. 2005) and the effect these changes have had on C emissions locally (Johansson et al., 2006), we can expect increased fluxes of CH₄ from these sites with further thawing of permafrost and the creation of larger and more numerous thermokarst ponds. The spatial variability in ebullition we observed appears to relate to the variety of physical characteristics among the ponds (dominant vegetation, depth, hydrologic connectivity) therefore suggesting that these characteristics are important to measure to increase our understanding of bubble flux from thaw ponds (Holgerson & Raymond, 2016; Kuhn et al., 2018; Wik, Varner, et al., 2016).

1.6.2 Pond emissions compared to other sub-habitats

The average daily bubble flux of 20.0 mg CH₄ m⁻² d⁻¹ from our measured ponds is more than 3 times that reported for open water at the Stordalen Mire (5.3 mg CH₄ m⁻² d⁻¹, Johansson et al., 2006 and the references therein). It is important to note that CH₄ flux reported in Johansson et al. (2006) for open water is an average of literature values for lakes in Wisconsin USA, northern Finland, and the Arctic, representing different

ecosystems and methodologies. In comparison to other mire ecosystems sub-habitats, our ponds emit up to 30 times less (53, 120, 293 mg CH₄ m⁻² d⁻¹ for semi-wet, wet, and tall graminoids, respectively; Christensen et al., 2004). The bubble fluxes from our ponds are 1.5 and six-fold lower rates than those of total hydrocarbon (THC) emissions from the nearby *Sphagnum spp.* and *Eriophorum spp.* dominated sites (30 and 127 mg CH₄ m⁻² d⁻¹, respectively; measured using autochambers and calculated as 80% of THC emissions reported in Bäckstrand et al., 2010). It is important to note however, that we present bubble flux while Bäckstrand et al., (2010) and Christensen et al. (2004) report CH₄ emissions from chamber measurements which include all transport pathways. In comparison to larger open water areas adjacent to the ponds, the average bubble flux measured at the nearby Villasjön lake is more than twice that was measured from thaw ponds in this study (45.4 mg CH₄ m⁻² d⁻¹; Wik et al., 2013). A comparison between the mean and 10th and 90th percentile from this study to that of Wik et al. (2013) shows that the data are somewhat overlapping, suggesting that ebullition is as highly variable in both the ponds as in the lakes.

In comparison to ebullition rates reported in the literature for some of these and other ponds in the Stordalen Mire area, our daily average bubble flux measures 20 mg m⁻² d⁻¹ (measured using frequent, often daily sampling over four sampling seasons [see Methods]) are an order of magnitude smaller than their than those of 272 mg CH₄ m⁻² d⁻¹, reported by Kuhn et al. (2018). Kuhn et al. (2018) sampled their chambers twice per week between June and October in 2015. Again, 39 days of direct ebullitive measurements, not estimated from chambers, are considered necessary to accurately

estimate local ebullitive emissions from lakes (Wik, Thornton, et al., 2016). Because more than 85% of our ebullitive measurements were made within one to three days (169 sampling days in total), we are confident that our numbers are representative for the Stordalen ponds. It is likely that the bubble flux estimate made by Kuhn et al. (2018) is an overestimation, due to their lack of direct measurements using bubble traps.

Our four seasons of high frequency bubble measurements from thaw ponds in a subarctic region show that these small and shallow surface waters are significant emitters of CH₄. The ebullition component of emissions from northern water bodies < 0.001 km² have been left out of recent syntheses (Holgerson & Raymond, 2016; Wik, Varner, et al., 2016) leaving a substantial part of the annual emission excluded from the CH₄ budget. Considering a bubble flux of 20 mg CH₄ m⁻² d⁻¹ as representative of small ponds, we calculated regional emissions using a total area of 59,105 to 344,361 km² across permafrost regions north of 50°N. These numbers are 40% of the global area range of < 0.001 km² ponds, reported in Holgerson et al. (2016), based on the general distribution of water bodies worldwide (Verpoorter et al., 2014). Including the estimated average of 149 ice-free days (Wik et al., 2016), we determined that between 0.2 and 1.0 Tg CH₄ is emitted via ebullition from thaw ponds <0.001 km² in size. We recognize that this estimate is conservative as recent attention has been paid to non-growing season fluxes from lake ecosystems, which includes ice-break up, spring thaw, and bubbles trapped in ice (Jammet et al., 2015, 2017; Wik et al., 2011). While we did not measure these fluxes, we expect that since these ponds freeze completely during the winter, they likely do not emit CH₄ during winter and have a low potential emission during ice-out.

We also did not measure diffusive flux or plant-mediated flux in this study, so this estimate does not represent total CH₄ from these ponds. At a regional scale, our estimate is almost one-fourth of that of Walter et al. (2006), which conservatively estimated the areal coverage of thermokarst lakes in the yedoma region of Northern Siberia to be 11% (3.8 Tg CH₄). On a global scale, our estimate is one-third of the estimated emission from thermokarst water bodies worldwide (3.3 ± 1.7 Tg CH₄) of which 2.6 Tg CH₄ (79%) is from ebullition (and includes the data in Walter et al., 2006; Wik, Varner, et al., 2016).

1.7 Conclusions

We collected over 2000 measurements, over four sampling seasons, of ebullitive emission from eight thaw ponds, making this dataset the largest of its kind. We investigated the drivers of significant spatial and temporal variability seen among the study ponds. Contrary to other studies, meteorological variables such as SWR, atmospheric pressure, and temperature showed very weak correlations with bubble flux. This result highlights the need for high frequency (e.g. sub-daily), long term measurements. Many of the studies available on this topic reference only portions of the sampling season, with some studies collecting samples for a month or less. Pond physical characteristics, such as water depth, vegetation presence and hydrology may be the primary control on a pond's ability to process OC and are critical observations for determining CH₄ emission potential from these systems. Since permafrost ecosystems are vulnerable to thaw due to climate change, it is likely that such characteristics as these could change rapidly over a pond's life time. Our findings agree with previously

published work that suggest thaw ponds are important emitters of CH₄ on regional scales. We suggest that the classification of type for small thaw ponds, through a combination of ground-based measurements, remote sensing and modeling, across all permafrost ecosystems is essential for modeling and scaling future emissions.

1.8 Acknowledgments, Samples, and Data

The co-authors would like to acknowledge the following funding in support of this project: the Northern Ecosystems Research for Undergraduates program (NSF REU site EAR#1063037, PI Varner), an NSF MacroSystems Biology grant (EF #1241037, PI Varner), UNH's Hamel Center for Undergraduate Research SURF Abroad grant, and by the Malmberg Scholarship Program of the American Swedish Institute, which is supported by the endowment established by Cornelia Malmberg through a generous bequest from her estate. A portion of this work was supported through the New Hampshire Space Grant Consortium, under NASA grant NNX15AH79H. This study was in part funded by the Genomic Science Program of the United States Department of Energy Office of Biological and Environmental Research, grants DE-SC0010580, DE-SC0016440. This study has been made possible by the Swedish Infrastructure for Ecosystem Science (SITES), in this case at the Abisko Scientific Research Station (ANS). Meteorological data were provided by Swedish Polar Research Secretariat, ANS, Abisko, Sweden. Thanks to staff at ANS for providing housing, equipment and laboratory space. Thanks to Niklas Rakos, Chris Hemmingsson, Matthew Osman, Justine Ramage, Mathilda Nyzell, Nathan Tomczyk, Eric Heim, Katharine Rocci, Kiley Remiszewski, Carmody McCalley, James Lazarcik for assistance in sample collection

and analysis. The figures in this paper are color-blind friendly using colors from www.ColorBrewer.org by Cynthia A. Brewer, Geography, Pennsylvania State University. Thanks to our reviewers for their diligent comments. The data associated with this work is stored on the data repository site of the ISOGENIE project and can be found at <https://isogenie-db.asc.ohio-state.edu/datasources#fluxes>.

CHAPTER 2: USING UNMANNED AERIAL SYSTEMS TO MONITOR THE CHANGE IN THAW POND SIZE OVER FIVE GROWING SEASONS: IMPLICATIONS FOR CH₄ EBULLITIVE FLUX²

2.1 Introduction

Freshwater aquatic ecosystems, including lakes and rivers, are a large source of atmospheric methane (CH₄; Bastviken et al. 2011; Ciais et al. 2013; Downing, 2010; Kirschke et al. 2013). Globally, small water bodies in particular have higher CH₄ concentrations and therefore emissions, than their larger counterparts (Bastviken et al., 2004; Downing, 2010). Recent work by Holgerson and Raymond (2016) have estimated that very small ponds (< 0.001 km²) comprise less than 9% of the area covered by lakes and ponds globally, yet they account for over 40% of the hydrodynamically driven diffusive CH₄ emissions from these water bodies. Additionally, inclusion of CH₄ emissions from ebullition, or bubbling, would make contributions from small ponds to the global CH₄ budget even more significant (Bastviken et al. 2011; Downing, 2010; Holgerson & Raymond, 2016; Wik, Varner, et al. 2016). A review of both ebullitive and diffusive emissions from lakes and ponds located above 50°N found that small ponds are a significant source of CH₄ for the northern latitudes (Wik, Varner et al., 2016). Yet a

² The work in this chapter is currently in prep for submission to a peer-reviewed journal: Burke, S. A., Palace, M., Contosta, A. R., Perryman, C., Bennett, K., Rocci, K., Herrick, C., Crill, P. M., & Varner, R. K. In prep. Using unmanned aerial systems to monitor the change in thaw pond size over five growing seasons: Implications for CH₄ ebullitive flux. *Remote Sensing of the Environment*.

full understanding of the size of these waterbodies, the relationship between their size and the amount of CH₄ they emit, and how these change over time remains unknown.

Small ponds, in particular thaw ponds, which develop due to the thawing and slumping of ice-rich permafrost peat (Bouchard et al., 2014; Negandhi et al., 2013; O'Donnell et al., 2011), represent an ecosystem type that has the potential to become more dominant as the Arctic continues to change in response to increasing global atmospheric temperatures (Shirokova et al. 2013). However, they are often ignored in larger scaling and modeling studies (Downing et al., 2006, Downing, 2010; Lehner & Döll, 2004) because relationships to vegetation, water table depth and other parameters that can be scaled easily have not been identified. Recently, Kuhn et al. (2018) surveyed 52 ponds over a single growing season in two permafrost peatland mires located in northern Sweden. The ponds were classified into different types based on their vegetation dominance and hydrology and while ebullition was found to be highly variable among ponds, no significant difference in ebullitive flux was observed (Kuhn et al., 2018). Burke et al. (2019) focused their study of ebullitive emissions on eight ponds in the same region over the growing seasons of 2012 – 2015. They found ebullitive emissions to be highly variable between ponds and found the eight ponds to fall into four statistically different groups. Further scrutiny found these four groups, hereafter called pond types, to vary based on apparent physical characteristics, such as vegetation presence, depth, and hydrologic connectivity (Burke et. al., 2019). When looking at CH₄ emissions from water bodies above 50°N, lake type was found to be an important factor in determining emission potential (Wik, Varner et al., 2016) however the

categories included in this study were broad (e.g. peatland ponds was considered a single pond type). Additionally, though lake spatial area was not as important as depth and sediment type in driving flux per unit area, Wik, Varner et al. (2016) called for more studies to include the monitoring of physical characteristics along with areal extent of CH₄ emitting water bodies.

Earth observing remote sensing satellites, such as Landsat, have been used broadly in ecosystem scale modeling studies, and have been used extensively to assess water body size, particularly in rice paddy environments (Cohen & Goward, 2004, Dong et al., 2016; Zhou et al. 2016). However, remote sensing, particularly using satellites, is limited due to spatial resolution (Anderson & Gaston, 2013). For example, many satellite platforms have spatial resolutions too large to see water bodies smaller than 0.001 km² (Muster et al., 2012) making them difficult to use in studying temporal changes in thaw ponds. Unmanned aerial systems (UAS), offer a potential scaling stepping-stone between ground-based measurements and satellite imagery due to the increased spatial and temporal resolution, cost-effectiveness, and ease of use particularly in remote field areas (Chambers et al., 2007; Palace et al., 2018).

Mapping ponds on smaller spatial scales is also important for monitoring change over time (Kim et al., 2013). UAS technology has been used successfully to map and monitor melt ponds on glaciers in Nepal (Immerzeel et al., 2014; Miles et al., 2016) and on Arctic sea ice (Inoue et al., 2007; Wang et al., 2018; Tschudi et al., 2008), though few studies involve repeat measurements to look at change over time (Immerzeel et al., 2014 ; Miles et al., 2016; Tschudi et al., 2008). UASs provide researchers with the

ability to fly their field sites repeatedly, so they can capture important seasonal milestones, such as the melt and monsoon seasons (Immerzeel et al., 2014; Miles et al., 2016). Using UAS imagery collected in 2013 and 2014, Miles et al. (2016) was able to model the melting rate of a pond on Lirung Glacier and found it was large enough to likely contribute to substantial glacial abatement. Further, Immerzeel et al., (2014) used UAS imagery to model melting rate across the same glacier and found the melting rate around ponds was much higher than other parts of the glacier. The ease of use of UASs can often offer a much better alternative than more time and resource intensive field methods, especially when site accessibility is an issue (Immerzeel et al., 2014).

The purpose of this work is to monitor pond size over time at a rapidly changing permafrost peatland area in northern Sweden and determine potential relationships of changing pond size to ebullitive CH₄ emission. This site has been found to have varying CH₄ flux rates from ponds of differing type (Burke et al., 2019). In order to better understand how these ponds are changing over time, we monitored the spatial area of seven ponds using a high-resolution UAS equipped with a RGB (three channel red, green, blue) camera multiple times across the growing season over a three-year period. We also took advantage of UAS imagery collected in July over the whole site in recent years to expand our dataset to five growing seasons. We then compared the spatial extent of the ponds estimated from high resolution UAS imagery to measured rates of ebullitive CH₄ flux.

2.2 Methods

2.2.1 Study Site

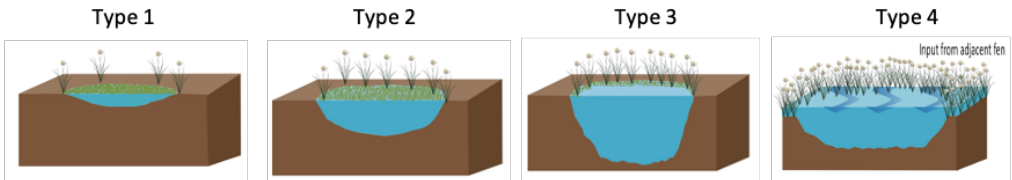
This study focuses on the Stordalen Mire complex located 10 km east of Abisko, Sweden (68°22'N, 19°03'E; Figure 2.1). Northern Sweden has experienced mean annual temperatures above 0°C since 2000, leading to the destabilization of underlying permafrost in the region (Callaghan et al., 2010; Kuhn et al., 2018). This research site contains the following four subhabitats: dry tundra plateaus underlain by permafrost, *Sphagnum spp.* dominated semi-wet areas, *Eriophorum spp.* dominated wet areas and collapsed features that accumulate water (Johansson et al., 2006, Malmer et al., 2005), hereafter called thaw ponds (Christensen et al., 2004). In previous work, eight thaw ponds within Stordalen mire were measured for CH₄ ebullitive emissions across several growing seasons (Burke et al., 2019), seven of which are the focus of this study.

High resolution meteorological measurements at Stordalen Mire have been collected since 2013 and maintained by the Swedish network of the Integrated Carbon Observation System (ICOS), a European infrastructure for measuring the C balance across Europe (http://www.icos-sweden.se/station_stordalen.html). Measurements from their WeatherHawk Series 500 system (WeatherHawk, Logan, UT) that is mounted on top of the ICOS instrument shelter at Stordalen Mire (4 m above ground level) and has measured air temperature, relative humidity, barometric pressure, solar radiation, rain, wind direction and wind speed averaged over 10-minute intervals since 2013.

2.2.2 Measurements of Methane Ebullition from Thaw Ponds

Measurements of ebullition were collected from seven ponds during the growing season (June – August) of 2012 to 2018 using simple floating funnels following the methodology of Burke et al. (2019). The funnels were sampled for the accumulated gas on a daily to weekly basis, with 84% of measurements collected within 3 days or less (2012 - 2018). Samples collected were run on a gas chromatograph equipped with a flame ionization detector (GC-FID, Shimadzu 2014) to get CH₄ concentration and rates of daily ebullitive flux were calculated based on the concentration, volume sampled and time between sampling periods (see Burke et al., 2019 for more details). Based on statistical results from our previous study (Burke et al., 2019), the ponds fell into four groups, which were related to apparent physical differences between ponds (Table 2.1, Figure B.9; see Burke et al., 2019 for full descriptions of each pond, and the four pond types). The ponds varied in vegetation presence, depth and hydrologic connectivity with some of the funnels deployed in ponds containing floating *Sphagnum spp.* while other ponds contained no floating vegetation (Burke et al., 2019).

Table 2.1 Modified Table from Burke et al. (2019) (Table 1.1). Physical characteristics of ponds sampled at Stordalen Mire, Abisko, Sweden between 2016 – 2018. Based on statistical differences in ebullitive flux, the ponds fall into four groups (see Figure A2.9): These groups, hereafter called types, differ in apparent physical characteristics: (1) shallow with low sedge (*Carex spp.* & *Eriophorum spp.*) presence, (2) intermediate depth and increased sedge presence, (3) deepest and sedge dominated, and (4) intermediate depth, open water and flow through present. The check marks mean that plant species is present, the x marks mean that plant species is not present. Hydrologic status is based on the work done by Olefeldt & Roulet (2012). See Burke et al. (2019) for more detailed description of each pond and pond type.



Pond	A	B	C	D	E	F	H
Average Depth (cm)	22	18	35	41	85	43	41
<i>Sphagnum spp.</i>	✓		✓		✓		X
<i>Eriophorum spp.</i>	✓		✓ (> type 1)		✓ (> type 2)		✓ (> type 3)
<i>Carex spp.</i>	X		X		✓		✓ (> type 3)
Median pH \diamond	4.1	3.8	4.3	4.5	3.8	4.3	5.9
Hydrologic status *	Isolated		Transitioning		Isolated		Open Water - connected to adjacent fen

* Classification based on Olefeldt et al. (2012).
 \diamond pH was measured during the 2013 and 2014 sampling seasons. Median pH is presented due to low number of measurements available in 2014.

2.2.3 Imagery Collection

Tie points made from Styrofoam wrapped in yellow tape and forming a large X (~1m × 1m) were placed around the ponds and used for georectification (Figure 2.1, inset). Considering the compact nature of the areas of interest, no more than three to five tie points were placed around each pond. The center of each tie point was recorded as a waypoint using a highly accurate differential GPS system (Trimble® Geo7X handheld unit (H-Star) with Floodlight™ technology used with a Trimble® Tornado external antenna, accuracy ± 12 cm). Tie points were initially placed in June of each field season

and were removed at the end of the field season in August; their GPS locations were collected once each field season, usually in August.

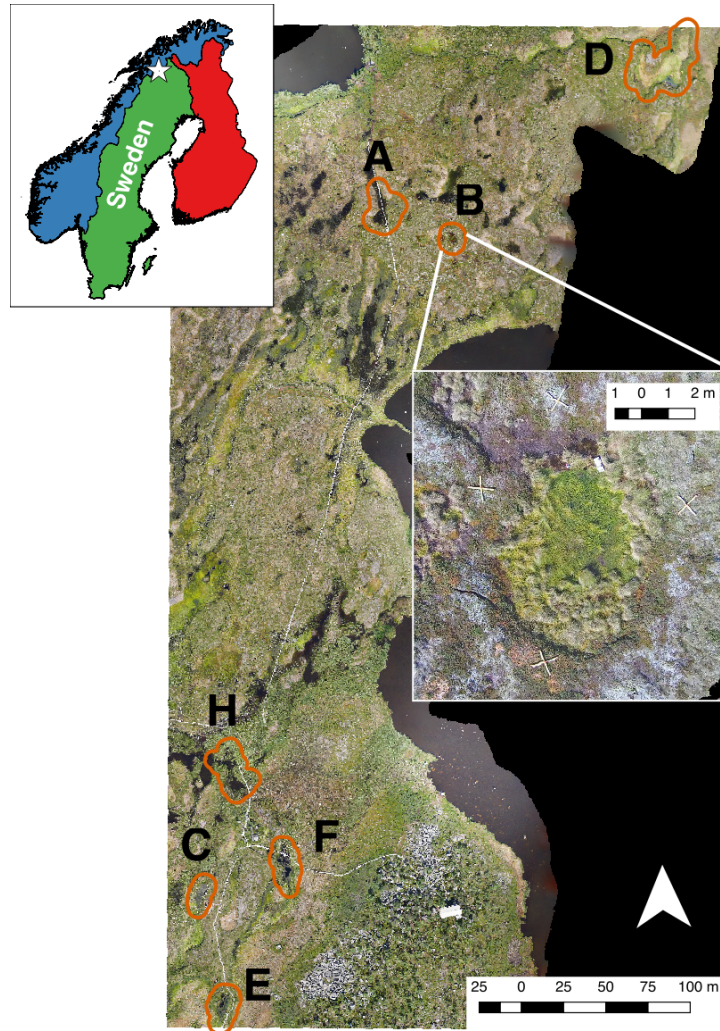


Figure 2.1 Modified from Burke et al. (2019) (Figure 1.1). Orthomosaic image of Stordalen Mire, Sweden ($68^{\circ}22'N$, $19^{\circ}03'E$) with pond sites marked. The image was collected using a fixed wing UAS in July of 2016 (DelGreco, 2018; Palace et al., 2018). The fixed wing image was provided by Jessica DelGreco, Michael Palace and Christina Herrick. The seven ponds focused on in this study are outlined in orange and labeled with their corresponding letter. Inset image of Pond B, collected using a quadcopter UAS July 2018, shows the yellow X tie points placed around each pond used for georeferencing. The quadcopter image was provided by Sophia Burke and Kathryn Bennett.

Imagery of the seven ponds was collected using a quadcopter and a fixed wing airplane. Most of the images ($n = 139$ out of 144) were collected in .mp4 format using a Yuneec® Q500 quadcopter UAS equipped with a gimbal RGB camera, flying on

average every week during the 2016, 2017 and 2018 growing seasons. The UAS was flown at an altitude of fifteen to twenty meters to ensure that all tie points were visible in the video and adequate coverage of vegetation surrounding the pond could be visible. The UAS was flown only during calm days with no rain, which limited the number of flights made particularly during the 2017 growing season.

2.2.4 Orthorectification

After quadcopter image collection, individual frames were extracted from each .mp4 video (Free Video to JPEG Converter, DVDVideoSoft) at a rate of one per half second. Images collected during individual flights over each pond were loaded into Photoscan Pro 1.2 by AgiSoft (AgiSoft LLC, St. Petersburg, Russia) where a camera calibration was performed using a pixel size of 0.0013×0.0013 mm and a focal length of 5.0 mm. The images were initially aligned using high accuracy and generic preselection settings. Then the image projections were sorted in descending order followed by the removal of all images with projections less than 100. Then additional photo alignments were performed until all images had projections greater than 100. A dense point cloud was built using medium quality and aggressive depth filtering settings, followed by a mesh with height field surface type and dense cloud source data (interpolation enabled) settings. Lastly, an orthomosaic was rendered using a planar projection (because the images would not be georeferenced within AgiSoft), mesh surface and mosaic blending mode parameters, with color correction enabled. Orthomosaics were exported as JPEG images. A total of 139 orthomosaics were created from the quadcopter imagery collected across the three sampling seasons.

Each July of 2014 through July 2018, images of the larger Stordalen Mire area were collected using a fixed-wing UAS (n = 5 ;Triton XL, Robota, Lancaster, TX) equipped with a built-in camera and was flown at an altitude of seventy meters the full extent of the mire using a preset flight plan (Goose™ autopilot program, Robota; see Palace et al., 2018 for complete methodology). Orthomosaic imagery collected with the fixed-wing UAS was rendered using the methodology described in detail in Palace et al. 2018. Both sets of imagery, quadcopter and fixed-wing, had a spatial resolution of 3 cm (DelGreco, 2018; Palace et al., 2018).

2.2.5 Georectification

Orthomosaic images collected with the quadcopter were next georeferenced in QGIS 2.14 (QGIS Development Team, 2020) using the Georeferencer GDAL plugin. Separate QGIS projects were created for each field season, with the collected GPS points loaded in with the coordinate reference system (CRS) set to EPSG:4326, WGS 84. On the fly CRS transformations was enabled for the project, with the CRS for the world set to EPSG: 32634, WGS 84/UTM 34N. Orthomosaic images were georeferenced using a first polynomial transformation algorithm with cubic resampling. The target spatial reference system for each image was set to EPSG:32634. Reports were generated for each initial georectification. If multiple images of a pond were available in a sampling season, the raster with the lowest average of the tie point residuals (a metric for the accuracy of each tie point georectification) was considered the 'Best of' image, with few exceptions (e.g. image showed incomplete coverage of the pond or there was distortion in the image; Table B.1). The remaining images of that

pond collected in the same sampling season, were then re-georeferenced, using the 'Best of' image as the target. Additional ground control points were added to the remaining images, by marking the ends of each tie-point, based on matching points in the 'Best of' image. If the images contained boardwalk, matching crosshatches were marked in the remaining images based on their location in the 'Best of' image. Updated output rasters were created for the remaining images, following the same transformation settings.

2.2.6 Pond Edge Polygons and Water Polygons

Each stitched image was delineated by hand using QGIS 2.14 (QGIS Development Team, 2020). Two polygons were drawn over each georeferenced orthomosaic (Figure 2.2). One polygon delineated the location of the pond's edge, defined by the distinct edge where collapse due to thaw was occurring. The other polygon marked the location of the water's edge, defined as where open water appeared to be in the orthomosaic. This proved difficult to define in areas where submerged vegetation was present. Vegetation type was of help in defining certain edges as certain types of vegetation prefer waterlogged conditions than others and were included in the water polygon (e.g. *Carex spp.*; Malhotra & Roulet, 2015; Malmer et al., 2005).

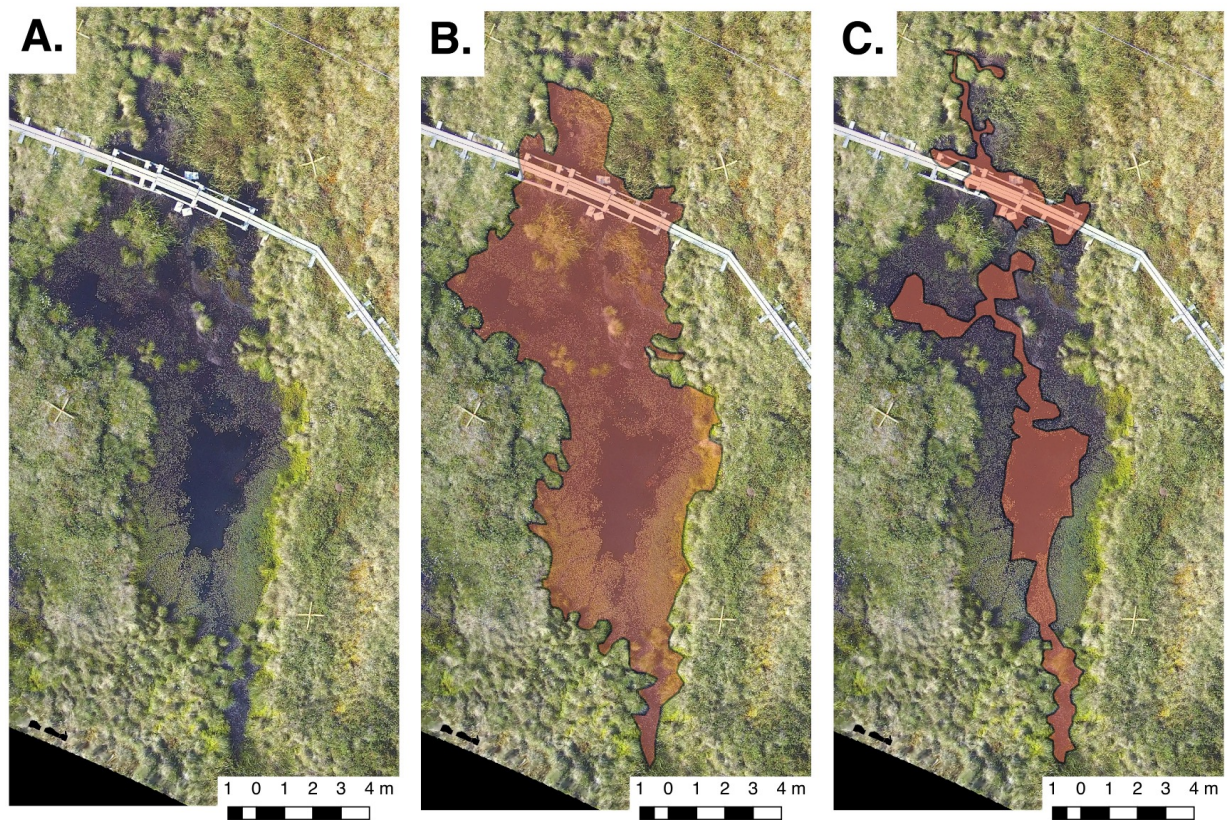


Figure 2.2 Orthomosaic of Pond F (panel A) with pond edge polygon overlaid (panel B) and water polygon overlaid (panel C). The pond edge polygon represented where the thawed areas met the intact areas. The water polygon represented where the water currently was within the pond. The boardwalk is visible in each panel, along with the yellow tie points used for georeferencing.

For ponds that were of type 4, meaning they had flow through them, pond edge was defined as where open water occurred. Once all the polygons were drawn ($n = 337$, 275 from the quadcopter imagery, 62 from the fixed wing imagery), the polygons were merged into a single shapefile and then the field calculator was used to calculate area, the length of the edge or perimeter, and the ratio between edge and area for each polygon. Then the attribute table of the merged shapefile was exported to a .csv file for statistical analysis.

2.2.7 Statistical Analysis

Statistical analysis was performed in R 3.6.1 (R Core Team, 2019). Initial data exploration, following the protocol of Zuur et al. (2010), determined that non-parametric statistical tests would be the most appropriate, given the violation of several parameters of the key assumptions in parametric statistical analysis (collinearity, normality, equal variance, and autocorrelation). Kruskal-Wallis sums tests were performed to determine the variation in polygon area (both pond edge and water) between various categorical variables of interest (e.g. ponds, pond types, sampling months and sampling seasons). Post-hoc Dunn's tests were then performed to examine pairwise comparisons between variables (dunn.test package; Dinno, 2017). Further we found the statistical differences between area, edge, and the ratio between the two when compared on their own to other parameters (e.g. pond, pond type, month etc.) were marginal, so we chose to focus further statistical analysis on polygon area.

In order to relate polygon area to CH₄ flux, we looked at the temporal differences in flight dates across the 2016, 2017 and 2018 sampling seasons and found flight dates occurred on average around eight days apart. An eight-day moving window of median daily CH₄ flux (mg CH₄ m⁻² d⁻¹) and total flux over an eight-day moving window (mg CH₄ m⁻²) was calculated across the eight days leading up to, centered around, and following each drone flight date. Preliminary comparisons were conducted between these flux parameters and water polygon area and the most statistical significance was found when median centered flux was used. Therefore, we performed all further statistical testing with regards to CH₄ using the median centered daily flux. To investigate the influence of precipitation on water polygon area, we used high temporal resolution

precipitation data (measured every ten minutes), collected at the field site (ICOS – WeatherHawk system), to calculate total precipitation accumulation over Stordalen Mire in the seven days leading up to and including each flight date. Non-parametric Kendall correlation tests were used to investigate relationships among pond size and various continuous variables of interest (e.g. flight date, total precipitation accumulation before flight). We chose a similar approach to approaching the interpretation of Kendall correlation tests as Burke et al. (2019) by following criteria set out by Cohen (1988). Based on the absolute value of the resulting Kendall's tau (τ) statistic, correlations were classified as strong ($|\tau| \geq 0.5$), moderate ($0.3 < |\tau| < 0.5$), or weak ($0.1 < |\tau| < 0.3$; Cohen, 1988). We considered the strength of the correlation to be very weak if the $|\tau|$ was less than 0.1, regardless of whether the p -value was statistically significant.

2.3 Results

2.3.1 Spatial Variability in Pond Area

Based on imagery collected using the quadcopter UAS, area of both pond edge and water polygons varied significantly by pond ($p < 0.0001$, Figure 2.3). Among pond edge polygons, most of the ponds ranged between 25.9 to 219 m², except for pond D, which ranged in size between 411.3 and 533.4 m². The smallest pond measured was pond B, with a median pond edge area of 34.5 m², and the largest was pond D, with a median pond edge area of 476.3 m².

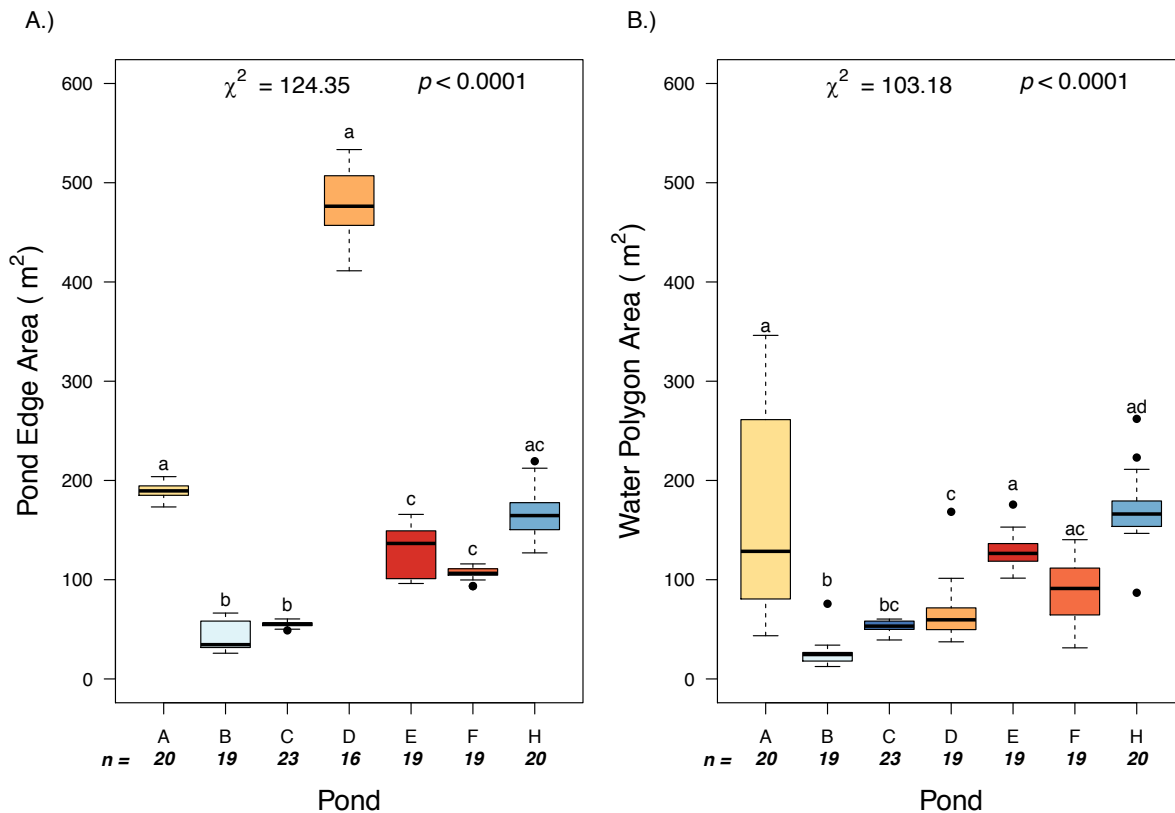


Figure 2.3 Pond edge area (A.) and water polygon area (B.) of ponds from quadcopter UAS imagery collected at Stordalen Mire in 2016, 2017 and 2018 field seasons. N values displayed below each pond indicate the number of images represented in each boxplot. Black lines represent median values, and black circles represent outliers. Lowercase letters represent significant differences between ponds. Results of the Kruskal Wallis ranks sum test are displayed as χ^2 and p values.

Among water polygons, the smallest areas were again measured at pond B, with a median water area of 24.6 m². The largest fluctuation or most variable water area was pond A, with a minimum area of 43.5 m² and maximum area of 346.2 m². Overall variability in water polygon area was found not to be significantly related to the amount of precipitation accumulated within the eight days before each flight (Figure B.2). When the variability in water polygon area of each pond individually was compared to precipitation accumulation before each flight, pond B was found to have a significant

relationship ($p = 0.002$, $\tau = 0.50$), however this appears to be driven by a single point (Figure B.3).

2.3.2 Seasonal Variability in Water Polygon Area

To explore seasonal variability among ponds, we chose to focus on water polygon area, as this acts as a proxy for water contained in each pond during the season. When all water polygon areas are grouped together by month, no significant difference is seen across the sampling season (Figure 2.4), yet when water polygon area across the sampling season is explored in each pond individually, pond A shows a significant difference between months (Figure B.5). The lowest median water polygon areas were observed in June, at 69.5 m² and the highest median areas were observed in July, at 86.8 m², followed closely by August, with median area of 82.7 m² (Figure 2.4).

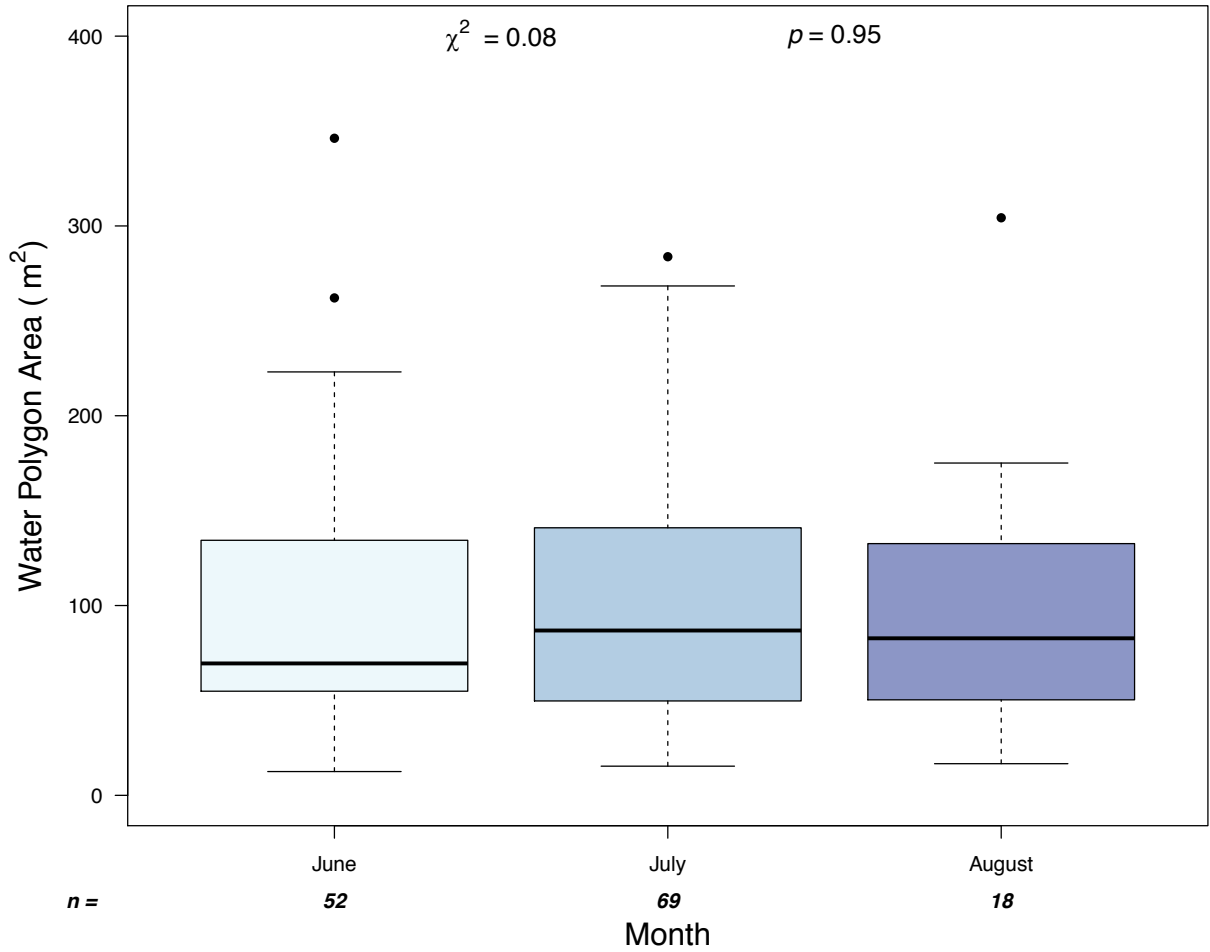


Figure 2.4 Variability in water polygon area among months in the sampling season from imagery collected at Stordalen Mire using the quadcopter drone in 2016 to 2018 field seasons. N values displayed below each month indicate the number of images represented in each boxplot. Black lines represent median values, and black circles represent outliers. Results of the Kruskal Wallis ranks sum test are displayed as χ^2 and p values.

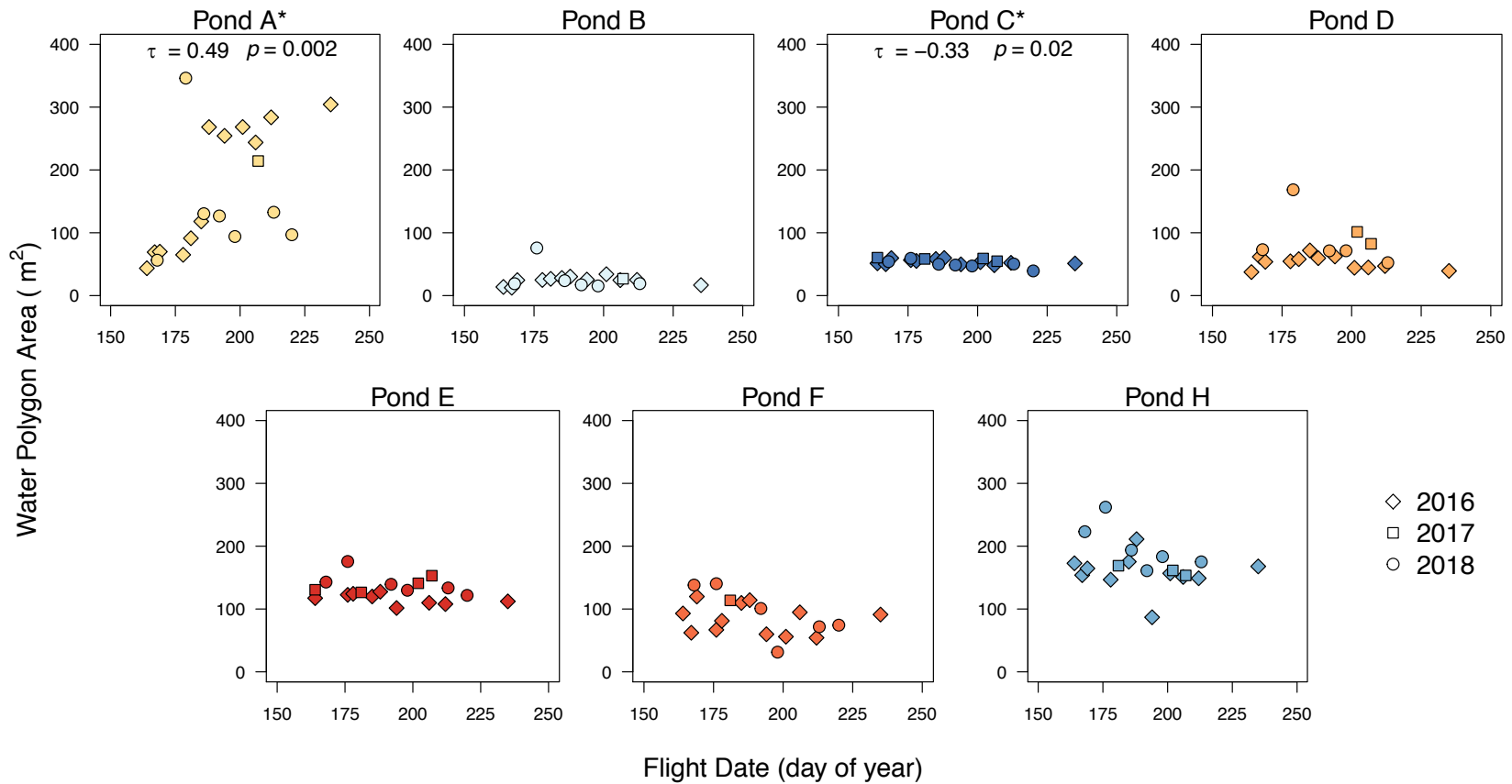


Figure 2.5 Variability in water polygon area (m²) across the sampling season (day of year) from quadcopter imagery. Each pond is displayed with a different color. The different shapes represent different sampling seasons. Kendall rank sum tests were performed on each pond, with ponds showing a significant relationship indicated by the * next to their name. Those that were significant also have their p value and τ displayed.

This follows the pattern in monthly average precipitation, with June having the lowest average precipitation and July having the highest when 2016, 2017 and 2018 sampling seasons are looked at together (Table B.2). When the variability in water polygon area across the sampling season is explored in each pond individually, the ponds overall had stable water polygon areas over the course of the season with the exception of pond A which is the only pond found to significantly differ in area with an increase over the season ($p = 0.002$, $\tau = 0.49$, Figure 2.5). When flight date is treated as a continuous variable, water polygon area is found to vary significantly across the sampling season in pond C with a decreasing area, though small, over the growing season (Figure 2.5).

2.3.3 Fixed Wing vs. Quadcopter Platforms: Water Polygon Area

To test the validity of using both the fixed wing and quadcopter imagery together in a time series analysis, we compared the pond edge areas from fixed wing imagery in 2016, 2017, and 2018 to the average of pond edge areas from quadcopter imagery in the same years (Figure 2.6). We found a strong significant agreement in areas measured between the two UASs ($\tau = 0.90$, $p < 0.0001$, Figure 2.6A), which provided support for our inclusion of fixed wing imagery from 2014 and 2015 in statistical analysis of interannual variability of pond edge and water areas.

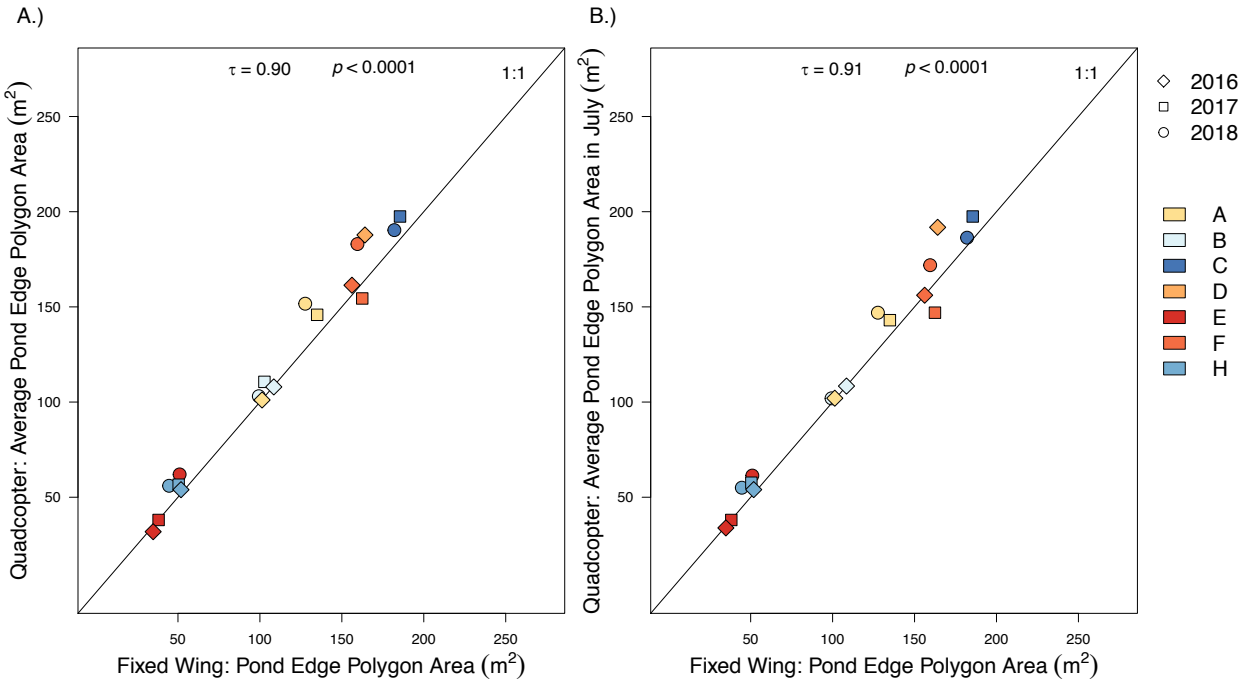


Figure 2.6 Comparison of pond edge polygon area from fixed wing imagery collected in July to the average pond edge polygon area measured from quadcopter imagery collected across the whole sampling season (A.) or in July (B.). The different shapes represent different sampling season and the different colors represent the different ponds. Results of a Kendall correlation test are presented as τ and p values. A 1:1 line is also displayed as a solid black line.

I also looked at this relationship with quadcopter imagery collected only in July and found the relationship to be slightly stronger ($\tau = 0.91$, $p < 0.0001$, Figure 2.6B). A similarly strong relationship was also seen when comparing water polygon areas measured from fixed wing imagery versus quadcopter imagery across the season and only in July (Figure B.5).

2.3.4 Interannual Variability in Pond Edge Area

In exploring interannual variability, we chose to focus on pond edge area, as this represents the extent at which thawing has occurred in the pond. Similar to the overall relationship of water polygon area in different months, pond edge area did not vary significantly among sampling seasons (Figure 2.7). However, the median pond edge

area does increase steadily across years, despite no significant difference between sampling seasons.

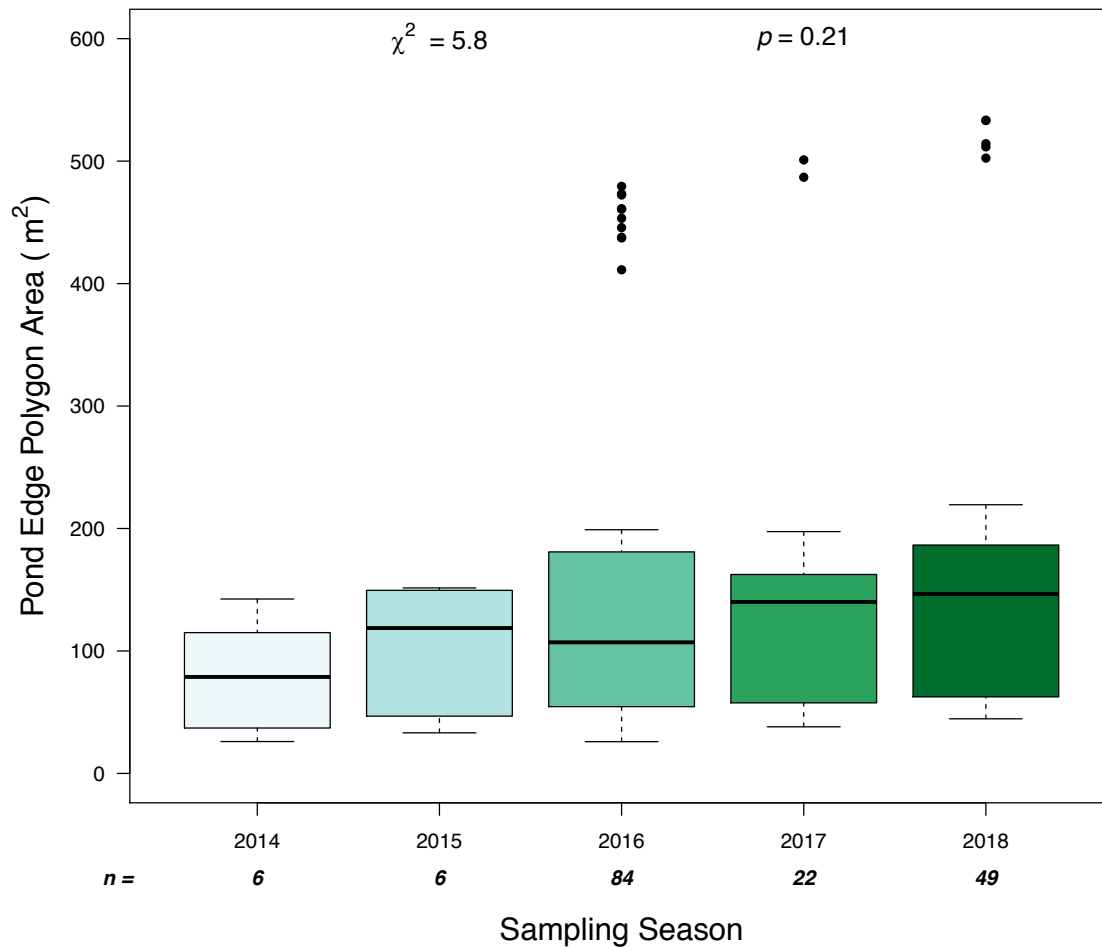


Figure 2.7 Variability in pond edge polygon area among different sampling seasons from both quadcopter and fixed wing imagery. N values displayed below each year indicate the number of images represented in each boxplot. Black lines represent median values, and black circles represent outliers. Results of the Kruskal Wallis ranks sum test are displayed as χ^2 and p values.

Lowest median pond edge area was seen in 2014, at 78.9 m². The highest median pond edge area was measured in 2018 was almost double that of 2014, at 146.5 m² (Figure 2.7).

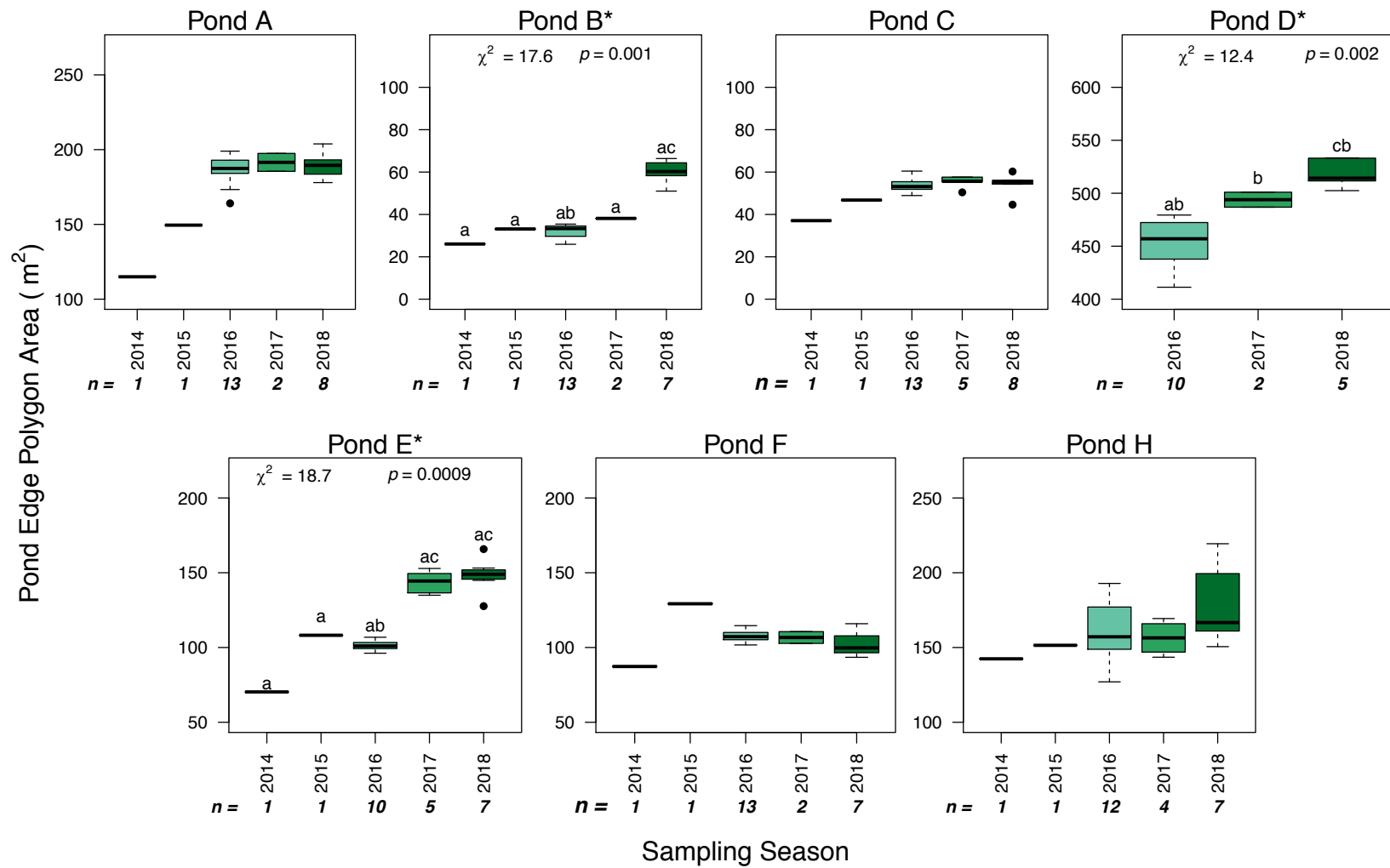


Figure 2.8 Variability in pond edge area by sampling season from both quadcopter and fixed-wing imagery. Note the differences in scale of the y-axis between subplots. N values displayed below each month indicate the number of images represented in each boxplot. Black lines represent median values, and black circles represent outliers. Lowercase letters represent significant differences between sampling seasons. Results of the Kruskal Wallis ranks sum test are displayed as χ^2 and p values.

The range in pond edge area was also smallest in 2014, ranging between 26 m² and 142.4 m² while in 2016 the range in pond edge area was between 25.9 m² and 479.4 m². And as with seasonal variability, when interannual variability is broken up by pond significant relationships begin to emerge (Figure 2.8). Pond edge area in ponds B, D, and E were found to vary significantly by sampling year ($p = 0.0009 - 0.001$, Figure 2.8). In all cases, pond edge area in 2018 was significantly larger than 2016 (Figure 2.8). In pond E, 2016 and 2017 were also found to be significantly different from each other, with pond edge area in 2017 significantly higher than 2016 (Figure 2.8).

2.3.5 Pond Area and Ebullitive CH₄ Emissions

Comparison of polygon area to ebullitive CH₄ emission from our studied ponds was done by calculating a median daily ebullitive flux (mg CH₄ m⁻² d⁻¹) across an eight-day moving window that was centered around each flight date (this included the three days preceding and the four days following each flight date). We chose to present median daily flux in this study as averages tend to swamp out the variability that is apparent in ebullitive emissions. Median daily ebullitive flux was found to vary significantly by pond ($p < 0.0001$, Figure 2.9).

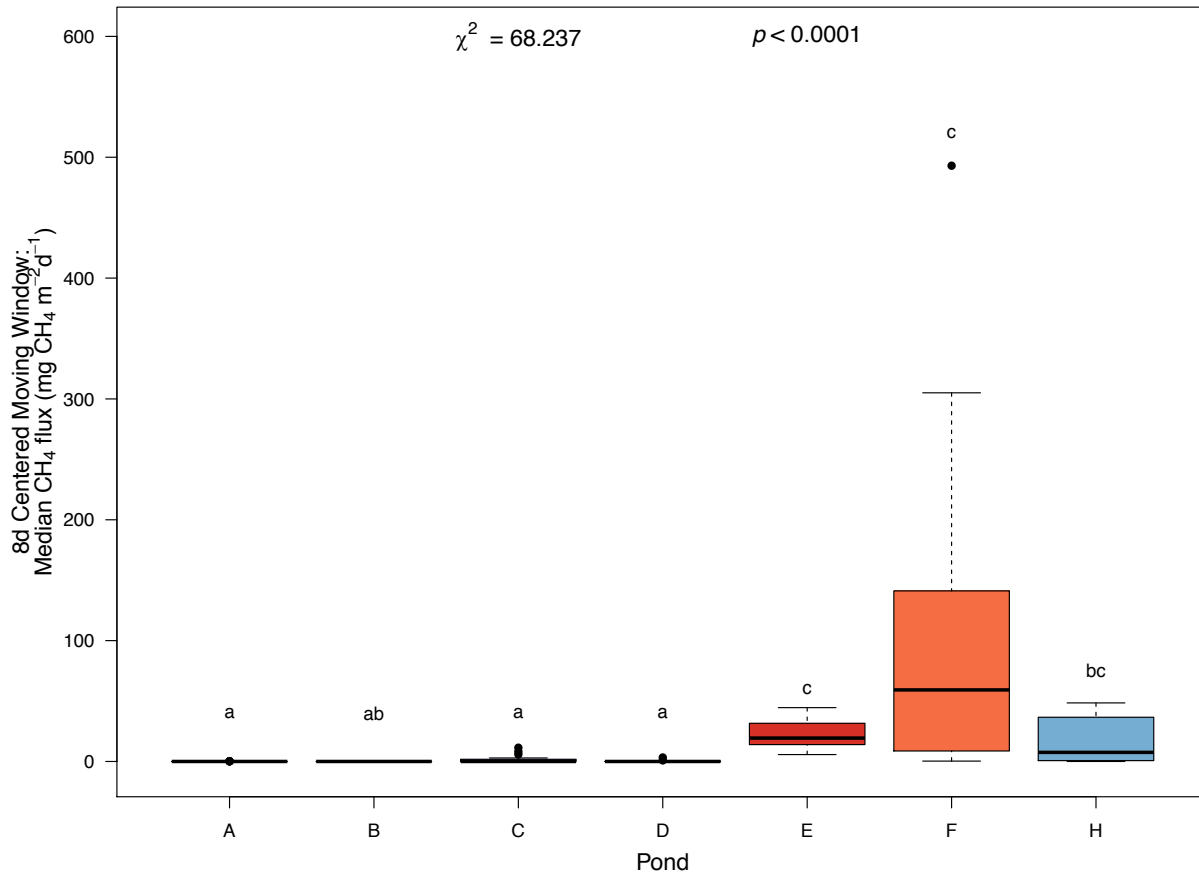


Figure 2.9 Modified from Burke et al. (2019) (Figure 1.3). Median daily ebullitive flux calculated across an eight-day moving window that is centered around each flight date during the 2016 – 2018 sampling seasons. Black lines represent median values, while black dots represent outliers. Lowercase letters represent significant differences between ponds. Results of the Kruskal Wallis ranks sum test are displayed as χ^2 and p values.

Burke et al. (2019) found daily ebullitive flux to vary significantly between ponds, creating four distinct groups, and contributed this significant difference to the varying physical characteristics between ponds that included vegetation presence, depth and hydrologic connectivity (Table 2.1; see Burke et al. 2019 for complete description of the pond types). Ponds A & B fall into type 1, ponds C & D fall into type 2, ponds E & F fall into type 3 and pond H is part of type 4. Pond G was not included in this current study due to sampling access limitations described in Burke et al. 2019. When the ponds are

placed into these statistically predetermined pond types, water polygon area was found to vary significantly (Figure 2.10). Pond types 1 and 2 were smaller and differed significantly from types 3 and 4. Pond edge area was also found to vary significantly by pond type, though the relationship wasn't as strong ($\chi^2 = 8.2$, $p = 0.04$, Figure B.6). The lowest median water polygon area was seen in type 2, at 54.65 m² followed closely by type 1, at 56.3 m², with the largest median water polygon area seen in pond type 4 at 166.2 m². Type 1 had the largest range in water polygon area (12.5 – 346.2 m², and this is due to its inclusion of pond A, which saw the largest range in water polygon area (Figure 2.3B).

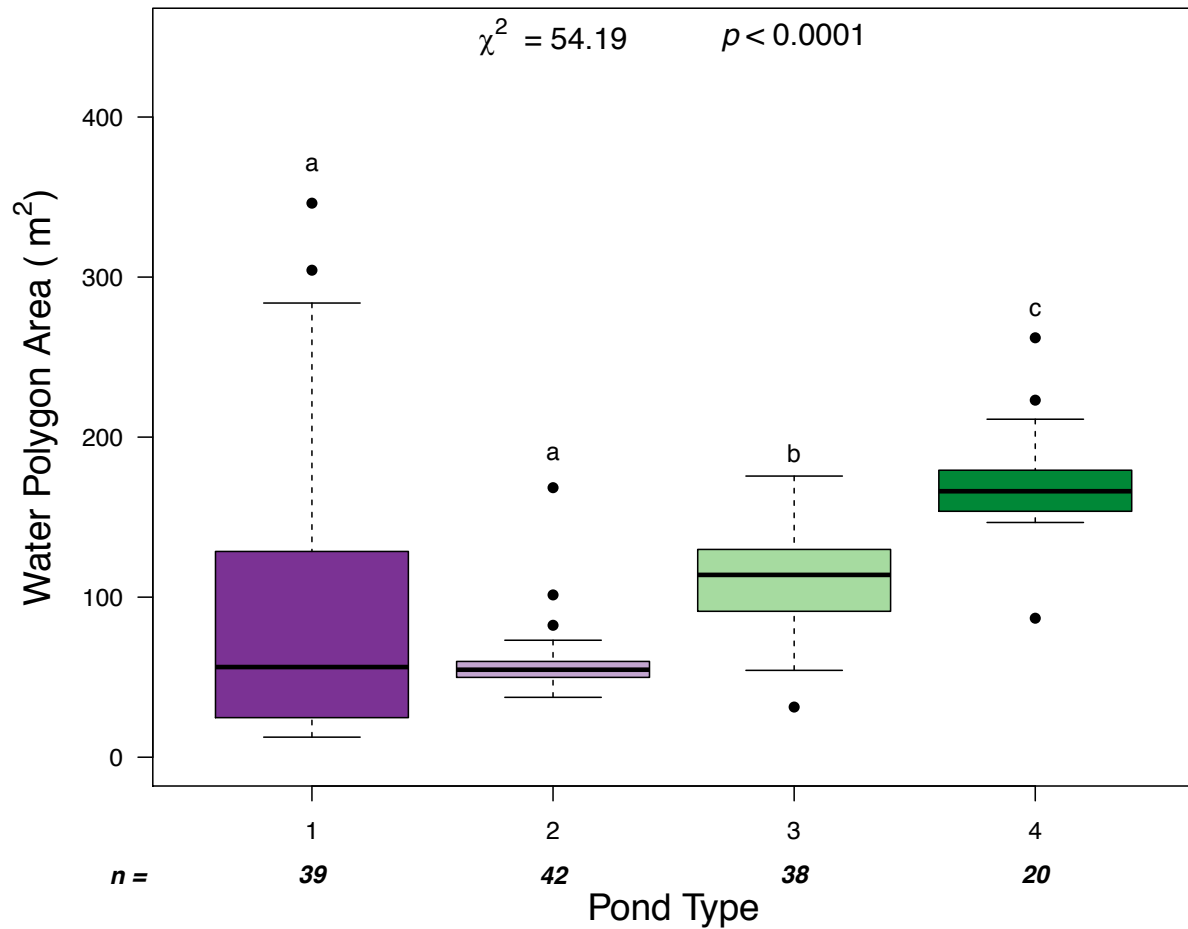


Figure 2.10 Water polygon area from quadcopter imagery among the different pond types. Black lines represent the median values of each boxplot and the black lines represent outliers. N values below the x axis represent the number of images included in each boxplot. The different colors represent the different pond types. Of the seven ponds studied, two ponds fell into types 1,2, and 3 with one pond in type 4. See Burke et al. 2019 for a complete description of each pond type. Results of the Kruskal Wallis ranks sum test are displayed as χ^2 and p values.

Seasonal variability of pond water area was observed by pond type (Figure 2.10).

However, water polygon area within a pond type was not found to vary significantly

(Figure 2.11). Despite this lack of significance, water polygon area does appear to

increase over the sampling season within pond type 1, while in all other pond types the

opposite trend is seen. It is important however to note that the lowest number of UAS

flights were conducted in August (Figure 2.11).

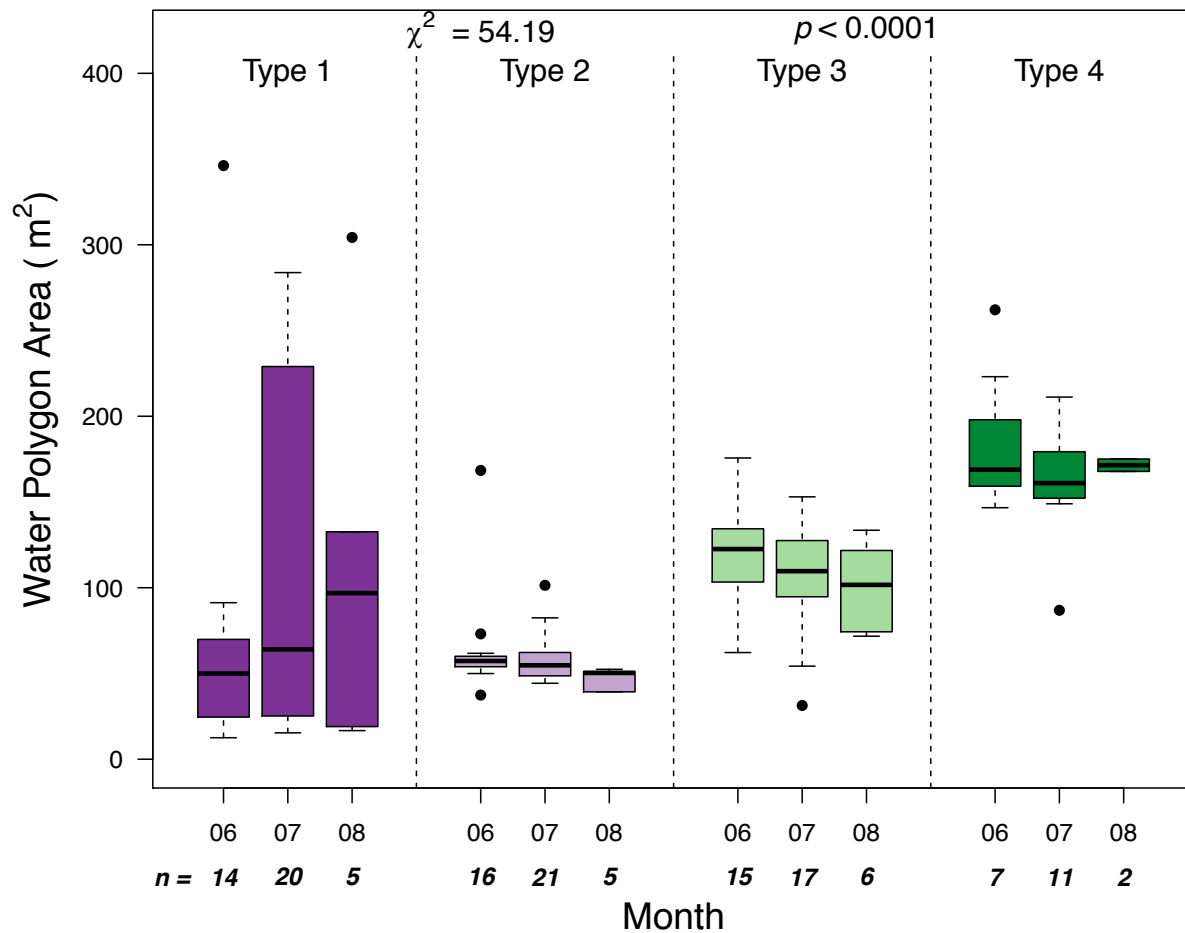


Figure 2.11 Water polygon area of differing pond types by month. The black lines represent the median values of each boxplot and the black dots represent the outliers. N values below each pond type represent the number of images included in each boxplot. The colors represent the different pond types. Results of the Kruskal Wallis ranks sum test are displayed as χ^2 and p values.

Interannual variability in pond edge area among the different pond types was explored using both quadcopter and fixed wing imagery but no significant difference was seen between pond edge area and sampling season among the four pond types (Figure B.7). However, similarly to the overall lack of significance found between pond edge area and sampling season (Figure 2.7), median pond edge area increased between 2014 and 2018 in all pond types (Figure B.7).

We also explored the relationship between pond edge area and total annual CH₄ flux and found annual ebullitive flux appears to be largest in ponds with pond edge areas ranging between 50 – 150 m², and ponds that were both smaller and larger in pond edge area emitted lower amounts of CH₄ on annual basis (Figure 2.12).

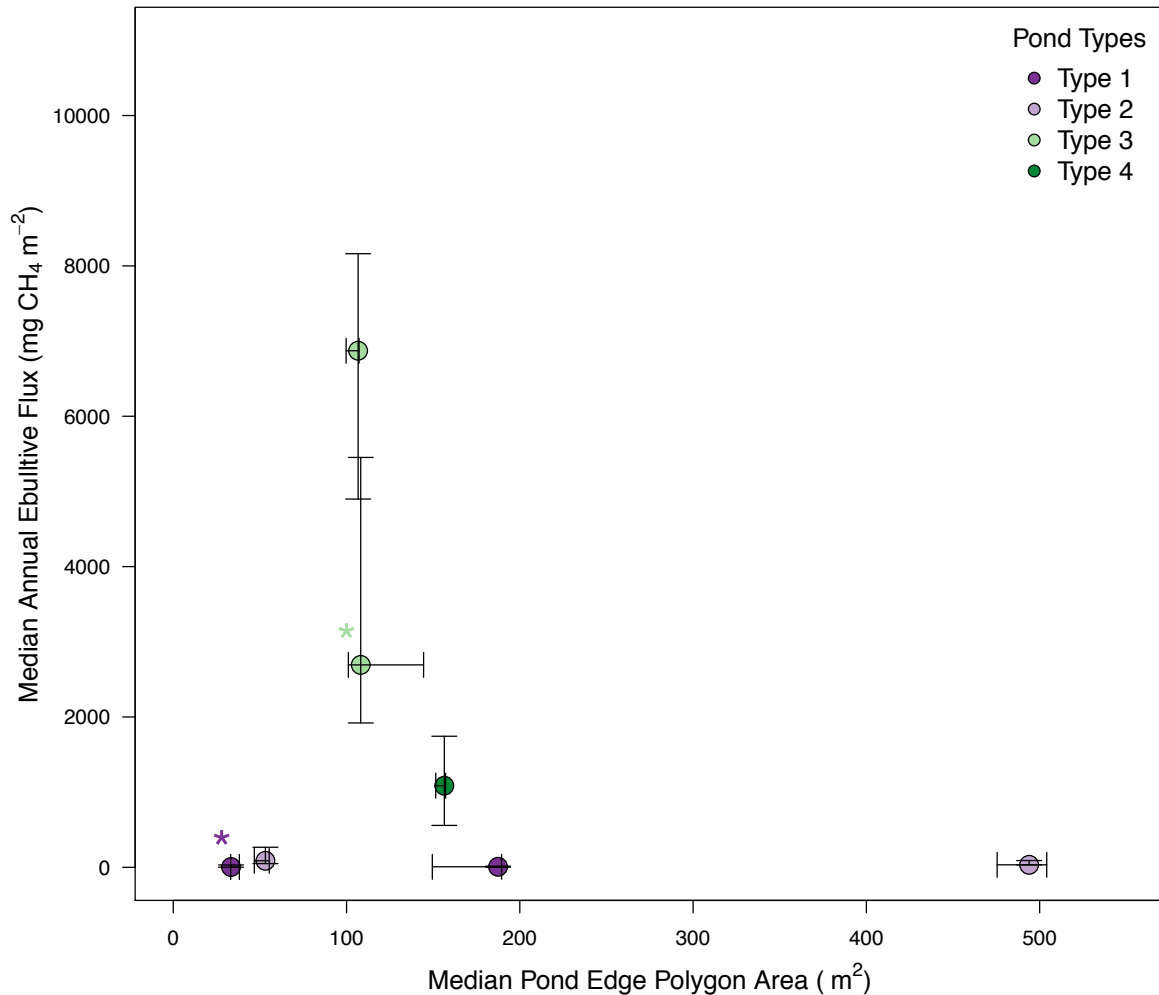


Figure 2.12 Median pond edge area (m²) compared to median annual ebullitive flux (mg CH₄ m⁻² d⁻¹) of the seven ponds in this study. Colors represent the pond type of each pond. The Asterix denote which ponds show significant differences in annual ebullitive flux with pond edge area (see Figure B.8 in the appendix) Median pond edge area includes both quadcopter and fixed wing imagery. Error bars represent 25th and 75th percentiles of both pond edge area and annual ebullitive flux.

Significant relationships among cumulative annual ebullitive flux and pond edge area were found among certain ponds. Pond B was found to have a positive relationship,

suggesting larger total annual flux was measured when a larger pond edge area was measured ($\tau = 0.58$, $p = 0.02$; Figure B.8). Pond E however, showed a negative relationship to pond edge, suggesting lower total annual flux was measured from ponds with larger pond edge areas ($\tau = -0.57$, $p = 0.0004$; Figure B.8).

2.4 Discussion

2.4.1 Using UAS platforms to monitor pond size over time

Our study found that interannually, all ponds appeared to increase in pond edge area between 2014 and 2018 however the magnitude of this change varied between ponds (Figure 2.8). While not in permafrost peatland areas, UAS technology has been used to measure melt pond area on the surface of Arctic sea ice (Inoue et al., 2008; Wang et al., 2018; Tschudi et al., 2008) and on the Lirung Glacier in Nepal (Immerzeel et al., 2014, Miles et al., 2016). However, few studies include repeat measurements to look at temporal changes (Immerzeel et al., 2014; Miles et al., 2016; Tschudi et al., 2008). Tschudi et al. (2007) used UAS imagery of sea ice near Barrow, Alaska and found the fractional cover of melt ponds to increase from 10% to 40% over the study period (Tschudi et al., 2008). In Nepal, Immerzeel et al. (2014) used repeat UAS flights during pre- and post- monsoon season in 2013 to identify surficial changes on Lirung Glacier. Melt ponds covered only 8% of the study area but were responsible for 24% of the melting that occurred during the study season (Immerzeel et al., 2014). Immerzeel et al., (2014) further noted the importance of continued long-term monitoring of such

features using a UAS in order to better understand the fate of glaciers like Lirung Glacier to climate change.

The importance of long-term monitoring holds true for permafrost peatlands such as Stordalen Mire, with the potential for drastic changes in hydrology and peatland subtypes in response to permafrost thaw (DelGreco, 2018; Johansson et al., 2006; Malmer et al., 2005; O'Donnell et al., 2011; Olefeldt & Roulet, 2012). When the ponds in this study are categorized by pond type, water polygon area varied significantly between ponds types across the season, with type 1 ponds increasing between June and August, and the remaining types appearing to have the opposite relationship (Figure 2.11). Ponds A and B are both type 1 ponds, positioned upon a palsa plateau (Figure 2.1), which have high rates of runoff, draining laterally towards more collapsed bog areas (O'Donnell et al., 2011; Olefeldt & Roulet, 2012) due to the relatively shallow thaw depth (O'Donnell et al., 2011). There is a potential for these ponds to shift to a different pond type, as permafrost continues to progress at this site, which could change how the ponds water area fluctuates over the season. This could also lead to changes to vegetation and hydrology which has already been seen at this site (DelGreco, 2018; Johansson et al., 2006; Malmer et al., 2005) and has implications for CH₄ flux if these ponds transition from Type 1 and 2 to 3 or 4 (Burke et al., 2019).

UAS technology has been used successfully in permafrost peatlands to monitor vegetation changes over time (DelGreco, 2018; Palace et al., 2018; Räsänen et al., 2019), however there was little focus on monitoring small water bodies. At Stordalen Mire, DelGreco (2018) used a four-year dataset of UAS imagery collected over

Stordalen Mire (collected in July of 2014 to July 2017) to investigate changes in vegetation cover types as permafrost thaws. Through this analysis, DelGreco (2018) found that over the four-year study period, Stordalen Mire became overall more wet, with intact permafrost areas reducing by almost 10% and semi-wet areas increasing by 18% resulting in an overall permafrost loss of 20% (DelGreco, 2018). In particular regard to open water, DelGreco (2018) found this to vary across the study period, with its highest extent occurring in 2015. In our study, we I saw an overall increase in median pond edge area of more than 50% between 2014 and 2018 sampling seasons (Figure 2.7). Most of the ponds in this study increased in pond edge area with each successive sampling season, except for pond F which measured its largest pond edge area also in 2015 (Figure 2.8). DelGreco (2018) suggested the variation in open water she saw was related to the presence of submerged vegetation in open water areas, which likely led to issues in the classification.

Due to the presence of submerged vegetation in many ponds in this study, with extensive *Sphagnum spp.* cover throughout, the ponds would likely be included in the semi-wet class from DelGreco (2018) and Palace et al. (2018), which further supported the need to hand-delineate our ponds. In addition, the high spatial resolution (3 cm) of both the fixed wing and quadcopter imagery made distinguishing the thawed edge of each pond fairly easy (Figure 2.2). Previous studies have used digital elevation models (DEM) to delineate wetlands, ponds and lakes using imagery produced using light detection and ranging (LiDAR) technology (e.g. Wu et al., 2019; Wu & Lane, 2017; Paine et al., 2015) as well as RGB cameras (Kraaijenbrink et al., 2016). Kraaijenbrink et

al. (2016) successfully used a UAS sourced DEM to delineate melt ponds on Lirung Glacier in Nepal, however they were likely delineating much deeper ponds than in our study (the deepest one measured by Kraaijenbrink et al. (2016) was ~9 m) which made the 0.2 m resolution of their DEM better suited. Attempts were made to delineate ponds in this study using DEMs created in AgiSoft from the quadcopter imagery, however the DEMs were found to be ineffective for the very shallow ponds like pond B (< 20 cm; Figure B.1).

2.4.2 Interannual variability in thaw pond size and its impact on CH₄ emissions

We found the annual CH₄ emission from the thaw ponds in this study to vary by pond edge area, with the largest annual emissions from ponds between 50 and 150 m² (Figure 2.12). Several recent studies have observed an inverse relationship between dissolved CH₄ concentration with pond size (Shirokova et al., 2013, Polishchuk et al., 2018, Holgerson & Raymond, 2016) which suggests an increase in emission of CH₄ from permafrost zones due to the potential increase in the number of small thaw ponds (Shirokova et al., 2013). Through the use of historical satellite data, Walter et al. (2006) found lake area to increase by almost 15% in their study region in Northern Siberia, which they estimate to have led to a ~ 60% increase in CH₄ from this region. It is important to note however that many upscaling studies such as Walter et al. (2006), neglect small ponds (areas < 0.001 km²) in their estimates due to the limited spatial resolution of satellite platforms (Anderson and Gaston, 2013; Muster et al., 2012).

In our study, we saw variability in CH₄ emissions with pond size and while our largest pond emitted less CH₄ per unit area than some of its smaller counterparts, while the smallest ponds measured also emitted the least CH₄ per unit area (Figure 2.12). This difference in emission is likely due to the physical differences between pond types. The smallest and lowest emitting ponds are shallow and isolated with little sedge present around its edges, while the higher emitting, though not the largest ponds are the deepest measured, have more sedge present around their edges (Figure 2.12; Burke et al., 2019). We also saw in some ponds an increase in annual ebullitive emission between years that did not include a change in pond edge area (e.g. pond F, pond C; Figure B.8). These changes in emission could instead be correlated with other physical changes in the ponds beyond changes in size, such as changes in vegetation (e.g. an increase in sedge presence, a plant that is known to promote CH₄ production and emission; Chanton et al., 2008; Kutzback et al., 2004; Noyce et al. 2014) or hydrology (e.g. ponds becoming more hydrologically connected to nearby fen areas; Johansson et al., 2006; Olefeldt & Roulet, 2012). Wik, Varner et al. (2016) reviewed published reports of CH₄ emissions from lakes above 50°N and found that lake type was an important factor in determining emissions potential, though lakes were categorized into broad groups which included beaver ponds, thermokarst lakes, glacial lakes and peatland ponds. They found CH₄ emissions from ponds to also decrease with increasing areal extent, though they only reported ebullitive emission from one peatland pond (Wik, Varner et al., 2016).

The ponds in this study, with spatial areas falling within the range of peatland ponds presented in Wik, Varner et al. (2016), also fall within the range of ebullitive emissions ($22 \text{ mg CH}_4 \text{ m}^{-2} \text{ d}^{-1}$; Figure B.9). Kuhn et al. (2018) calculated the net carbon balance (NCB) for Stordalen Mire, expanding on previous estimates by Bäckstrand et al. (2005) to include small ponds. With the help of areal imagery of the site, they estimated the areal extent of thaw ponds to increase from 1% in 2000 to 4% in 2015 and also concluded that adding thaw ponds in the NCB for Stordalen would shift the site closer to an overall C source, rather than a sink (Kuhn et al., 2018). However, the thaw pond area used neglected vegetated ponds completely and only included ponds with open water because they could be estimated more easily from areal imagery (Kuhn et al., 2018). The inclusion of areal estimates and emissions data from the mostly vegetated ponds in this study would likely result in a further improved NCB estimate for Stordalen. Understanding how ponds are changing in size and their distribution over time is essential for accurate modeling of CH_4 globally (Holgerson & Raymond, 2016), however monitoring the physical characteristics of ponds in tandem with their size is important in understanding their changing flux dynamics.

2.5 Conclusions

We collected UAS imagery of seven thaw ponds over five growing seasons, hand-delineating a total of 377 polygons of pond edge and water to assess change in pond size. Pond area increased overall across the study period indicating a general increase in wetness in this permafrost peatland, though the magnitude of change varied by pond. We also found CH_4 emissions to vary by pond size, with smaller ponds emitting more

CH₄ per unit area annually than larger ponds in this study, though we attribute this variability to differences in pond type (i.e. differences in vegetation and hydrology). Our results suggest that high resolution UAS imagery should be collected multiple times during the growing season in order to adequately capture the changing nature of these dynamic systems. UASs provide an excellent means of acquiring the necessary high-resolution imagery needed for the long-term monitoring of thaw ponds and should be used more readily in future studies. The importance of monitoring pond size over time remains essential for adequate modeling of CH₄ across the changing Arctic, however our results suggest that monitoring other pond characteristics, like pond type, in conjunction with size are important in understanding CH₄ emissions, and how they might change in the future.

CHAPTER 3: USING ACOUSTIC TECHNIQUES TO MONITOR CH₄ EBULLITION IN SUBARCTIC THAW PONDS³

3.1 Introduction

Arctic regions, particularly areas where there are significant amounts of organic carbon (C) stored in permafrost, are highly vulnerable to climate change. High latitude areas are known to be large sources of C to the atmosphere, particularly methane (CH₄) (Kirschke et al., 2013; Saunio et al., 2016), though how these emissions will change with rising global atmospheric temperatures remains unclear. Some suggest there could be an increase in overall emissions from arctic peatland areas due to increased thaw (Schuur et al., 2008), while others suggest that while the creation of new lakes due to thaw will increase CH₄ emissions, these emissions will be offset by vegetation, particularly in drained lakes (Turetsky et al., 2020). Northern peatlands store ~1000 Pg C within the top 3m of ground to be twice the amount originally thought (Hugelius et al., 2014). When these permafrost peatlands thaw, the OC stored within can be anaerobically broken down eventually into CH₄ (Stocker et al., 2013; Laurion et al., 2010; O'Donnell et al., 2011). Thaw ponds, which develop when permafrost peat thaws, slumps, and fills with meltwater (Bouchard et al., 2014; Negandhi et al., 2013; O'Donnell et al., 2011), are understood to be significant sources of methane to the atmosphere

³ The work in this chapter is currently in prep for submission to a peer-reviewed journal: Burke, S. A., Palace, M., Perry, A., Padilla, A., Herrick, C., Contosta, A. R., Weber, T., Crill, P. M., & Varner, R. K. In prep. Using acoustic techniques to monitor methane ebullition in subarctic thaw ponds. *Hydrology & Earth System Science or Environmental Science & Technology*.

(Negandhi et al, 2013; Walter et al., 2006; Wik, Varner et al., 2016), though there are few long-term studies available (Burke et al., 2019).

Ebullition, or bubbling, is often the dominant transport pathway of CH₄ out of anoxic environments yet is the least studied (Bastviken et al., 2011; Coulthard et al., 2009; Fechner-Levy & Hemond, 1996). Ebullition in waterbodies has been successfully measured using several techniques ranging in complexity and sampling resolution from daily manual sampling of floating funnels (Burke et al., 2019; Wik et al., 2013) to automated techniques utilizing submersible echo sounders (Jackson et al., 1998; Ostrovsky et al., 2008) and pressure sensors (Duc et al., 2019; Maher et al., 2019; Varadharajan et al., 2010). Monitoring ebullition is difficult because in addition to steady background emissions (Goodrich et al., 2011), ebullitive emission can also be episodic both spatially and temporally, making them hard to capture (Rosenberry et al., 2003; Varadharajan & Hemond, 2012; Walter et al., 2006). In addition, ebullitive flux is often represented as a daily flux measurement (e.g. mg CH₄ m⁻² d⁻¹) which implies a steady rate of emission across the day. However, studies have found significant diurnal variation in CH₄ emissions from ebullition (e.g. Bastviken et al., 2004; Goodrich et al., 2011). This suggests that the continuous monitoring of ebullitive emission is essential in order to accurately estimate fluxes, yet of the high resolution (sub-daily) studies of ebullitive emissions available, many are of one field season duration or less (Maher et al., 2019; Varadharajan & Hemond, 2012) or occur in oceanography studies monitoring methane seeps in the deep ocean (e.g. Dziak et al., 2018; Greene & Wilson, 2012; Wiggins et al., 2015).

Passive acoustics, which involves the placement of a listening device near an emission site, have been used in research to continuously monitor gas leaks (Bergès et al., 2015) as well as bubbling from oceanic methane seeps (Dziak et al., 2018; Greene & Wilson, 2012; Wiggins et al., 2015). Active acoustics, which typically is more energy intensive (Det Norske Veritas, 2010), involve the use of sonar devices that emit a sound pulse and can monitor bubbles moving up through the water column based on the returned sound wave or backscatter (Greinert & Nützel, 2004; Jackson et al., 1998; Ostrovsky et al., 2008). While hydroacoustic techniques have been successfully used in freshwater and ocean environments to understand bubble release and movement through the water column (e.g. Bergès et al., 2015; Dziak et al., 2008; Jackson et al., 1998; Ostrovsky et al., 2008; Wiggins et al., 2015), never has acoustic technology been used in tandem with meteorological and emissions data to investigate drivers of emission.

In this study, we describe the first use of a passive acoustic system for continuously monitoring CH₄ ebullition from two thaw ponds in a subarctic peatland during the growing season of 2018. This high-resolution acoustic data allows us to detect ebullitive emissions in addition to the collection of trapped gas in a floating trap system. We then analyze bubble detections for correlations with high-resolution meteorological data (air temperature, incoming solar radiation and wind speed) to investigate possible drivers of ebullitive emissions.

3.2 Methods

3.2.1 Field Site

The Stordalen Mire complex is located 10 km east of Abisko in northernmost Sweden (68°21'N, 19°02'E). Since 2000, this region has experienced mean annual temperatures above 0°C, leading to thawing and destabilization of permafrost below ground (Callaghan et al., 2010). Stordalen is home to several subhabitats typical of permafrost peatlands such as palsa plateaus, semi-wet and wet areas containing *Sphagnum spp.* and *Eriophorum spp.* respectively, as well as collapse features that contain meltwater (Johansson et al., 2006, Malmer et al., 2005), referred to in this paper as thaw ponds (Christensen, 2004). Previous work by Burke et al. (2019) at this site focused on measuring ebullitive CH₄ from eight thaw ponds across four growing seasons. They found daily ebullitive flux to be highly variable spatially and temporally, with the eight ponds falling into four statistically different groups (Burke et al., 2019). These groups were examined further and suggested that physical differences such as vegetation presence and hydrologic connectivity distinguished the four groups from each other (Burke et al., 2019). In this study, we focused on two particular ponds, Ponds C and H, that differed in pond type (Figure 3.1; type 2 and type 4 respectively, see Burke et al., 2019 for full description of both ponds).

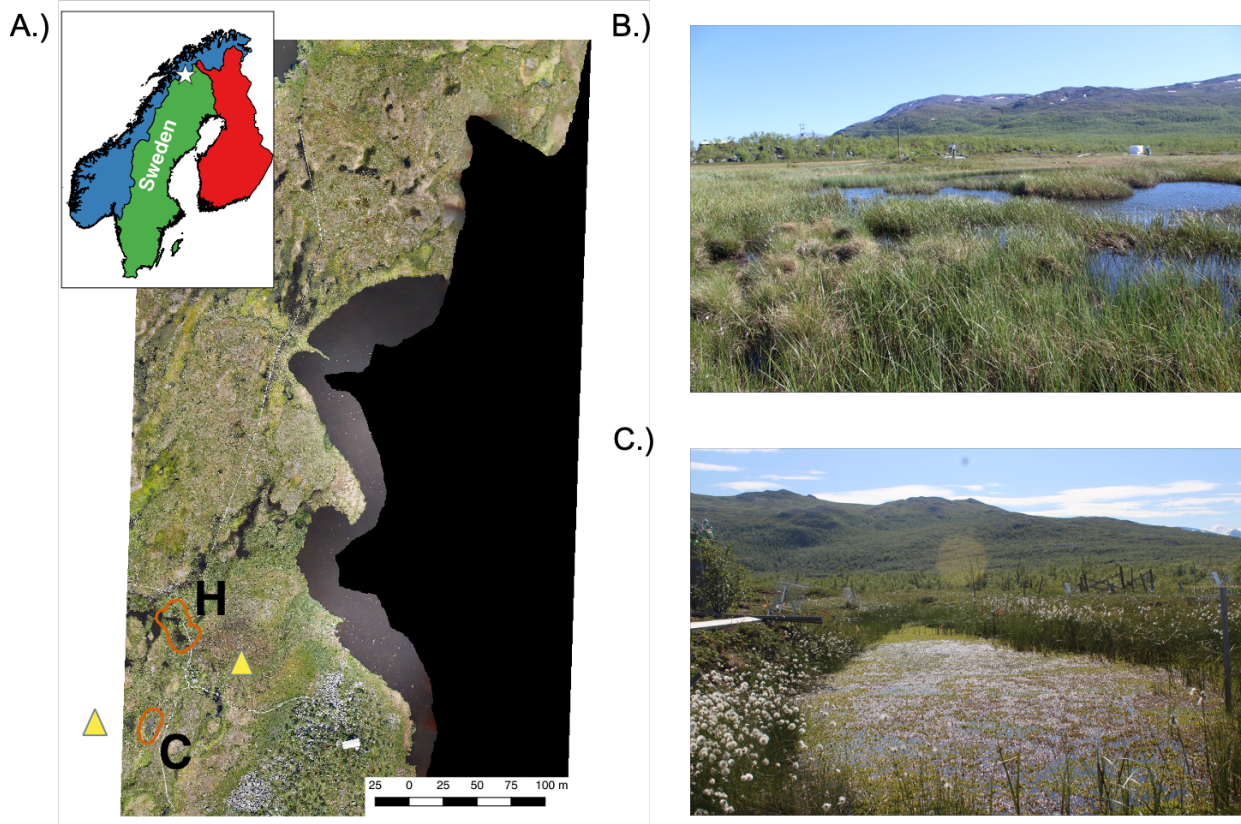


Figure 3.1 Modified from Burke et al. (2019) (Figure 1.1). A.) Aerial image of Stordalen Mire with ponds H and C outlined in orange. The aerial image was created by Michael Palace, Christina Herrick and Jessica DelGreco. The yellow triangles represent the location of the water table loggers. The aerial image does not cover the area to the west of pond C, so the water table logger location is approximate. B.) a ground level photograph of traps deployed in pond H during the 2019 field season. C.) a ground level photograph of the traps deployed in pond C during the 2019 field season. Ground level images were taken by Kathryn Bennett.

High frequency monitoring of meteorological variables of interest such as air temperature (T_{air} , °C), incoming solar radiation (SWR, $W\ m^{-2}$), total precipitation (TotPrec, mm), atmospheric pressure (P_{air} , kPA), relative humidity (Rh, %), wind speed (WS, ms^{-1}) were recorded at Stordalen Mire by the Swedish Integrated Carbon Observation System (ICOS) Network. They maintain an instrumentation shelter at Stordalen Mire, at the top of which (4 m above ground level) a WeatherHawk system (WeatherHawk, Logan, UT) records the meteorological variables mentioned above at 10 min intervals. Measurements of water table depth (WTD, mm) were also measured at

logger stations nearby both ponds (Persson et al., 2012) on 2-hr increments during the study. Total hydrostatic pressure at the bottom of each pond (P_{abs} , kPA) at 2-hr intervals across the study period was estimated for each pond using the following equation:

$$P_{abs} = (d \times \rho \times g) + P_{air}$$

where d is the pond depth (m), ρ is the density of liquid water (at 25°C: 997 kg m³), g is local gravity (9.82418 m s⁻²), and P_{air} (kPA) is the measured air pressure from the WeatherHawk system averaged over 2-hr increments.

3.2.2 Monitoring CH₄ ebullition

Ebullitive CH₄ was measured using simple floating funnel systems described in Burke et al. (2019). Each pond had two floating funnels deployed during the growing season, between 6 June and 8 August 2018 (Figure 3.2).

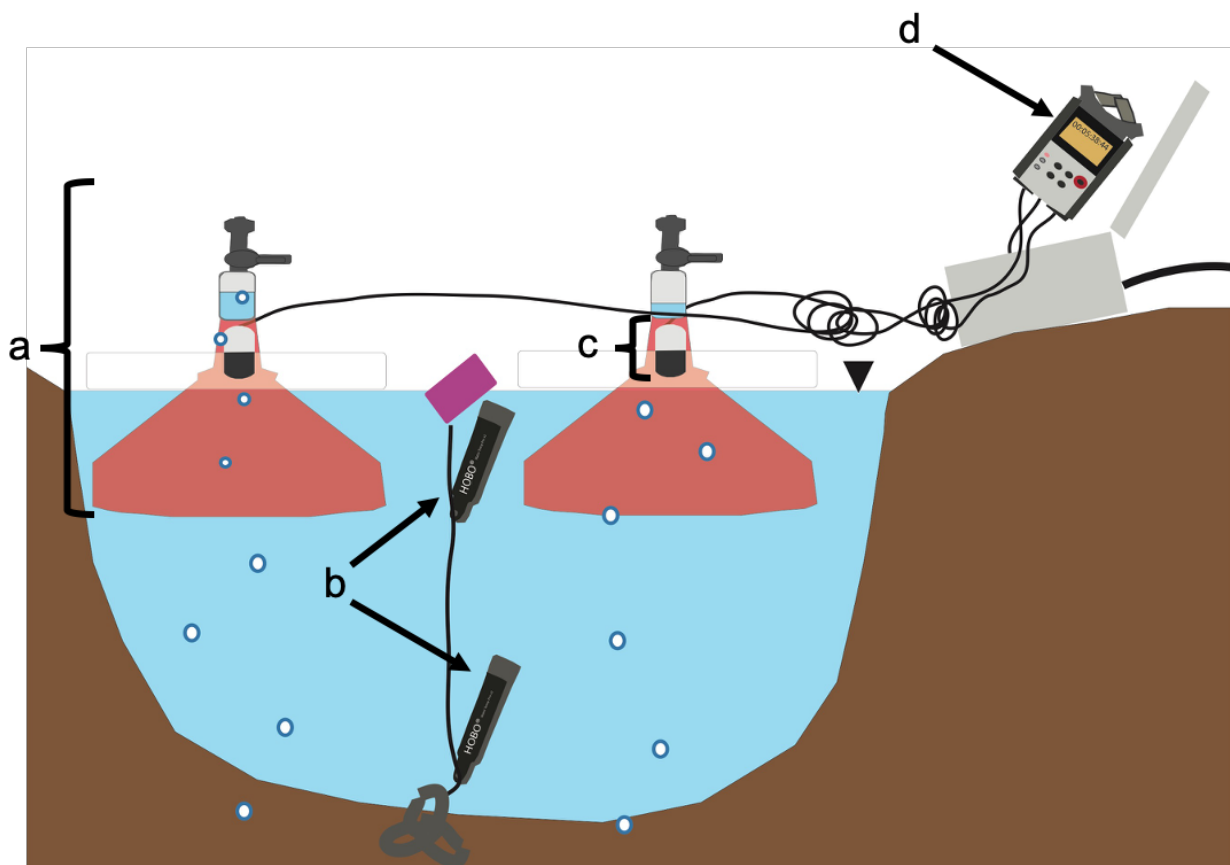


Figure 3.2 Diagram of acoustic bubble trap system deployed in pond C and pond H. a.) the floating bubble trap where ebullitive bubbles were captured and could be sampled regularly b.) water temperature loggers recorded water temperature every five minutes during the study period c.) the traps were equipped with a hydrophone at the base of each funnel which were plugged into d.) a recorder placed on shore.

The funnels were sampled for accumulated gas and measured for CH₄ concentration daily, with 100% of measurements collected within 1.5 days or less during the 2018 field season. A gas sample was collected only if there appeared to be > 1mL of gas accumulated in 60mL syringe at the top of each trap (Figure 3.2). Water temperature (T_{water}) was recorded throughout the field season, at 5-min intervals between June and September using data loggers placed in each pond (HOBO Water Temp Pro v2, model U22-001) (Burke et al., 2019). In order to enhance our temporal resolution of monitoring ebullition, each funnel was equipped with a hydrophone (waterproof microphone; Aquarian Hydrophones H1a Hydrophone, Aquarian Audio &

Scientific, Anacortes, WA), positioned at the base of the funnel's neck (Figure 3.2). This allowed for the bubbles entering the funnel to hit the hydrophone before moving up to the top of the syringe and displacing the water. The hydrophones were plugged into a recorder (ZOOM® H4n recorder, Zoom North America, Hauppauge, NY). Files were continuously recorded at 160 kb s^{-1} in stereo mode (each hydrophone was recorded on a separate channel) into .mp3 file format. Though recording in .mp3 format has its limitations in terms of audio quality due to signal compression, we chose to record in this format to allow us to record for longer time periods (.wav format files would have filled up our 32 GB SD cards within 42 hours, while .mp3 files allowed for us to record for nineteen days before switching out SD cards).

3.2.3 Laboratory Testing and Calibration

In order to investigate this acoustic method in a laboratory environment, we used a bubble generator (Rychert & Weber, 2020) that makes bubbles of known size using an air tank and a solenoid valve. Placed at the bottom of a freshwater 6m deep tank at the University of New Hampshire's Center for Coastal and Ocean Mapping Joint Hydrographic Center (CCOM; <http://ccom.unh.edu/facilities/test-tanks/engineering-tank>), the bubble generator released bubbles of four different sizes, fifty bubbles each released over a twenty-five-minute period. The bubble sizes were created by varying the differential pressure (DP) applied to the solenoid valve and were between 1 – 5mm radii in size at release (Rychert & Weber, 2020). The same floating bubble traps equipped with hydrophones used in the field were deployed above the bubble generator and recorded continuously as bubbles floated up into the funnel. The laboratory tests

were conducted in the evening hours of 3 September 2019 so as to minimize the background noise associated with the regular use of the facility. The audio files containing bubbles of known size were analyzed using the same code as the field data. Since the timing of each bubble release from the bubble generator was known, we could focus in on areas of the calibration data when the bubbles hit the hydrophone.

3.2.4 Acoustic Data Processing and Analysis

3.2.4.1 MATLAB processing

Typically, each .mp3 file written to the SD card was 2 GB in size, more than 29 hours long, and needed to be “chopped” into 6-minute segments before further analysis could occur (MP3/WAV Splitter, PistonSoft). Then each six-minute segment was read into MATLAB using the ‘audioread’ function. The signal was filtered by applying a bandpass filter (butter & filtfilt, Mathworks) using a pre-determined frequency range of 1500 – 4500Hz (Figure C.1). This frequency range is based on where most of the energy within the signal appeared to be concentrated (Figure C.1, panels A and B). The data was then transformed into an analytic signal using a Hilbert transform. A mean intensity of the acoustic signal of each channel (which corresponds to each trap) was then calculated, followed by a signal amplitude threshold, which takes the mean intensity of the signal and applies a signal to noise ratio to it, so as to bring the threshold up above the noise floor.

To find peaks associated with bubbles in the acoustic data, the findpeaksG.m function was used (O’Haver, 2020a). This function finds peaks by locating positive peaks above a given amplitude threshold. This function also fits a Gaussian curve the

top part of each detected peak to a Gaussian curve in order to estimate the width, height, and area under the curve (O'Haver, 2020b). To ensure the best detection parameters (smooth threshold, smooth width, fit width) were used in findpeaksG.m, the ipeak.m function was used in conjunction with the four calibration recordings where the location of bubble peaks within the files are known. The ipeak.m function allows for the interactive exploration of such functions like findpeaksG.m through data visualization and the tuning of detection parameters (O'Haver, 2020a, 2020b). A loop function was created to scroll through folders containing acoustic files that were created each time an SD card was swapped out of a trap. An output file was created for each folder containing a list of all the files processed, the peak number, its location within the file in seconds, the channel within which the peak was detected and the amplitude threshold of the channel. Channels within which no peaks were detected were still listed within the output file with a peak number of zero.

3.2.4.2 Data Filtering in R

Once processing in MATLAB was complete, further analysis occurred in R 3.6.1 (The R Foundation for Statistical Computing, 2019). Initial filtering was performed to remove all channels where no peaks were detected, leaving only positive detections ($n = 92,319$ detections). The timestamp of each peak detection found in the audio files was calculated based on the date and time the recorder was started, the length of each raw and chopped file, and the location of each peak detection within the file. Additionally, we explored how the number of detections would change if we aggregated detections occurring within a set number of seconds from the previous detection as a single

detection. Considering the sensitivity of the hydrophone (-190 dB, Aquarian Audio Products, 2020), we thought it possible that detections occurring close together in time could be from the same bubble passing up through the trap. We calculated the time difference between successive detections and then binned the detections into zero, half, one, two, three, up to ten second bins, with detections falling in each bin if the time difference between it and the previous detection was greater than the time bin in seconds. For example, detections that fell into the two seconds bin were detections that occurred more than two seconds apart. The zero seconds bin considered all detections valid detections. The greatest drops in total detections occurred between the zero and half second bins (Trap H1 – H2: 30% drop, Trap C1-C2: 17 – 11% drop respectively, Figure 3.3).

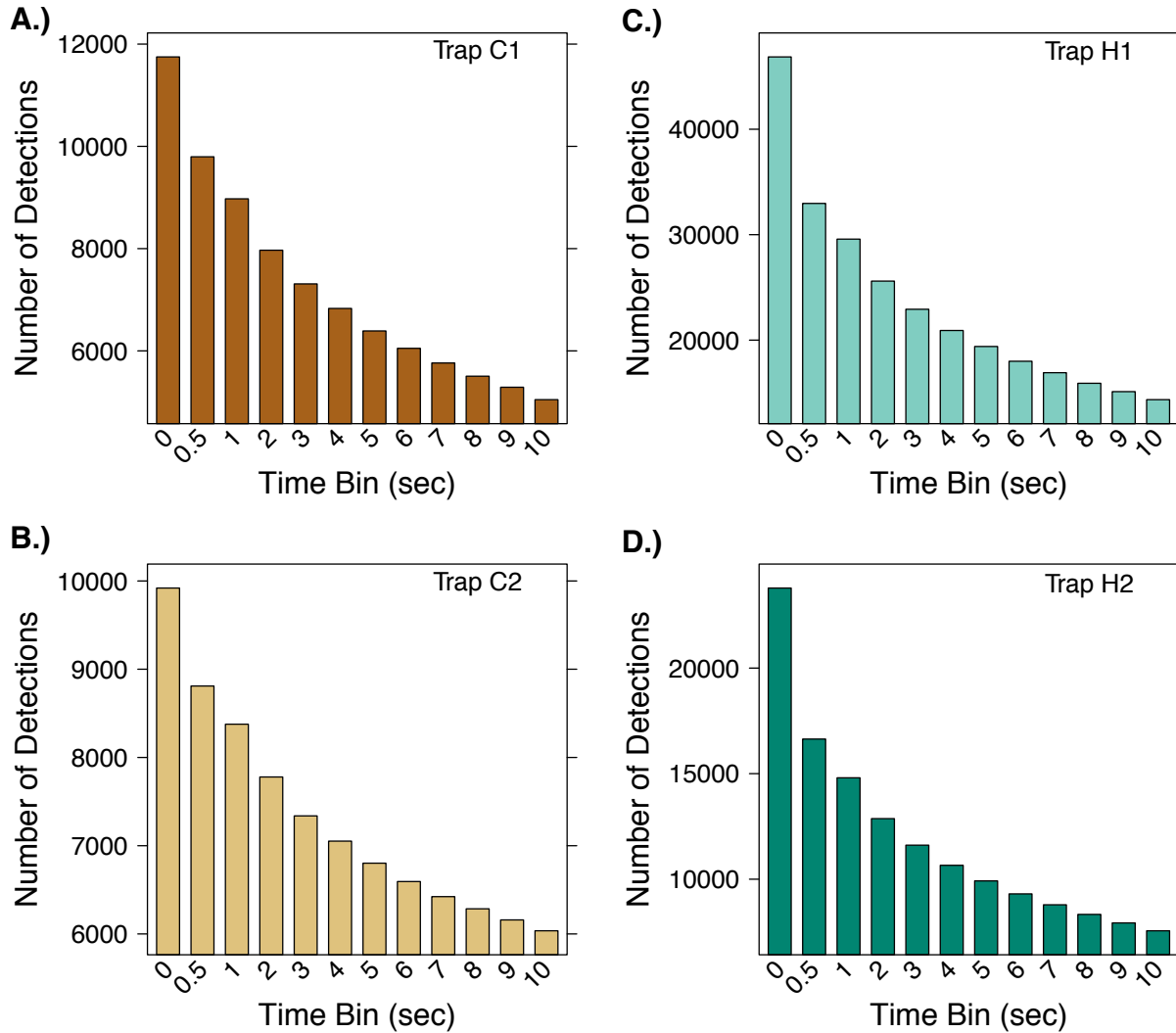


Figure 3.3 Number of detections across the different time bins (sec) of the detection dataset after initial filtering (zero detections removed). The zero bin represents when all detections are considered valid detections. Detections were considered in each bin if the difference in time between the detection and the one previous was greater than the time bin.

Due to the large drop in detections between the zero and half bins, detections that occurred less than half a second from each other were counted as a single detection ($n = 68,210$ detections remaining).

Further data filtering was performed to remove potential sources of background noise still left after preliminary filtering (e.g. trap sampling sounds and precipitation events). Any six-minute file with an amplitude threshold less than 1.2119×10^{-6} dB and

greater than 4.612×10^{-5} dB (the amplitude threshold of the smallest and largest bubble size from the laboratory test, respectfully) or occurred within an hour period where the weather station on site registered a rain event or a Rh reading of greater than 85% were automatically removed. The filtering conditions for TotPrec and Rh above 85% were applied due to the instances when the hydrophones detected rain events that were registered as well as not registered by the weather station (n = 12,342 detections remaining).

Table 3.1 Summary of acoustic detections from the 2018 sampling season that occurred more than half a second apart after filtering out noise due to sampling and precipitation events.

Trap	Total detections more than half a second apart
H1	7324
H2	3012
C1	428
C2	1578

Due to the disproportionate number of bubbles detected in pond H than in pond C (Table 3.1), we plotted ten-minute bubble counts across several days with differing patterns of WS to check to see if changes in WS were leading to false detections in the acoustic data of pond H. Ten-minute bubble counts were determined by summing the number of bubbles detected on a ten-minute basis across the acoustic record. On days when WS varied on the ten-minute scale, the number of detections counted in pond H appeared to mirror the changes in WS more so than in pond C suggesting the wind was either causing increased ebullition or false detections in the acoustic data from pond H (Figure C.2– Figure C.3). Pond H is positioned in an open area of Stordalen Mire, with a large flow-through fen on either side of it while pond C is more wind-protected, with an

intact palsa bank on one side (Figure 3.1, panels B and C). The hydrophones are floating just below the surface of the pond and there is a high probability that sounds related to increasing windspeed were registered as false detections in the acoustic data. Due to the apparent influence of noise from wind at pond H and with no apparent approach to filter out the impact of wind on the acoustic data, we chose to focus the remaining of our statistical testing on pond C.

3.2.5 Statistical Analysis

Statistical analysis was performed in R 3.6.1 (R Core Team, 2019). All bubble detection and meteorological data (T_{air} , P_{air} , SWR, WS, WTD, P_{abs} , and T_{water}) were averaged over a two-hour time window considering measurements of WTD had the lowest temporal resolution of measurements every two hours. Measurements of TotPrec and Rh were used to filter the detections, so they were not included in further statistical analysis. We performed initial data exploration, as detailed by Zuur et al. (2010), to determine if our data violated any of the assumptions of statistical analysis (e.g. collinearity, autocorrelation, normality and equal variance). This process revealed that the bubble count data were not normal due to the large number of zero counts in the data set and used the *fitdistrplus* package (Delignette-Muller & Dutang, 2015) to determine the data distribution. During initial data exploration, we also investigated whether any of the meteorological variables had a lagged effect on bubble detections by using the *astsa* package (Stoffer, 2019) yet the correlation coefficients for all of the meteorological variables (T_{air} , P_{air} , SWR, WS, WTD, P_{abs} , and T_{water}) were low (< 0.2) suggesting the lags found were inconsequential.

We then used generalized linear mixed effect modeling (GLMM) to determine the influence of trap, month, and the two-hourly means of several meteorological (or sums, in the case of precipitation) variables on the occurrence of bubbles in the acoustic record. Model selection was determined based on the model with the lowest Bayesian Information Criterion (BIC) because BIC tends to penalize complex models with multiple parameters more so than Akaike's Information Criterion (AIC) (Buckland et al., 1997). By modeling each variable separately first, we determined that month as well as several meteorological variables were not significant predictors of bubble detection (P_{air} , WTD, P_{abs} , T_{water}) and were therefore excluded from further modeling. We therefore developed five models to explore how bubble detections varied by trap and with changing WS, T_{air} and SWR:

$$(1) \text{BubDet}_{2hr} \sim \beta + k \times \text{trap}$$

$$(2) \text{BubDet}_{2hr} \sim \beta + k \times WS$$

$$(3) \text{BubDet}_{2hr} \sim \beta + k \times T_{air}$$

$$(4) \text{BubDet}_{2hr} \sim \beta + k \times SWR$$

$$(5) \text{BubDet}_{2hr} \sim \beta + k_1 \times T_{air} + k_2 \times SWR$$

where BubDet_{2hr} is the total number of bubble detections every two hours, β is the model intercept for equations 1-5 and k represents the slope of each parameter variable (e.g. trap, WS, T_{air} , SWR). In order to see how well model 5 represented the data, we created a linear model:

$$(6) \text{ BubDet}_{2hr} \sim \beta + k_1 \times \text{predBubDet}_{2hr}$$

where predBubDet_{2hr} are the bubble detections predicted by model 5, using the *predict.glmTMB* function via the *glmTMB* package (Brooks et al., 2017). Selection of singular and additive random effects was performed for each model including the influence of day of year (doy), month and trap (note: for model 1, trap was not included as a random effect), with the model with the lowest BIC chosen as the best fit. Models 1-5 were fitted with a negative binomial distribution via the *glmTMB* package (Brooks et al., 2017). For model 5, backwards selection of fixed effects was performed following the protocol set out by Zuur et al. (2010). Although WS was found to be a significant predictor of bubble detections on its own (model 2) and was included initially in model 5, through the backwards selection process just described it was removed from the final model. Since mixed-effects models do not produce a whole-model r^2 value, a pseudo- r^2 value was calculated for each GLMM model (Nakagawa & Schielzeth, 2013) using the *MuMIn* package, which provided a marginal pseudo r^2 ($R^2_{\text{GLMM}(m)}$) describing the variance explained by the model's fixed effects as well as a conditional pseudo r^2 ($R^2_{\text{GLMM}(c)}$) describing the variance explained by the model's fixed and random effects (Bartón, 2019). Since model 6 was a linear model, an adjusted model r^2 is provided in the model output.

3.3 Results

3.3.1 Meteorological drivers of CH_4 emissions

All meteorological variables measured during the study period varied on a daily basis (Figure 3.4). Daily average WS, daily TotPrec and Rh peaked during the month of June while daily T_{air} and T_{pond} were low (Table 3.2). As the study period progressed, air and pond temperatures increased with T_{air} peaking in July and T_{pond} peaking in August. The lowest TotPrec was measured in August however it is important to note that this study only extended eight days into August (Table 3.2).

Table 3.2 Summary of measured meteorological data during the study period: 6 June – 8 August 2018. Pair, SWR, T_{air} , TotPrec, Rh and WS were measured by ICOS-Sweden, WTD was measured by Dr. Andreas Persson et al., T_{pond} was measured by the co-authors. The N value below each month corresponds to the number of days within that month that the averages are pulled from.

Data	N =	June 24	July 31	August 8
Pair (kPa)		96.6	97.5	96.9
Pabs (kPa)		6242.1	6209.6	6504.2
WTD (mm)		277.3	274	304.2
SWR ($W m^{-2}$)		155.1	219.5	170.8
T_{air} ($^{\circ}C$)		7.1	14.9	14
T_{pond} ($^{\circ}C$)		7.2	12.5	13.9
TotPrec (mm)		74.8	51	6.2
Rh (%)		77.5	72.6	76.4
WS ($m s^{-1}$)		5.7	4.2	4.9

To explore drivers of bubble emission, we modeled each meteorological variable individually against $BubDet_{2hr}$ first, with WS, T_{air} and SWR returning significant fixed effect p values ($p < 0.005$, Table C.1). All three variables had positive slopes which suggest bubble detections increased with increasing WS, T_{air} and SWR. The pseudo r^2 values suggest however that for all three singular models (models 2 - 4), little of the variability in bubble detections is explained by the fixed effects alone ($R^2_{GLMM(m)}$ 0.01 – 0.1). Therefore, it is likely that more of the variability is explained by the random effects of the model (trap and doy, $R^2_{GLMM(c)}$: 0.84 – 0.87, Table C.1). Based on the significance

of WS, T_{air} and SWR in their individual models, we created an additive model to look at the influence of multiple meteorological variables on bubble detections (model 5). Through the backwards selection process, WS was removed from the final model, leaving only T_{air} and SWR (model 5). Both T_{air} and SWR had significantly positive slopes ($k_1 \times T_{\text{air}} = 0.07$, $p = 0.0004$, $k_2 \times \text{SWR} = 0.001$, $p < 0.0001$) with T_{air} potentially playing a more important role in driving bubble detections than SWR given the larger slope (Figure 3.5 panels A & B; Table C.1). However, similarly to the singular models, the R^2_{GLMM} for model 5 suggests much more of the variability in bubble detections is driven by the random effects in the model (trap & doy, Table C.1). Further, we used model 5 to predict bubble detections across the sampling period (model 6) and saw again an adjusted r^2 that is indicative of the fixed effects having a lack of effect on measured bubble detections (Figure 3.5 panel C; Table C.2).

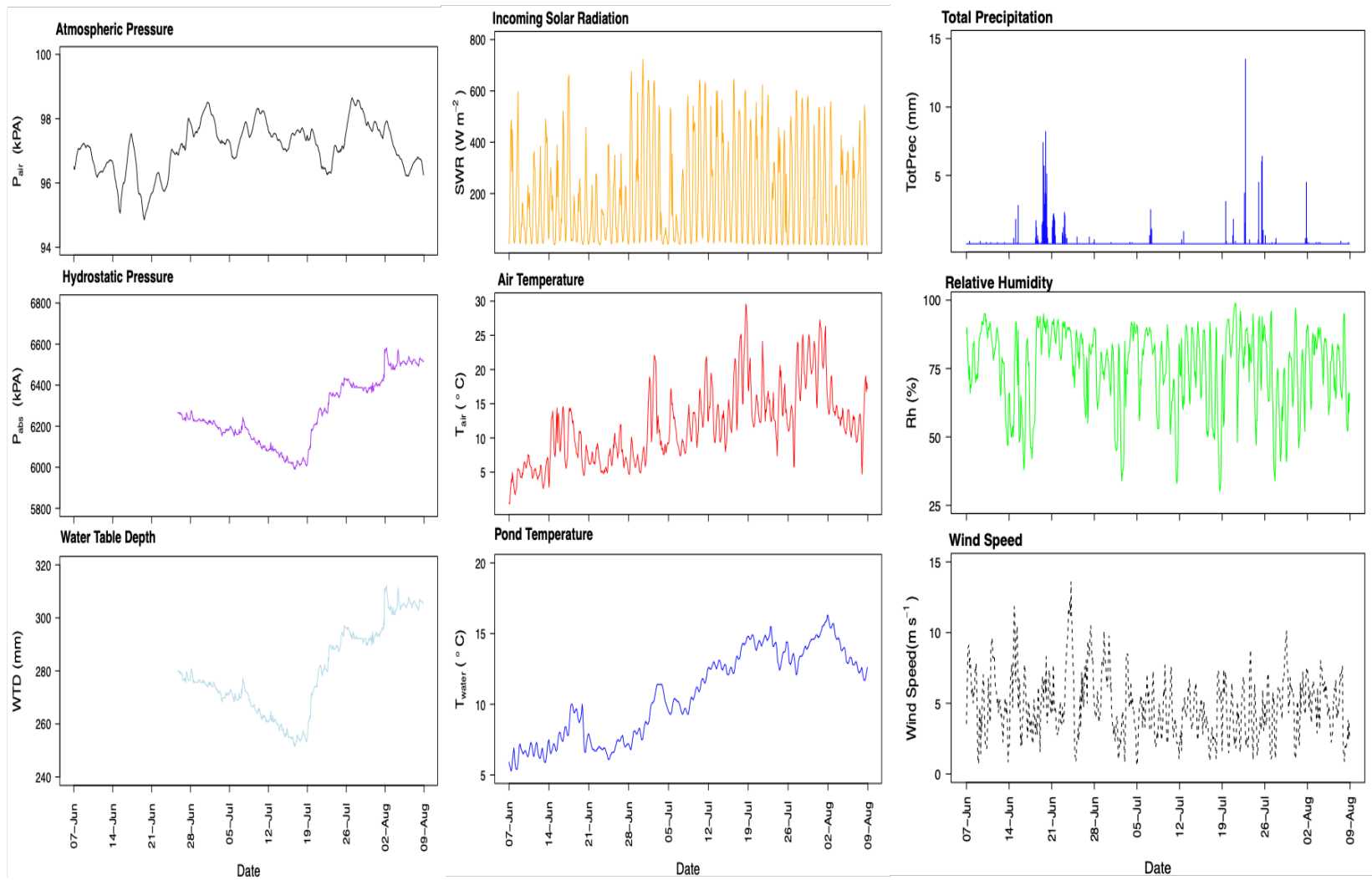


Figure 3.4 Time series of two-hour averages (apart from total precipitation, which is two-hour totals) of all meteorological variables measured during the sampling season. Each y axis is labeled with their respective measurement units.

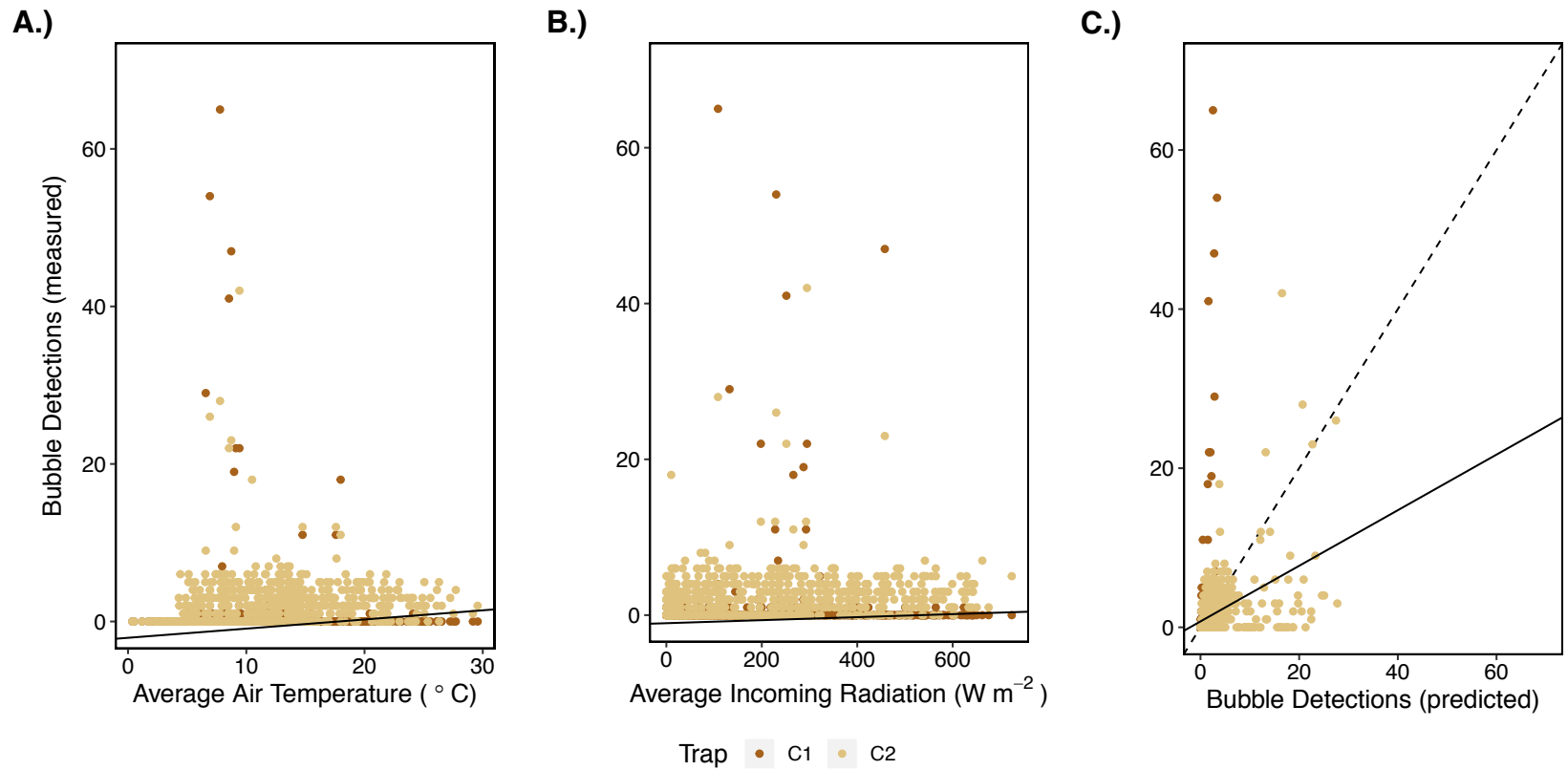


Figure 3.5 Scatterplots showing the relationship between bubble detections and A.) T_{air} , B.) SWR, and C.) predicted bubble detections based on the additive model that included both T_{air} and SWR (model 5). Detections from each trap are distinguished by color. The solid black lines in each subplot represent the model fit line for model 3, model 4 and model 6 respectively. The dashed line in panel C.) is a 1:1 line for reference.

3.3.2 Spatial and Temporal variability in bubble detection by trap

Daily total bubble detections captured in both traps in pond C varied across the study period (Figure 3.6). The lowest number of bubbles we detected on a daily basis from both traps was 0, with 0 detections also being the mode for trap C1 (Figure 3.6).

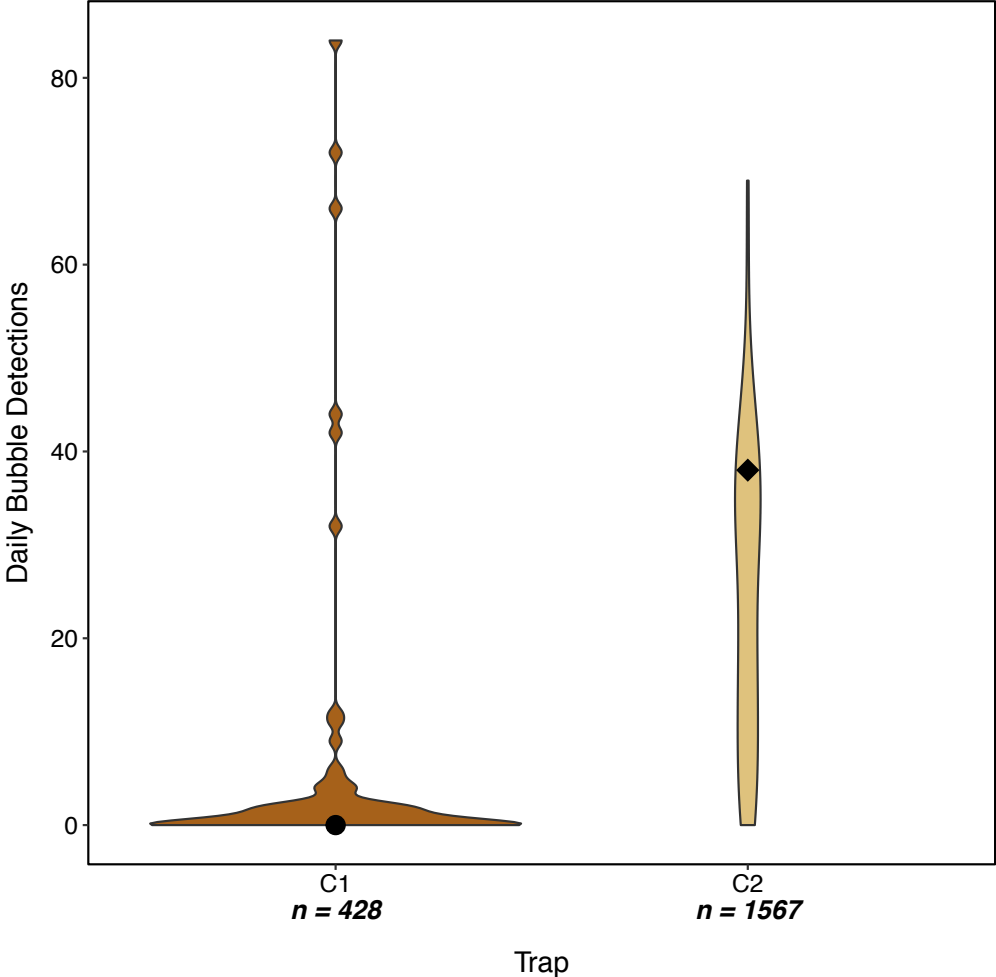


Figure 3.6 Violin plot showing the distribution of bubble detections measured on a daily basis between traps C1 and C2 during the 2018 growing season. The black circle and diamond on the violin plots represent the mode of daily bubble detections for traps C1 and C2 respectively. N values below each trap represent the total number of detections measured across the sampling season.

The mode for trap C2 was 38 detections (Figure 3.6). The maximum number of detections in a day from trap C1 was 84 and was 69 in trap C2 (Table 3.2). This peak in

daily detections occurred in June for trap C1 and July for trap C2 (Table 3.2). Similarly, the cumulative bubble detections per month for trap C1 occurred in June at 284 detections, while for trap C2, with 801 detections, this occurred in July (Table 3.2).

Table 3.3 Summary of the minimum, maximum, mode and cumulative of bubble detections on a daily scale for each month in the 2018 sampling season. The numbers with the * for each trap represent the maximum daily bubble detections across the whole sampling season.

	C1			C2		
	June	July	August	June	July	August
Total Daily Bubble Detections						
Minimum	0	0	0	0	0	5
Maximum	84*	44	12	60	69*	44
Mode	0	0	0	0	29	5
Cumulative Bubble Detections	284	107	37	555	801	211

Both traps had the lowest number of bubble detections on a daily and a cumulative basis in August (12 and 37 for trap C1, 44 and 211 for trap C2 respectively; Table 3.2), however the study only extended eight days into the month of August. Overall, we measured 428 bubble detections in trap C1 and 1567 bubble detections in trap C2 (Figure C.4).

Though we counted more bubble detections in trap C2 than in C1, we sampled more accumulated gas from trap C1. We collected 72.4 mL of ebullitive gas from trap C1 and 37.6 mL of ebullitive gas from trap C2, with a daily average volume collected per trap of 1.14 mL and 0.6 mL respectively (Figure 3.7 & Figure C.4). Bubble detections were found to vary significantly by trap (fixed effect p value < 0.0001, model 1; Table C.1), however the marginal pseudo r^2 value of 0.36 suggests that trap explains only 36% of the variability in $\text{BubDet}_{2\text{hr}}$ while the conditional pseudo r^2 (which includes both the fixed

and random effects) of 0.83 suggests more of the variability is explained by the random effect of day.

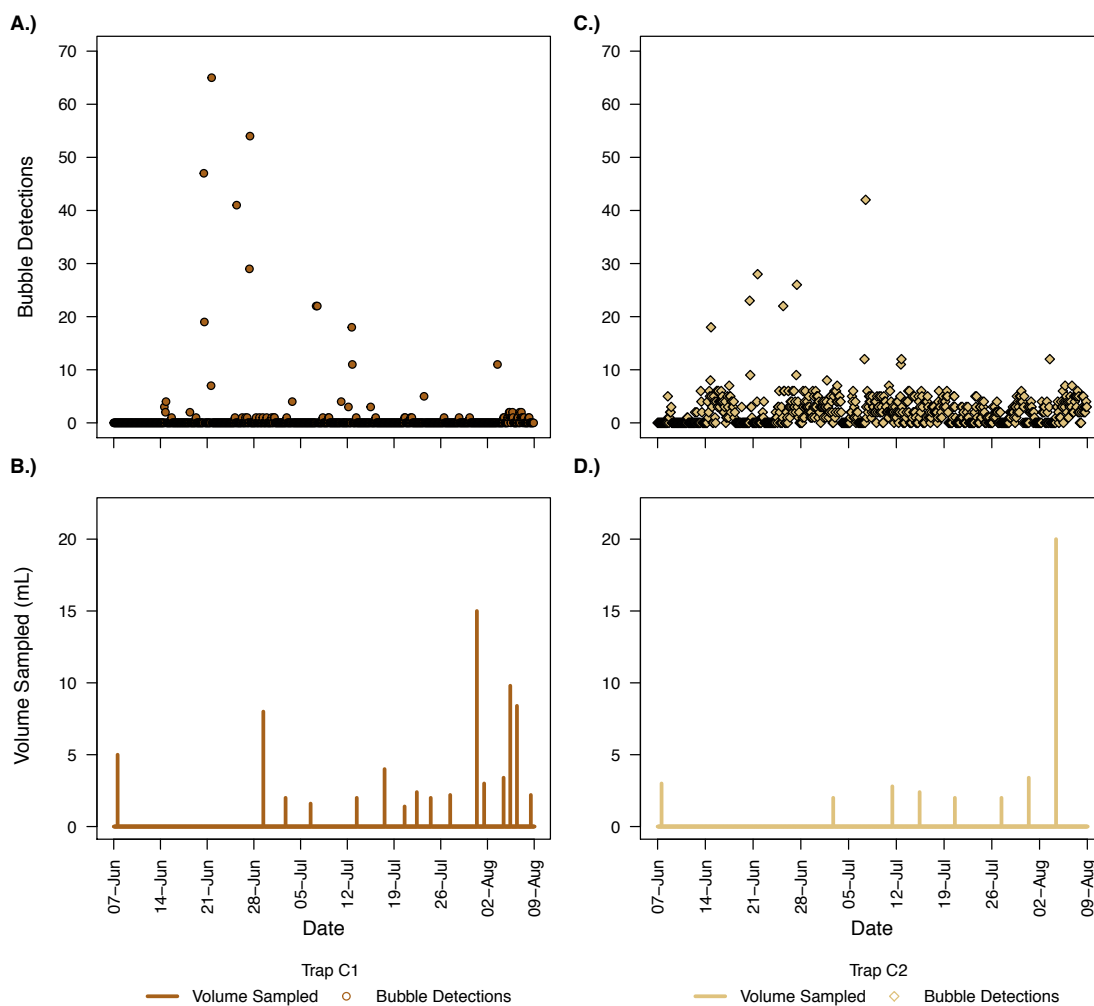


Figure 3.7 Time series of total bubble detections every two hours and the volume of gas collected in mL across the 2018 sampling season from trap C1 (A.) & B.) respectively) and from trap C2 (C.) & D.) respectively).

On a diel basis, average bubble detections varied per hour between traps, yet both traps appear to peak between the hours of 08:00 and 18:00 local time (Figure 3.8: A – B). The average hourly bubble detections in the early hours of the morning and late evening is low for both traps. Average hourly T_{air} , SWR and WS followed a similar pattern, all peaking between 12:00 and 16:00 local time, and all reducing to their lowest

hourly average in the late evening and early morning hours (Figure 3.8: C – E). Further it appears the highest average hourly bubble detections occurred during the time of day when T_{air} , SWR and WS tended to be highest, between 10:00 and 13:00, while the lowest hourly detections on average occurred between 22:00 and 01:00 (Figure 3.8).

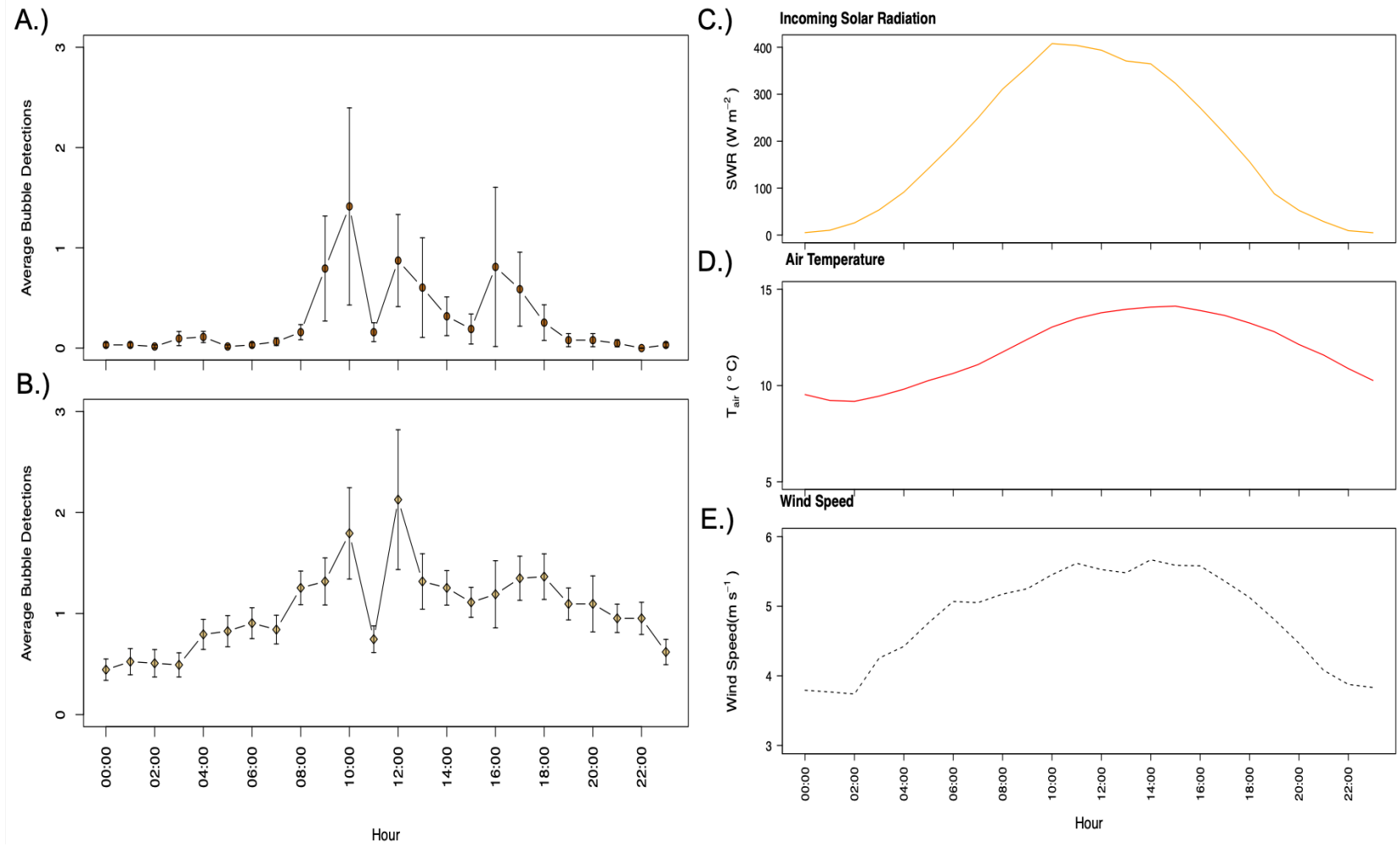


Figure 3.8 Diel variability in average bubble detections and SWR, T_{air}, and WS on an hourly basis across the study period for traps C1 and C2 (Traps C1 & C2: panels A & B respectively, SWR, T_{air}, WS: panels C-E respectively). Different traps are distinguished by the color and shape of the points. Vertical bars represent ± the standard error associated with each point.

3.4 Discussion

3.4.1 Drivers of CH₄ ebullition

Previous research has established important drivers of ebullitive emission such as changes in atmospheric pressure (Tokida et al. 2007; Tokida et al., 2009; Wik et al., 2013), changes in water table depth (Weyhenmeyer, 1999), and energy inputs (e.g. T_{air} & SWR, Goodrich et al., 2011; Wik et al., 2014). Our results support the importance of energy inputs (Goodrich et al, 2011; Wik et al., 2014) however contrary to previous work, we did not find P_{air}, P_{abs} or WTD to be significant drivers (Tokida et al. 2007; Tokida et al., 2009; Weyhenmeyer, 1999; Wik et al., 2013). We found bubble detections to be significantly correlated with T_{air} and SWR (model 5) with bubble detections increasing with increasing T_{air} and SWR. In trap C2, the maximum number of detections was measured in July, which follows the peak in daily average T_{air} for the season. In the larger lakes in Stordalen Mire, energy input, in the form of SWR and sediment temperature, were found to be very strong predictors of seasonal cumulative ebullitive flux (Wik et al., 2014). On a diel scale, Bastviken et al. (2004) saw a 70% increase in ebullitive emission from lakes in North American and Sweden during day compared to night which agrees with our finding of average hourly bubble detections peaking in the middle of the day and reaching their lowest levels at night (Figure 3.8). This is in contrast to ebullitive emission rates from automatic chamber data from a temperate peatland which peaked in the early morning and late evening. However, in the peatland the ebullitive signal is also likely impacted by the plants and microbial communities near the surface (Goodrich et al., 2011). All of the GLMM models (1-5) looking at

meteorological drivers of bubble detections in this study included spatial (trap) and temporal (day) variability as random effects and each suggested much of the variability seen in bubble detections seen within a sub-meter area were due to spatial and temporal heterogeneity represented by these random effects (Table C.1). However, the importance of meteorological drivers, particularly on the diel scale, could be further investigated by including time of day as a fixed effect in further models. This agrees with previous research that found ebullitive emissions from lakes and ponds to be highly spatially and temporally variable (Burke et al., 2019; Kuhn et al., 2018; Wik et al. 2013; Wik et al. 2014). Additionally, substrate quality (e.g. how labile the C is below ground) has been shown to affect rates of CH₄ production and ebullition as well (Bergman et al., 1998; Malhotra & Roulet, 2015; Wik et al. 2018). We saw lower number of detections from trap C1 than in C2 which could suggest more steady releases below trap C2 and more episodic releases below trap C1 (Figure 3.6) indicating some subsurface differences in organic matter quality and pore structure between these traps (Coulthard et al., 2009). Since we collected more gas from trap C1 overall, these episodic events potentially give off larger bubbles or more volume than the steady ebullition from trap C2 (Figure 3.7). Coulthard et al. (2009) suggests more ebullitive CH₄ could be released to the atmosphere via episodic events than steady rates of emission due to the bypassing or overwhelming of the CH₄ oxidation (consumption) zone.

Several studies have also found increasing wind speed leads to more ebullitive emissions in peatlands (Friborg et al., 1997; Goodrich et al., 2011; Sachs et al., 2008; Tokida et al., 2009). In a polygonal tundra area in northern Siberia, Sachs et al. (2008)

found near-surface turbulence to account for 60% of the variability in emissions while in a temperate peatland, Goodrich et al. (2011) found windspeed (a proxy for turbulence) to account for 63% of variability in emissions. We counted the most daily bubble detections in June for trap C1, at 84 detections, on June 27, 2018 (Figure C.3). Further investigations into the meteorological variability on this day reveals that the daily average wind speed was 8.6 m s^{-1} , almost 3 m s^{-1} higher than the daily average windspeed for the month of June (5.7 m s^{-1} , Table 3.3). There was also a high number of detections that day in trap C2, though not the highest during the season, of 60 detections which suggests the increase in windspeed is acting on different areas of the pond in a similar way. Further, we found that when WS was modeled against bubble detections across the sampling season, WS was deemed a significant fixed effect (Table C.1).

3.4.2 High resolution monitoring of CH₄ ebullition

High-resolution sampling of CH₄ ebullition in lakes often involves the use of pressure sensors (Duc et al., 2019; Maher et al., 2019; Varadharajan et al., 2010; Varadharajan & Hemond, 2012) with fewer studies using acoustic techniques (Ostrovksy, 2003; Ostrovsky et al., 2008; Vagle et al., 2010). We continuously recorded bubble emissions using a high-resolution passive acoustic system across the growing season and found CH₄ emissions to vary significantly between bubble traps (Figure 3.7; Table C.1). High-resolution sampling is useful for ebullitive monitoring as ebullitive emissions are highly temporally variable. Teasing out meteorological drivers can also be difficult with daily resolution sampling data. Burke et al., (2019) saw very weak correlation between daily

average ebullitive flux and meteorological variables (SWR and T_{water}) and suggested this could be due to the sampling frequency. Similarly, we found meteorological variables (SWR, T_{air} and WS) to be significantly correlated with bubble detections yet they explained little of the variability seen. Yet, when we look on a diel scale, it appears as though bubble detections do correlate with changes in SWR, T_{air} and WS (Figure 3.8). Several studies have also noted diurnal variability in CH_4 emissions (Bastviken et al., 2004; Goodrich et al., 2011, Maher et al., 2019) when sub-daily sampling frequency was used.

Contrary to many passive acoustic systems that place the listening device some distance from the emission source (e.g. Dziak et al., 2018; Greene & Wilson, 2012; Wiggins et al., 2015), our acoustically equipped bubble traps allows for the close proximity and even contact between bubble and hydrophone as the CH_4 bubble passes up through the funnel (Figure 3.2). Given the shallow depth of our ponds (≤ 41 cm; Burke et al., 2019) we were limited by how deep we could place the bubble trap system while also avoiding contact with the pond bottom. With this limitation, we exposed the sensitive hydrophones to background noise relating to sampling and meteorological variables (e.g. rain events, wind), which has potentially led to some false detections. We found the acoustic records from traps in pond H were affected by wind noise, given the large difference in number of bubble detections found compared to pond C (Table 3.1) and the mirroring of increasing and decreasing bubble detections during windy days (Figure C.2 & Figure C.3). While ebullitive emissions have been shown to increase with increasing wind speed, we cannot confidently separate true ebullitive emissions relating

to wind speed changes and false detections due to wind noise within pond H. Varadharajan et al. (2010) also recorded wind/wave noise in their pressure data when the wind was > 3 kmph though this was typically only an issue when the trap was empty. Their bubble systems however were deployed in a much larger lake (0.58 km²; Varadharajan & Hemond, 2012) than our ponds. Given the shallow depth of the ponds, we were unable to deploy the traps deeper in the water column as was done by Varadharajan & Hemond (2012).

In the future, caution should be taken when placing these systems in shallow ponds so as to avoid potential background noise. For example, sound insulating material could be wrapped around the funnel base where the hydrophone is positioned and along the sides. This could help not only insulate the hydrophone from wind noise, but also from noise associated with trap sampling or with people walking by the traps. In addition, if the trap is placed in a pond that has moving water, the trap should be placed downstream of any boardwalk or rocks to avoid noise associated with the trap making contact with said boardwalk or rocks.

3.5 Conclusions

This study presents the use of an acoustic bubble trap system to obtain high resolution data of CH₄ emissions from subarctic peatland ponds. We found bubble detections to correlate with meteorological variables (SWR, T_{air} and WS) yet more of the variability was explained by apparent spatial and temporal heterogeneity within a pond. We also saw diel variability in hourly bubble detections in tandem with hourly averages

of T_{air} , SWR and WS. The acoustic data from one pond site, located in an open area appeared to be more affected by wind noise than the other more sheltered pond, which makes separating false and true detections difficult. Therefore, steps should be taken to insulate the acoustic traps from background noise when deploying them in shallow ponds as well as avoiding any solid object in the ponds that the traps could be pushed into by the wind. Our results show that hydroacoustic monitoring techniques in tandem with manual sampling of CH_4 emissions aid in our understanding of the drivers of ebullitive emission in subarctic peatlands.

LIST OF REFERENCES

- Abisko Scientific Research Station ANS. (2017). *Abisko Weather Station Data*. (A. S. R. Station, Ed.). Abisko Scientific Research Station. Retrieved from <http://polar.se/abisko>
- Anderson, K., & Gaston, K. (2013). Lightweight unmanned aerial vehicles will revolutionize spatial ecology. *Frontiers in Ecology and the Environment*, 11(3), 138–146. <https://doi.org/10.1890/120150>
- Andersson, J. (2016, February 1). *Assessing the ecosystem carbon storage in two subarctic areas: Phytomass and soil organic carbon stocks at Abisko in Sweden and Utsjoki in Finland* (Masters). Stockholm University, Stockholm. Retrieved from <http://www.diva-portal.org/smash/record.jsf?pid=diva2%3A932184&dswid=-7530>
- Andresen, C. G., & Lougheed, V. L. (2015). Disappearing Arctic tundra ponds: Fine-scale analysis of surface hydrology in drained thaw lake basins over a 65 year period (1948-2013). *Journal of Geophysical Research: Biogeosciences*, 120(3), 466–479. <https://doi.org/10.1002/2014JG002778>
- Aquarian Audio Products. (2020). H1a Hydrophone User's Guide. Retrieved from https://www.aquarianaudio.com/AqAudDocs/H1a_manual.pdf
- Arthur, D., & Vassilvitskii, S. (2007). k-means++: The advantages of careful seeding (pp. 1027–1035). Society for Industrial and Applied Mathematics.
- Avis, C. A., Weaver, A. J., & Meissner, K. J. (2011). Reduction in areal extent of high-latitude wetlands in response to permafrost thaw. *Nature Geoscience*, 4(7), 444–448.
- Bäckstrand, K. (2010). Annual carbon gas budget for subarctic peatland, Northern Sweden. *Biogeosciences*, 7, 95–108.
- Bartón, K. (2019). MuMIn: Multi-Model Inference (Version R package version 1.43.15). Retrieved from <https://CRAN.R-project.org/package=MuMIn>
- Bastviken, D., Cole, J., Pace, M., & Tranvik, L. (2004). Methane emissions from lakes: Dependence of lake characteristics, two regional assessments, and a global estimate. *Global Biogeochemical Cycles*, 18(4), n/a–n/a. <https://doi.org/10.1029/2004GB002238>
- Bastviken, D., Tranvik, L. J., & Downing, J. A. (2011). Freshwater Methane Emissions Offset the Continental Carbon Sink. *Science*, (Table 1), 6.

- Bell, R. G. (1969). Studies on the decomposition of organic matter in flooded soil. *Soil Biology and Biochemistry*, 1(2), 105–116. [https://doi.org/10.1016/0038-0717\(69\)90001-7](https://doi.org/10.1016/0038-0717(69)90001-7)
- Bergès, B. J. P., Leighton, T. G., & White, P. R. (2015). Passive acoustic quantification of gas fluxes during controlled gas release experiments. *International Journal of Greenhouse Gas Control*, 38, 64–79. <https://doi.org/10.1016/j.ijggc.2015.02.008>
- Bergman, I., Svensson, B. H., & Nilsson, M. (1998). Regulation of methane production in a swedish acid mire by pH, temperature and substrate. *Soil Biology and Biochemistry*, 30(6), 729–741. [https://doi.org/10.1016/S0038-0717\(97\)00181-8](https://doi.org/10.1016/S0038-0717(97)00181-8)
- Bolduc, B., Hodgkins, S. B., Sullivan, M., The IsoGenie Team, & Rich, V. I. (in prep). The IsoGenieDB: A Solution to Systems Microbiology Integrating Cross-Disciplinary Data Management. Retrieved from <https://isogenie.osu.edu/data/>
- Bouchard, F., Francus, P., Pienitz, R., Laurion, I., & Feyte, S. (2014). Subarctic thermokarst ponds: investigating recent landscape evolution and sediment dynamics in thawed permafrost of northern Québec (Canada). *Arctic, Antarctic, and Alpine Research*, 46(1), 251–271.
- van Breemen, N. (1995). How Sphagnum bogs down other plants. *Trends in Ecology & Evolution*, 10(7), 270–275. [http://dx.doi.org/10.1016/0169-5347\(95\)90007-1](http://dx.doi.org/10.1016/0169-5347(95)90007-1)
- Brooks, M. E., Kristensen, K., van Benthem, K. J., Magnusson, A., Berg, C. W., Nielsen, A., et al. (2017). glmmTMB Balances Speed and Flexibility Among Packages for Zero-inflated Generalized Linear Mixed Modeling. *The R Journal*, 9(2), 378–400.
- Brown, L., & Young, K. L. (2009). Assessment of Three Mapping Techniques to Delineate Lakes and Ponds in a Canadian High Arctic Wetland Complex. *ARCTIC*, 59(3), 283–293. <https://doi.org/10.14430/arctic314>
- Buckland, S. T., Burnham, K. P., & Augustin, N. H. (1997). Model selection: an integral part of inference. *Biometrics*, 603–618.
- Burke, S. A., Wik, M., Lang, A., Contosta, A. R., Palace, M., Crill, P. M., & Varner, R. K. (2019). Long-Term Measurements of Methane Ebullition From Thaw Ponds. *Journal of Geophysical Research: Biogeosciences*, 2018JG004786. <https://doi.org/10.1029/2018JG004786>
- Callaghan, T. V., Bergholm, F., Christensen, T. R., Jonasson, C., Kokfelt, U., & Johansson, M. (2010). A new climate era in the sub-Arctic: Accelerating climate changes and multiple impacts. *Geophysical Research Letters*, 37(14). <https://doi.org/10.1029/2009GL042064>

- Camill, P. (1999). Patterns of boreal permafrost peatland vegetation across environmental gradients sensitive to climate warming, *77*, 13.
- Cermakova, I., Komarkova, J., & Sedlak, P. (2019). Calculation of Visible Spectral Indices from UAV-Based Data: Small Water Bodies Monitoring. In *2019 14th Iberian Conference on Information Systems and Technologies (CISTI)* (pp. 1–5). Coimbra, Portugal: IEEE. <https://doi.org/10.23919/CISTI.2019.8760609>
- Chambers, J. Q., Asner, G. P., Morton, D. C., Anderson, L. O., Saatchi, S. S., Espirito-Santo, F. D. B., et al. (2007). Regional ecosystem structure and function: ecological insights from remote sensing of tropical forests. *Trends in Ecology & Evolution*, *22*(8), 414–423.
- Chanton, J. P. (2005). The effect of gas transport on the isotope signature of methane in wetlands. *Organic Geochemistry*, *36*(5), 753–768. <https://doi.org/10.1016/j.orggeochem.2004.10.007>
- Chanton, J. P., Glaser, P. H., Chasar, L. S., Burdige, D. J., Hines, M. E., Siegel, D. I., et al. (2008). Radiocarbon evidence for the importance of surface vegetation on fermentation and methanogenesis in contrasting types of boreal peatlands. *Global Biogeochemical Cycles*, *22*(4), n/a-n/a. <https://doi.org/10.1029/2008GB003274>
- Chasar, L. S., Chanton, J. P., Glaser, P. H., Siegel, D. I., & Rivers, J. S. (2000). Radiocarbon and stable carbon isotopic evidence for transport and transformation of dissolved organic carbon, dissolved inorganic carbon, and CH₄ in a northern Minnesota peatland. *Global Biogeochemical Cycles*, *14*(4), 1095–1108.
- Christensen, T. R., Johansson, T., Akerman, H. J., Mastepanov, M., Malmer, N., Friborg, T., et al. (2004). Thawing sub-arctic permafrost: Effects on vegetation and methane emissions. *Geophysical Vdots*, *31*(4), L04501. <https://doi.org/10.1029/2003GL018680>
- Ciais, P., Sabine, C., Bala, G., Bopp, L., Brovkin, V., Canadell, J., et al. (2013). *Carbon and Other Biogeochemical Cycles* (Climate Change 2013: The Physical Science Basis. Contribution of Working Group I to the Fifth Assessment Report of the Intergovernmental Panel on Climate Change) (pp. 465–570). Cambridge, United Kingdom and New York, New York, USA: Intergovernmental Panel on Climate Change. <https://doi.org/10.1017/CBO9781107415324.015>
- Cohen, W. B., & Goward, S. N. (2004). Landsat's role in ecological applications of remote sensing. *AIBS Bulletin*, *54*(6), 535–7645.
- Coulthard, T. J., Baird, A. J., Ramirez, J., & Waddington, J. M. (2009). Methane dynamics in peat: Importance of shallow peats and a novel reduced-complexity approach for modeling ebullition. In *Carbon Cycling in Northern Peatlands* (pp.

- 173–186). Retrieved from <http://onlinelibrary.wiley.com/doi/10.1029/2008GM000811/summary>
- Davidson, S., Santos, M., Sloan, V., Reuss-Schmidt, K., Phoenix, G., Oechel, W., & Zona, D. (2017). Upscaling CH₄ Fluxes Using High-Resolution Imagery in Arctic Tundra Ecosystems. *Remote Sensing*, 9(12), 1227. <https://doi.org/10.3390/rs9121227>
- DelGreco, J. (2018). *Four years of unmanned aerial system imagery reveals vegetation change in a sub-arctic mire due to permafrost thaw* (Masters Thesis and Captstone). University of New Hampshire. Retrieved from <https://scholars.unh.edu/thesis/1216>
- Delignette-Muller, M. L., & Dutang, C. (2015). fitdistrplus: An R Package for Fitting Distributions. *Journal of Statistical Software*, 64(4), 1–34.
- Det Norske Veritas. (2010). *Selection and use of Subsea Leak Detection Systems* (No. DNV-RP-F302) (p. 36).
- Dinno, A. (2017). *dunn.test: Dunn's Test of Multiple Comparisons Using Rank Sums*. Retrieved from <https://cran.r-project.org/package=dunn.test>
- Dong, J., Xiao, X., Menarguez, M. A., Zhang, G., Qin, Y., Thau, D., et al. (2016). Mapping paddy rice planting area in northeastern Asia with Landsat 8 images, phenology-based algorithm and Google Earth Engine. *Remote Sensing of Environment*, 185, 142–154. <https://doi.org/10.1016/j.rse.2016.02.016>
- Downing, J A, Prairie, Y. T., Cole, J. J., Duarte, C. M., Tranvik, L. J., Striegl, R. G., et al. (2006). The global abundance and size distribution of lakes, ponds, and impoundments. *Limnology and Oceanography*, 51(5), 2388–2397.
- Downing, John A. (2010). Emerging global role of small lakes and ponds: little things mean a lot. *Limnetica*, 29(1), 9–24.
- Duc, N. T., Silverstein, S., Lundmark, L., Reyier, H., Crill, P., & Bastviken, D. (2013). Automated flux chamber for investigating gas flux at water-air interfaces. *Environmental Science & Technology*, 47(2), 968–75. <https://doi.org/10.1021/es303848x>
- Duc, N. T., Silverstein, S., Wik, M., Crill, P., Bastviken, D., & Varner, R. K. (2019). Greenhouse gas flux studies: An automated online system for gas emission measurements in aquatic environments. *Hydrology and Earth System Sciences Discussions*, 1–18. <https://doi.org/10.5194/hess-2019-83>
- Dziak, R. P., Matsumoto, H., Embley, R. W., Merle, S. G., Lau, T.-K., Baumberger, T., et al. (2018). Passive acoustic records of seafloor methane bubble streams on the

Oregon continental margin. *Deep Sea Research Part II: Topical Studies in Oceanography*, 150, 210–217. <https://doi.org/10.1016/j.dsr2.2018.04.001>

- Ehn, J. K., Mundy, C. J., Barber, D. G., Hop, H., Rossmagel, A., & Stewart, J. (2011). Impact of horizontal spreading on light propagation in melt pond covered seasonal sea ice in the Canadian Arctic. *Journal of Geophysical Research*, 116, C00G02. <https://doi.org/10.1029/2010JC006908>
- Fechner-Levy, E. J., & Hemond, H. F. (1996). Trapped methane volume and potential effects on methane ebullition in a northern peatland. *Limnology and Oceanography*, 41(7), 1375–1383. <https://doi.org/10.4319/lo.1996.41.7.1375>
- Friborg, T., Christensen, T. R., & Søgaard, H. (1997). Rapid response of greenhouse gas emission to early spring thaw in a subarctic mire as shown by micrometeorological techniques. *Geophysical Research Letters*, 24(23), 3061–3064. <https://doi.org/10.1029/97GL03024>
- Fuchs, M., Kuhry, P., & Hugelius, G. (2015). Low below-ground organic carbon storage in a subarctic Alpine permafrost environment. *The Cryosphere*, 9(2), 427–438. <https://doi.org/10.5194/tc-9-427-2015>
- Gignac, L. D., Vitt, D. H., & Bayley, S. E. (1991). Bryophyte response surfaces along ecological and climatic gradients. *Plant Ecology*, 93(1), 29–237.
- Glaser, P. H., Hansen, B., Siegel, D. I., Reeve, A. S., & Morin, P. (2004). Rates, pathways and drivers for peatland development in the Hudson Bay Lowlands, northern Ontario, Canada. *Journal of Ecology*, 92(6), 1036–2745.
- Glaser, P. H., Chanton, J. P., Morin, P., Rosenberry, D. O., Siegel, D. I., Ruud, O., et al. (2004). Surface deformations as indicators of deep ebullition fluxes in a large northern peatland. *Global Biogeochemical Cycles*, 18(1).
- Goodrich, J. P., Varner, R. K., Frolking, S., Duncan, B. N., & Crill, P. M. (2011). High-frequency measurements of methane ebullition over a growing season at a temperate peatland site. *Geophysical Research Letters*, 38(7). <https://doi.org/10.1029/2011GL046915>
- Gorham, E. (1991). Northern Peatlands: Role in the carbon cycle and probable responses to climatic warming. *Ecological Applications*, 1(2), 182–195.
- Green, S. M., Baird, A. J., Boardman, C. P., & Gauci, V. (2014). A mesocosm study of the effect of restoration on methane (CH₄) emissions from blanket peat. *Wetlands Ecology and Management*, 22(5), 523–537. <https://doi.org/10.1007/s11273-014-9349-3>

- Greene, C. A., & Wilson, P. S. (2012). Laboratory investigation of a passive acoustic method for measurement of underwater gas seep ebullition. *The Journal of the Acoustical Society of America*, *131*(1), EL61–EL66. <https://doi.org/10.1121/1.3670590>
- Greene, S., Walter Anthony, K. M., Archer, D., Sepulveda-Jauregui, A., & Martinez-Cruz, K. (2014). Modeling the impediment of methane ebullition bubbles by seasonal lake ice. *Biogeosciences*, *11*(23), 6791–6811. <https://doi.org/10.5194/bg-11-6791-2014>
- Greinert, J., & Nützel, B. (2004). Hydroacoustic experiments to establish a method for the determination of methane bubble fluxes at cold seeps. *Geo-Marine Letters*, *24*(2), 75–85.
- Grinham, A., Albert, S., Deering, N., Dunbabin, M., Bastviken, D., Sherman, B., et al. (2018). The importance of small artificial water bodies as sources of methane emissions in Queensland, Australia. *Hydrology and Earth System Sciences*, *22*(10), 5281–5298. <https://doi.org/10.5194/hess-22-5281-2018>
- Hamilton, J. D., Kelly, C. A., Rudd, J. W. M., Hesslein, R. H., & Roulet, N. T. (1994). Flux to the atmosphere of CH₄ and CO₂ from wetland ponds on the Hudson Bay lowlands (HBLs). *Journal of Geophysical Research*, *99*, 1495–1510.
- Hartley, Iain. P., Hill, Timothy. C., Wade, Thomas. J., Clement, Robert. J., Moncrieff, John. B., Prieto-Blanco, Ana., et al. (2015). Quantifying landscape-level methane fluxes in subarctic Finland using a multiscale approach. *Global Change Biology*, *21*(10), 3712–3725. <https://doi.org/10.1111/gcb.12975>
- Hodgkins, S. B., Tfaily, M. M., McCalley, C. K., Logan, T. A., Crill, P. M., Saleska, S. R., et al. (2014). Changes in peat chemistry associated with permafrost thaw increase greenhouse gas production. *Proceedings of the National Academy of Sciences*, *111*(16), 5819–5824.
- Holgerson, M. A., & Raymond, P. A. (2016). Large contribution to inland water CO₂ and CH₄ emissions from very small ponds. *Nature Geoscience*, *9*(3), 222–226. <https://doi.org/10.1038/ngeo2654>
- Holmes, C. D., Prather, M. J., Søvde, O. A., & Myhre, G. (2013). Future methane, hydroxyl, and their uncertainties: key climate and emission parameters for future predictions. *Atmospheric Chemistry and Physics*, *13*(1), 285–302.
- Hugelius, G., Strauss, J., Zubrzycki, S., Harden, J. W., Schuur, E., Ping, C.-L., et al. (2014). Estimated stocks of circumpolar permafrost carbon with quantified uncertainty ranges and identified data gaps. *Biogeosciences*, *11*(23), 6573–6593.

- Immerzeel, W. W., Kraaijenbrink, P. D. A., Shea, J. M., Shrestha, A. B., Pellicciotti, F., Bierkens, M. F. P., & de Jong, S. M. (2014). High-resolution monitoring of Himalayan glacier dynamics using unmanned aerial vehicles. *Remote Sensing of Environment*, *150*, 93–103. <https://doi.org/10.1016/j.rse.2014.04.025>
- Inoue, J., Curry, J. A., & Maslanik, J. A. (2008). Application of Aerosondes to Melt-Pond Observations over Arctic Sea Ice. *Journal of Atmospheric and Oceanic Technology*, *25*(2), 327–334. <https://doi.org/10.1175/2007JTECHA955.1>
- Jackson, D. R., Williams, K. L., Wever, T. F., Friedrichs, C. T., & Wright, L. D. (1998). Sonar evidence for methane ebullition in Eckernförde Bay. *Continental Shelf Research*, *18*(14–15), 1893–1915. [https://doi.org/10.1016/S0278-4343\(98\)00062-4](https://doi.org/10.1016/S0278-4343(98)00062-4)
- Jammet, M., Crill, P., Dengel, S., & Friborg, T. (2015). Large methane emissions from a subarctic lake during spring thaw: Mechanisms and landscape significance. *Journal of Geophysical Research: Biogeosciences*, *120*(11), 2289–2305.
- Jammet, M., Dengel, S., Kettner, E., Parmentier, F.-J. W., Wik, M., Crill, P., & Friborg, T. (2017). Year-round CH₄ and CO₂ flux dynamics in two contrasting freshwater ecosystems of the subarctic. *Biogeosciences Discussions*, 1–49. <https://doi.org/10.5194/bg-2016-466>
- Johansson, T., Malmer, N., Crill, P. M., Friborg, T., Akerman, J. H., Mastepanov, M., & Christensen, T. R. (2006). Decadal vegetation changes in a northern peatland, greenhouse gas fluxes and net radiative forcing. *Global Change Idots*, *12*(12), 2352–2369. <https://doi.org/10.1111/j.1365-2486.2006.01267.x>
- Jorgenson, M. T., Harden, J., Kanevskiy, M., O'Donnell, J., Wickland, K., Ewing, S., et al. (2013). Reorganization of vegetation, hydrology and soil carbon after permafrost degradation across heterogeneous boreal landscapes. *Environmental Research Letters*, *8*(3), 035017. <https://doi.org/10.1088/1748-9326/8/3/035017>
- Joyce, J., & Jewell, P. W. (2003). Physical controls on methane ebullition from reservoirs and lakes. *Environmental & Engineering Geoscience*, *9*(2), 167–178.
- Kim, D., Hwang, B., Chung, K. H., Lee, S. H., Jung, H.-S., & Moon, W. M. (2013). Melt pond mapping with high-resolution SAR: the first view. *Proceedings of the IEEE*, *101*(3), 748–758.
- King, J. Y., Reeburgh, W. S., & Regli, S. K. (1998). Methane emission and transport by arctic sedges in Alaska: Results of a vegetation removal experiment. *Journal of Geophysical Idots*, *103*. Retrieved from <http://onlinelibrary.wiley.com/doi/10.1029/98JD00052/full>

- Kirschke, S., Bousquet, P., Ciais, P., Saunois, M., Canadell, J. G., Dlugokencky, E. J., et al. (2013). Three decades of global methane sources and sinks. *Nature Geoscience*, 6(10), 813–823. <https://doi.org/10.1038/ngeo1955>
- Kraaijenbrink, P. D. A., Shea, J. M., Pellicciotti, F., Jong, S. M. de, & Immerzeel, W. W. (2016). Object-based analysis of unmanned aerial vehicle imagery to map and characterise surface features on a debris-covered glacier. *Remote Sensing of Environment*, 186, 581–595. <https://doi.org/10.1016/j.rse.2016.09.013>
- Kuhn, M., Lundin, E. J., Giesler, R., Johansson, M., & Karlsson, J. (2018). Emissions from thaw ponds largely offset the carbon sink of northern permafrost wetlands. *Scientific Reports*, 8(1), 1–7. <https://doi.org/10.1038/s41598-018-27770-x>
- Kutzbach, L., Wagner, D., & Pfeiffer, E.-M. (2004). Effect of microrelief and vegetation on methane emission from wet polygonal tundra, Lena Delta, Northern Siberia. *Biogeochemistry*, 69(3), 341–362.
- Laurion, I., Vincent, W. F., MacIntyre, S., Retamal, L., Dupont, C., Francus, P., & Pienitz, R. (2010). Variability in greenhouse gas emissions from permafrost thaw ponds. *Limnology and Oceanography*, 55(1), 115–133. <https://doi.org/10.4319/lo.2010.55.1.0115>
- Lehner, B., & Döll, P. (2004). Development and validation of a global database of lakes, reservoirs and wetlands. *Journal of Hydrology*, 296(1–4), 1–22. <https://doi.org/10.1016/j.jhydrol.2004.03.028>
- Liebner, S., Ganzert, L., Kiss, A., Yang, S., Wagner, D., & Svenning, M. M. (2015). Shifts in methanogenic community composition and methane fluxes along the degradation of discontinuous permafrost. *Frontiers in Microbiology*, 6.
- Liu, W., Dong, J., Xiang, K., Wang, S., Han, W., & Yuan, W. (2018). A sub-pixel method for estimating planting fraction of paddy rice in Northeast China. *Remote Sensing of Environment*, 205(December 2017), 305–314. <https://doi.org/10.1016/j.rse.2017.12.001>
- Loisel, J., Yu, Z., Beilman, D. W., Camill, P., Alm, J., Amesbury, M. J., et al. (2014). A database and synthesis of northern peatland soil properties and Holocene carbon and nitrogen accumulation. *The Holocene*, 24(9), 1028–1042.
- Lundin, E. J., Giesler, R., Persson, A., Thompson, M. S., & Karlsson, J. (2013). Integrating carbon emissions from lakes and streams in a subarctic catchment: CARBON EMISSIONS FROM LAKES AND STREAMS. *Journal of Geophysical Research: Biogeosciences*, 118(3), 1200–1207. <https://doi.org/10.1002/jgrg.20092>

- Lundin, E. J., Klaminder, J., Giesler, R., Persson, A., Olefeldt, D., Heliasz, M., et al. (2016). Is the subarctic landscape still a carbon sink? Evidence from a detailed catchment balance. *Geophysical Research Letters*, *43*(5), 1988–8007.
- Maher, D. T., Drexler, M., Tait, D. R., Johnston, S. G., & Jeffrey, L. C. (2019). iAMES: An inexpensive, Automated Methane Ebullition Sensor. *Environmental Science & Technology*, *53*(11), 6420–6426. <https://doi.org/10.1021/acs.est.9b01881>
- Malhotra, A., & Roulet, N. T. (2015). Environmental correlates of peatland carbon fluxes in a thawing landscape: do transitional thaw stages matter? *Biogeosciences*, *12*(10), 3119–3130.
- Malmer, N., Johansson, T., Olsrud, M., & Christensen, T. R. (2005). Vegetation, climatic changes and net carbon sequestration in a North-Scandinavian subarctic mire over 30 years. *Global Change & Ecology*, *11*, 1895–1909. <https://doi.org/10.1111/j.1365-2486.2005.01042.x>
- Markus, T., Cavalieri, D. J., Tschudi, M. A., & Ivanoff, A. (2003). Comparison of aerial video and Landsat 7 data over ponded sea ice. *Remote Sensing of Environment*, *86*(4), 458–469.
- Marris, E. (2013). FLY , AND BRING ME DATA. *Nature*, *498*, 156–158. <https://doi.org/10.1038/498156a>
- Miles, E. S., Pellicciotti, F., Willis, I. C., Steiner, J. F., Buri, P., & Arnold, N. S. (2016). Refined energy-balance modelling of a supraglacial pond, Langtang Khola, Nepal. *Annals of Glaciology*, *57*(71), 29–40. <https://doi.org/10.3189/2016AoG71A421>
- Moore, T. R., De Young, A., Bubier, J. L., Humphreys, E. R., Lafleur, P. M., & Roulet, N. T. (2011). A Multi-Year Record of Methane Flux at the Mer Bleue Bog, Southern Canada. *Ecosystems*, *14*(4), 646–657. <https://doi.org/10.1007/s10021-011-9435-9>
- Muster, S., Langer, M., Heim, B., Westermann, S., & Boike, J. (2012). Subpixel heterogeneity of ice-wedge polygonal tundra: a multi-scale analysis of land cover and evapotranspiration in the Lena River Delta, Siberia. *Tellus B*, *64*(2012), 1–21. <https://doi.org/10.3402/tellusb.v64i0.17301>
- Muster, Sina, Heim, B., Abnizova, A., & Boike, J. (2013). Water body distributions across scales: a remote sensing based comparison of three arctic tundra wetlands. *Remote Sensing*, *5*(4), 1498–1523.
- Nakagawa, S., & Schielzeth, H. (2013). A general and simple method for obtaining R² from generalized linear mixed-effects models. *Methods in Ecology and Evolution*, *4*(2), 133–142. <https://doi.org/10.1111/j.2041-210x.2012.00261.x>

- Negandhi, K., Laurion, I., Whiticar, M. J., Galand, P. E., Xu, X., & Lovejoy, C. (2013). Small thaw ponds: an unaccounted source of methane in the canadian high arctic. *PloS One*, 8(11), e78204–e78204. <https://doi.org/10.1371/journal.pone.0078204>
- Noyce, G. L., Varner, R. K., Bubier, J. L., & Frohling, S. (2014). Effect of *Carex rostrata* on seasonal and interannual variability in peatland methane emissions. *Journal of Geophysical Research: Biogeosciences*, 119(1), 24–34. <https://doi.org/10.1002/2013JG002474>
- O'Donnell, J. A., Jorgenson, M. T., Harden, J. W., McGuire, A. D., Kanevskiy, M. Z., & Wickland, K. P. (2011). The Effects of Permafrost Thaw on Soil Hydrologic, Thermal, and Carbon Dynamics in an Alaskan Peatland. *Ecosystems*, 15(2), 213–229. <https://doi.org/10.1007/s10021-011-9504-0>
- O'Haver, T. (2020a). *Peak finding and measurement, 2019*. MATLAB. Retrieved from <https://www.mathworks.com/matlabcentral/fileexchange/11755-peak-finding-and-measurement-2019>
- O'Haver, T. (2020b). Pragmatic Introduction to Signal Processing: Applications in scientific measurement. The University of Maryland at College Park. Retrieved from <https://terpconnect.umd.edu/~toh/spectrum/index.html>
- Olefeldt, D., & Roulet, N. T. (2012). Effects of permafrost and hydrology on the composition and transport of dissolved organic carbon in a subarctic peatland complex. *Journal of Geophysical Research*, 117(G1), G01005. <https://doi.org/10.1029/2011JG001819>
- Olefeldt, D., Roulet, N., Giesler, R., & Persson, A. (2013). Total waterborne carbon export and DOC composition from ten nested subarctic peatland catchments—importance of peatland cover, groundwater influence, and inter-annual variability of precipitation patterns. *Hydrological Processes*, 27(16), 2280–2294. <https://doi.org/10.1002/hyp.9358>
- Ostrovsky, I., McGinnis, D. F., Lapidus, L., & Eckert, W. (2008). Quantifying gas ebullition with echosounder: the role of methane transport by bubbles in a medium-sized lake. *Limnology and Oceanography: Methods*, 6(2), 105–118.
- Ostrovsky, I. (2003). Methane bubbles in Lake Kinneret: Quantification and temporal and spatial heterogeneity. *Limnology and Oceanography*, 48(3), 1030–1036. <https://doi.org/10.4319/lo.2003.48.3.1030>
- Paine, J., Andrews, J., Saylam, K., & Tremblay, T. (2015). Airborne LiDAR-Based Wetland and Permafrost-Feature Mapping on an Arctic Coastal Plain, North Slope, Alaska. In R. Tiner, M. Lang, & V. Klemas (Eds.), *Remote Sensing of Wetlands* (pp. 413–434). CRC Press. <https://doi.org/10.1201/b18210-23>

- Palace, M., Herrick, C., DelGreco, J., Finnell, D., Garnello, A., McCalley, C., et al. (2018). Determining Subarctic Peatland Vegetation Using an Unmanned Aerial System (UAS). *Remote Sensing*, 10(9), 1498. <https://doi.org/10.3390/rs10091498>
- Persson, A., Hasan, A., Tang, J., & Pilesjö, P. (2012). Modelling Flow Routing in Permafrost Landscapes with TWI: An Evaluation against Site-Specific Wetness Measurements. *Transactions in GIS*, 16(5), 701–713. <https://doi.org/10.1111/j.1467-9671.2012.01338.x>
- Polishchuk, Y., Bogdanov, A. N., Muratov, I. N., Polishchuk, V. Y., Lim, A., Manasypov, R. M., et al. (2018). Minor contribution of small thaw ponds to the pools of carbon and methane in the inland waters of the permafrost-affected part of the Western Siberian Lowland. *Environmental Research Letters*, 13, 045002.
- QGIS Development Team. (2020). QGIS Geographic Information System (Version 2.14.21). Open Source Geospatial Foundation Project. Retrieved from <http://qgis.osgeo.org>
- R Core Team. (2017). *R: A language and environment for statistical computing*. Vienna, Austria: R Foundation for Statistical Computing. Retrieved from <https://www.r-project.org/>
- R Core Team. (2019). *R: A language and environment for statistical computing*. Vienna, Austria: R Foundation for Statistical Computing. Retrieved from <https://www.R-project.org/>
- Räsänen, A., Aurela, M., Juutinen, S., Kumpula, T., Lohila, A., Penttilä, T., & Virtanen, T. (2019). Detecting northern peatland vegetation patterns at ultra-high spatial resolution. *Remote Sensing in Ecology and Conservation*, rse2.140. <https://doi.org/10.1002/rse2.140>
- Rosenberry, D. O., Glaser, P. H., Siegel, D. I., & Weeks, E. P. (2003). Use of hydraulic head to estimate volumetric gas content and ebullition flux in northern peatlands. *Water Resources Research*, 39(3 %@ 1944-7973), 1–10. <https://doi.org/10.1029/2002WR001377>
- Rychert, K. M., & Weber, T. C. (2020). Tests of Acoustic Target Strength and Bubble Dissolution Models Using a Synthetic Bubble Generator. *Journal of Atmospheric and Oceanic Technology*, 37(1), 129–140. <https://doi.org/10.1175/JTECH-D-19-0133.1>
- Sachs, T., Wille, C., Boike, J., & Kutzbach, L. (2008). Environmental controls on ecosystem-scale CH₄ emission from polygonal tundra in the Lena River Delta, Siberia. *Journal of Geophysical Research*, 113.

- Saunois, M., Bousquet, P., Poulter, B., Peregon, A., Ciais, P., Canadell, J. G., et al. (2016). The global methane budget 2000-2012. *Earth System Science Data*, 8(2), 697–751. <https://doi.org/10.5194/essd-8-697-2016>
- Schlesinger, W. H., & Bernhardt, E. S. (2013). *Biogeochemistry: An Analysis of Global Change* (3rd ed.). Academic Press.
- Schuur, E. A. G., Bockheim, J., Canadell, J. G., Euskirchen, E., Field, C. B., Goryachkin, S. V., et al. (2008). Vulnerability of Permafrost Carbon to Climate Change: Implications for the Global Carbon Cycle. *BioScience*, 58(8), 701. <https://doi.org/10.1641/B580807>
- Segers, R. (1998). Methane production and methane consumption: a review of processes underlying wetland methane fluxes. *Biogeochemistry*, 41(1), 23–51.
- Shirokova, L. S., Pokrovsky, O. S., Kirpotin, S. N., Desmukh, C., Pokrovsky, B. G., Audry, S., & Viers, J. (2013). Biogeochemistry of organic carbon, CO₂, CH₄, and trace elements in thermokarst water bodies in discontinuous permafrost zones of Western Siberia. *Biogeochemistry*, 113(1–3), 573–593. <https://doi.org/10.1007/s10533-012-9790-4>
- Stocker, T. F., Qin, D., Plattner, G.-K., Tignor, M., Allen, S. K., Boschung, J., et al. (2013). IPCC, 2013: Climate Change 2013: The Physical Science Basis. Contribution of Working Group I to the First Assessment Report of the Intergovernmental Panel on Climate Change. In T. F. Stocker, D. Qin, G. K. Plattner, M. Tignor, S. K. Allen, J. Boschung, et al. (Eds.), *CEUR Workshop Proceedings* (Vol. 1542, p. 1535).
- Stoffer, D. (2019). *astsa: Applied Statistical Time Series Analysis* (Version R package version 1.9). Retrieved from <https://CRAN.R-project.org/package=astsa>
- Strasberg, M. (1953). The Pulsation Frequency of Nonspherical Gas Bubbles in Liquids. *The Journal of the Acoustical Society of America*, 25(3), 536–537. <https://doi.org/10.1121/1.1907076>
- Strasberg, M. (1956). Gas Bubbles as Sources of Sound in Liquids. *The Journal of the Acoustical Society of America*, 28(1), 20–26. <https://doi.org/10.1121/1.1908212>
- Striegl, R. G., & Michmerhuizen, C. M. (1998). Hydrologic influence on methane and carbon dioxide dynamics at two north-central Minnesota lakes. *Limnology and Oceanography*, 43, 1519–1529. <https://doi.org/10.4319/lo.1998.43.7.1519>
- Ström, L., & Christensen, T. R. (2007). Below ground carbon turnover and greenhouse gas exchanges in a sub-arctic wetland. *Soil Biology and Biochemistry*, 39(7), 1689–1698. <https://doi.org/10.1016/j.soilbio.2007.01.019>

- Svensson, B. H., Christensen, T. R., Johansson, E., & Öquist, M. (1999). Interdecadal Changes in CO₂ and CH₄ Fluxes of a Subarctic Mire: Stordalen Revisited after 20 Years. *Oikos*, *85*, 22–30.
- Tarnocai, C., Canadell, J. G., Schuur, E. a. G., Kuhry, P., Mazhitova, G., & Zimov, S. (2009). Soil organic carbon pools in the northern circumpolar permafrost region. *Global Biogeochemical Cycles*, *23*(2). <https://doi.org/10.1029/2008GB003327>
- Tokida, T., Miyazaki, T., Mizoguchi, M., Nagata, O., Takakai, F., Kagemoto, A., & Hatano, R. (2007). Falling atmospheric pressure as a trigger for methane ebullition from peatland. *Global Biogeochemical Cycles*, *21*(2).
- Tokida, T., Miyazaki, T., & Mizoguchi, M. (2009). Physical Controls on Ebullition Losses of Methane from Peatlands. In *Carbon Cycling in Northern Peatlands* (pp. 219–228). <https://doi.org/10.1029/2008GM000805>
- Tschudi, M. A., Maslanik, J. A., & Perovich, D. K. (2008). Derivation of melt pond coverage on Arctic sea ice using MODIS observations. *Remote Sensing of Environment*, *112*(5), 2605–2614.
- Tuittila, E.-S., Juutinen, S., Froking, S., Väliiranta, M., Laine, A. M., Miettinen, A., et al. (2013). Wetland chronosequence as a model of peatland development: Vegetation succession, peat and carbon accumulation. *The Holocene*, *23*(1), 25–35. <https://doi.org/10.1177/0959683612450197>
- Turetsky, M. R., Abbott, B. W., Jones, M. C., Anthony, K. W., Olefeldt, D., Schuur, E. A. G., et al. (2020). Carbon release through abrupt permafrost thaw. *Nature Geoscience*, *13*(2), 138–143. <https://doi.org/10.1038/s41561-019-0526-0>
- Vagle, S., Hume, J., McLaughlin, F., MacIsaac, E., & Shortreed, K. (2010). A methane bubble curtain in meromictic Sakinaw Lake, British Columbia. *Limnology and Oceanography*, *55*(3), 1313–1326. <https://doi.org/10.4319/lo.2010.55.3.1313>
- Varadharajan, C., & Hemond, H. F. (2012). Time-series analysis of high-resolution ebullition fluxes from a stratified, freshwater lake. *Journal of Geophysical Research*, *117*(G2). <https://doi.org/10.1029/2011JG001866>
- Varadharajan, C., Hermosillo, R., & Hemond, H. F. (2010). A low-cost automated trap to measure bubbling gas fluxes. *Limnology and Oceanography*, *8*, 363–375.
- Verpoorter, C., Kutser, T., Seekell, D. A., & Tranvik, L. J. (2014). A global inventory of lakes based on high-resolution satellite imagery. *Geophysical Research Letters*, *41*(18), 6396–6402.

- Vitt, D. H., & Slack, N. G. (1975). An analysis of the vegetation of Sphagnum-dominated kettle-hole bogs in relation to environmental gradients. *Canadian Journal of Botany*, 53(4), 332–4026.
- Walter, K. M., Zimov, S. a, Chanton, J. P., Verbyla, D., & Chapin, F. S. (2006). Methane bubbling from Siberian thaw lakes as a positive feedback to climate warming. *Nature*, 443(7107), 71–75. <https://doi.org/10.1038/nature05040>
- Wang, M., Su, J., Li, T., Xiaoyu, W., Ji, Q., Cao, Y., et al. (2018). Determination of Arctic melt pond fraction and sea ice roughness from Unmanned Aerial Vehicle (UAV) imagery, 29(3), 10.
- Weyhenmeyer, C. E. (1999). Methane emissions from beaver ponds: rates, patterns, and transport mechanisms. *Global Biogeochemical Cycles*, 13(4), 1079–1090.
- Whalen, S. C. (2005). Biogeochemistry of methane exchange between natural wetlands and the atmosphere. *Environmental Engineering Science*, 22(1), 73–94.
- Wiggins, S. M., Leifer, I., Linke, P., & Hildebrand, J. A. (2015). Long-term acoustic monitoring at North Sea well site 22/4b. *Marine and Petroleum Geology*, 68, 776–788. <https://doi.org/10.1016/j.marpetgeo.2015.02.011>
- Wik, M., Crill, P. M., Bastviken, D., Danielsson, V. A., & Norbäck, E. (2011). Bubbles trapped in arctic lake ice: Potential implications for methane emissions. *Journal of Geophysical Research*, 116(G3), G03044. <https://doi.org/10.1029/2011JG001761>
- Wik, M., Crill, P. M., Varner, R. K., & Bastviken, D. (2013). Multiyear measurements of ebullitive methane flux from three subarctic lakes. *Journal of Geophysical Research: Biogeosciences*, 118(April), 1307–1321. <https://doi.org/10.1002/jgrg.20103>
- Wik, M., Thornton, B. F., Bastviken, D., MacIntyre, S., Varner, R. K., & Crill, P. M. (2014). Energy input is primary controller of methane bubbling in subarctic lakes. *Geophysical Research Letters*, 41(2), 555–560.
- Wik, M., Thornton, B. F., Bastviken, D., Uhlbäck, J., & Crill, P. M. (2016). Biased sampling of methane release from northern lakes : A problem for extrapolation. *Geophysical Research Letters*, 43, 1256–1262. <https://doi.org/10.1002/2015GL066501.Received>
- Wik, M., Varner, R. K., Anthony, K. W., MacIntyre, S., & Bastviken, D. (2016). Climate-sensitive northern lakes and ponds are critical components of methane release. *Nature Geoscience*, 9(2), 99–105. <https://doi.org/10.1038/ngeo2578>
- Wik, M., Johnson, J. E., Crill, P. M., DeStasio, J. P., Erickson, L., Halloran, M. J., et al. (2018). Sediment characteristics and methane ebullition in three subarctic lakes.

Journal of Geophysical Research: Biogeosciences, 2399–2411.
<https://doi.org/10.1029/2017JG004298>

- Wilson, J. O., Crill, P. M., Bartlett, K. B., Sebacher, D. I., Harriss, R. C., & Sass, R. L. (1989). Seasonal variation of methane emissions from a temperate swamp. *Biogeochemistry*, 8(1), 55–71. <https://doi.org/10.1007/BF02180167>
- Wu, Q., & Lane, C. R. (2017). Delineating wetland catchments and modeling hydrologic connectivity using lidar data and aerial imagery. *Hydrology and Earth System Sciences*, 21(7), 3579–3595. <https://doi.org/10.5194/hess-21-3579-2017>
- Wu, Q., Lane, C. R., Li, X., Zhao, K., Zhou, Y., Clinton, N., et al. (2019). Integrating LiDAR data and multi-temporal aerial imagery to map wetland inundation dynamics using Google Earth Engine. *Remote Sensing of Environment*, 228, 1–13. <https://doi.org/10.1016/j.rse.2019.04.015>
- Xia, H., Zhao, W., Li, A., Bian, J., & Zhang, Z. (2017). Subpixel inundation mapping using landsat-8 OLI and UAV data for a wetland region on the zoige plateau, China. *Remote Sensing*, 9(1), 1–22. <https://doi.org/10.3390/rs9010031>
- Yu, Z., Loisel, J., Brosseau, D. P., Beilman, D. W., & Hunt, S. J. (2010). Global peatland dynamics since the Last Glacial Maximum. *Geophysical Research Letters*, 37(13).
- Zeikus, J. G., & Winfrey, M. R. (1976). Temperature Limitation of Methanogenesis in Aquatic Sediments. *APPL. ENVIRON. MICROBIOL.*, 31, 9.
- Zhou, Y., Xiao, X., Qin, Y., Dong, J., Zhang, G., Kou, W., et al. (2016). Mapping paddy rice planting area in rice-wetland coexistent areas through analysis of Landsat 8 OLI and MODIS images. *International Journal of Applied Earth Observation and Geoinformation*, 46, 1–12. <https://doi.org/10.1016/j.jag.2015.11.001>
- Zimov, S. a, Schuur, E. a G., & Chapin, F. S. (2006). Climate change. Permafrost and the global carbon budget. *Science (New York, N.Y.)*, 312(5780), 1612–1613. <https://doi.org/10.1126/science.1128908>
- Zuur, A. F., Ieno, E. N., & Elphick, C. S. (2010). A protocol for data exploration to avoid common statistical problems. *Methods in Ecology and Evolution*, 1(1), 3–14.

APPENDIX A: CHAPTER 1 SUPPLEMENTARY MATERIALS⁴

A.1 Introduction

This supplemental file contains figures and tables that support the main manuscript. In Figure S1 we have provided images of each of the sampled ponds. In Figure S2 we show the daily CH₄ ebullitive emissions from each pond across all sampling seasons. In Figures S3 and S4, we present emissions of CH₄ for ponds *B*, *C*, *E* and *H* (chosen due to the statistically significant differences between their fluxes) from 2014 and 2015, respectively. Figure S5 shows the variability in ebullitive flux for each month in the sampling season. Figure S6 shows the variability in ebullitive flux for each sampling season. Figure S7 shows the variability in ebullitive flux between ponds for each month. Figure S8 shows the variability in ebullitive flux between ponds for each sampling season. Table S1 shows measurements of water table depth and dissolved oxygen collected during pond surveys in 2013 and 2014. Table S2 shows associations between chosen meteorological variables and ebullitive flux. Table S3 and S4 show the pairwise comparisons of ebullitive flux between months within each pond and between ponds within each month respectively. Table S5 and S6 shows the pairwise comparisons of

⁴ This supplementary material has been published: Burke, S. A., Wik, M., Lang, A., Contosta, A. R., Palace, M., Crill, P. M., & Varner, R. K. (2019). Long-Term Measurements of Methane Ebullition from Thaw Ponds. *Journal of Geophysical Research: Biogeosciences*, 2018JG004786. <https://doi.org/10.1029/2018JG004786>

ebullitive flux between sampling seasons within each pond and between ponds within each sampling season respectively.

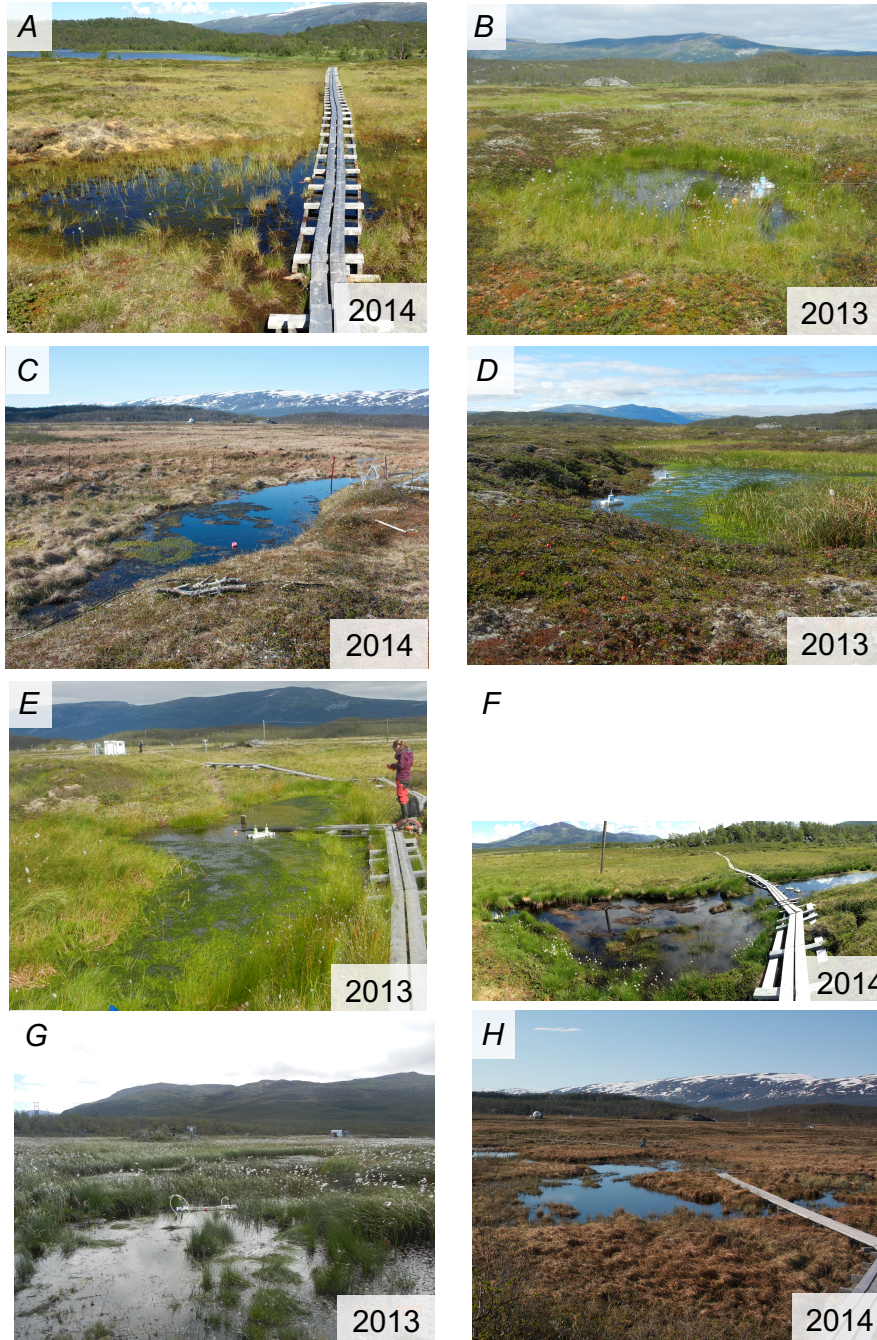


Figure A.1 Images of each pond measured in this study with a label corresponding to the pond identifier and year in which the photo was taken. In some photos, the bubble traps are visible, in others they are not due to them not being deployed yet when the photo was taken. Photos taken in 2013 were all taken by Ruth K. Varner. Photos taken in 2014 were taken by Sophia Burke. (Supplementary Figure S1 in Burke et al., 2019).

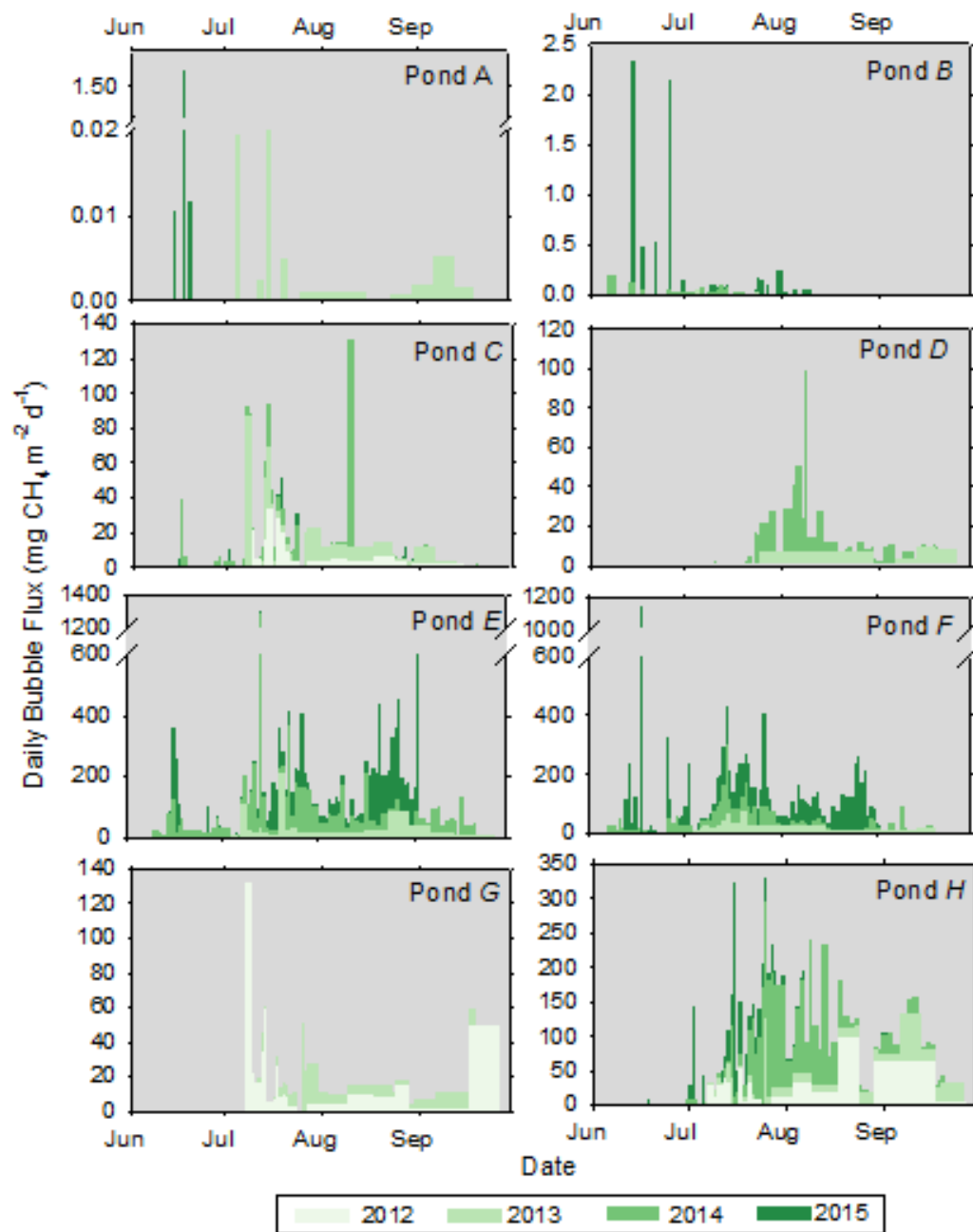


Figure A.2 Measured daily CH₄ emissions (mg m⁻² d⁻¹) for each pond at the Stordalen Mire, Abisko Sweden. (Supplementary Figure S2 in Burke et al., 2019).

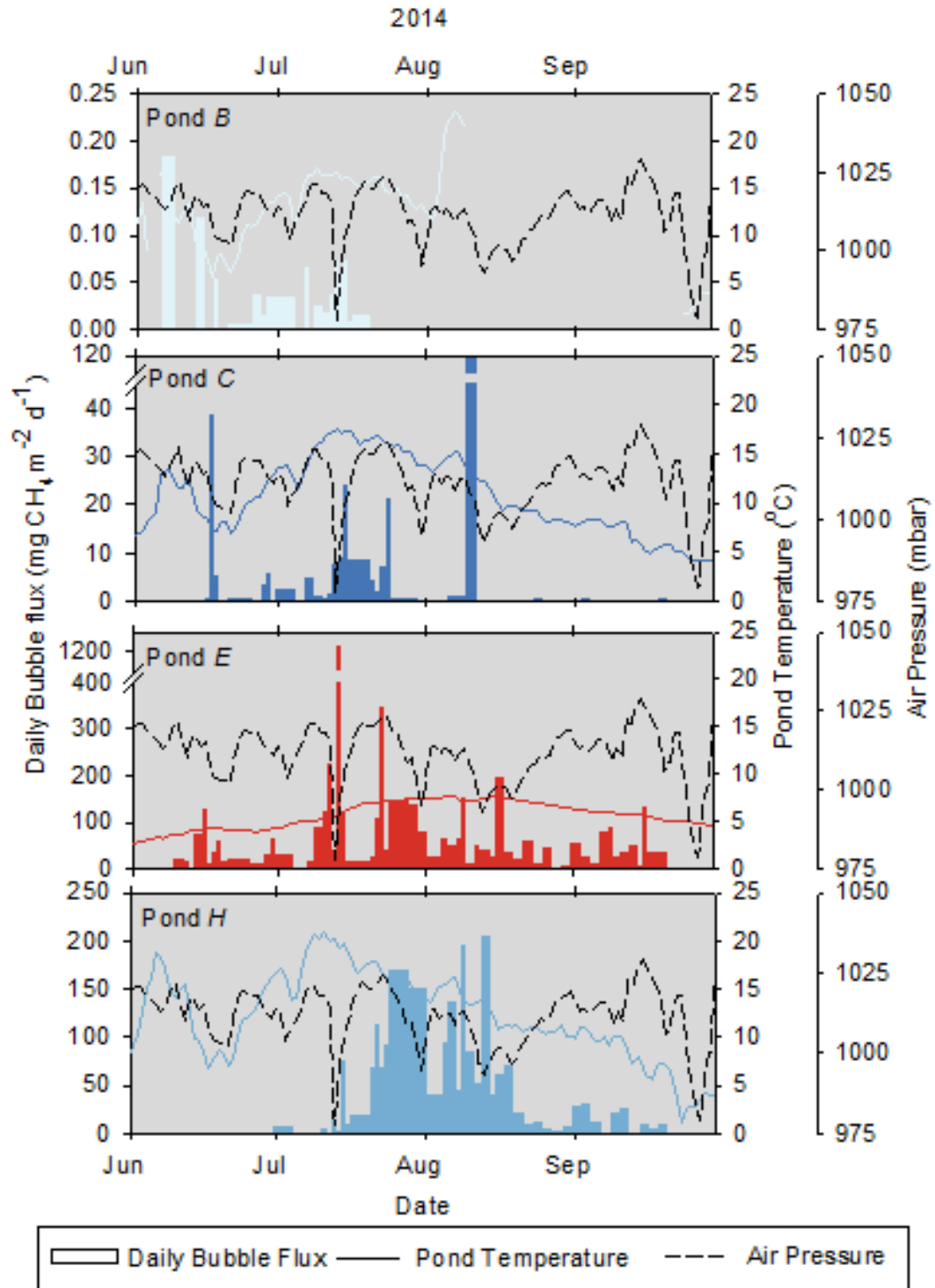


Figure A.3 Measured daily CH₄ flux from ponds B, C, E, and H respectively during the 2014 field season compared to pond temperature (°C), and atmospheric pressure (mbar)(ANS, 2017). These ponds were chosen to represent the variability in flux compared to meteorological conditions due to their statistically significantly different fluxes when compared to each other (see full text). (Supplementary Figure S3 in Burke et al., 2019).

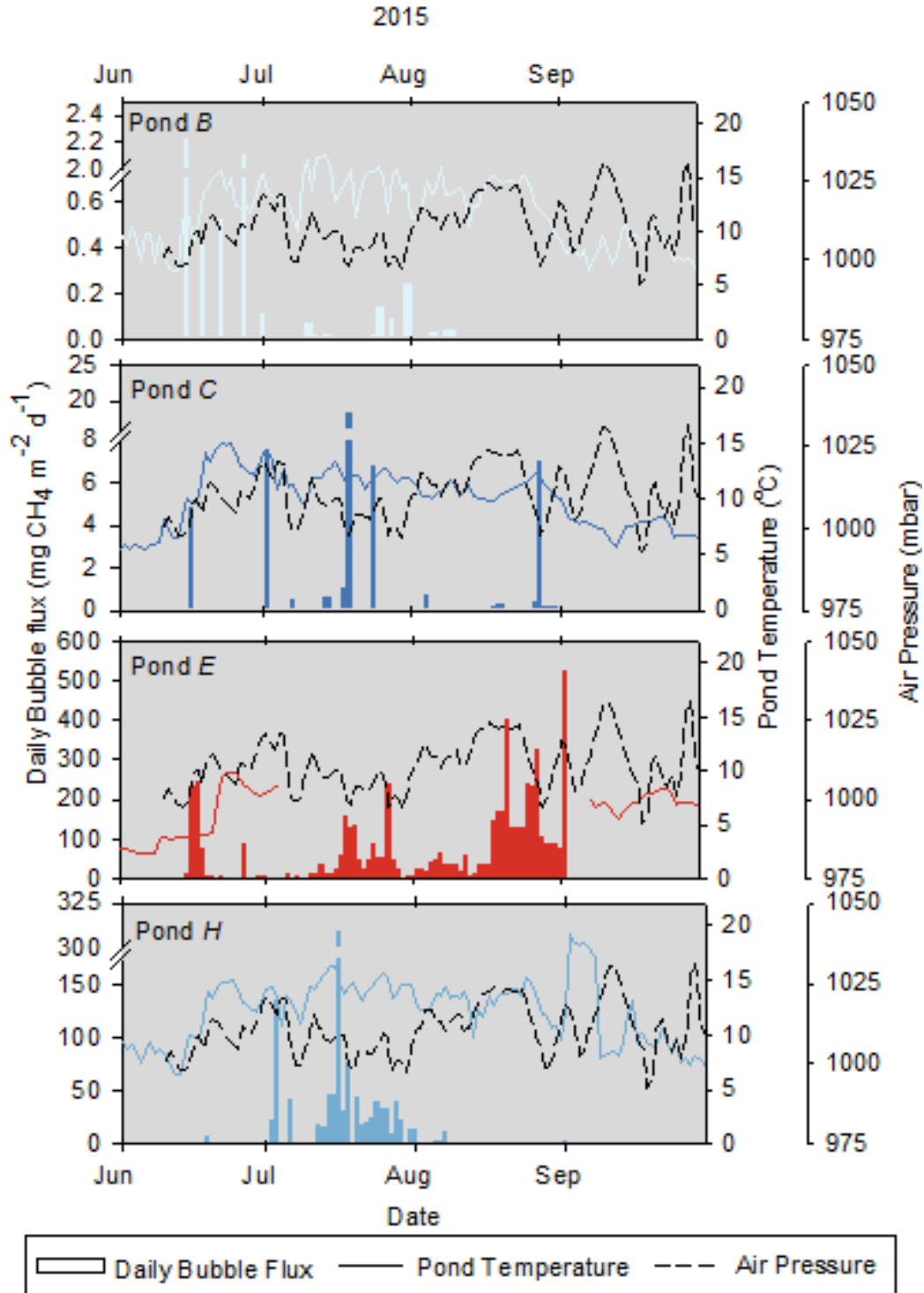


Figure A.4 Measured daily CH₄ flux from ponds B, C, E, and H respectively during the 2015 field season compared to pond temperature (°C), and atmospheric pressure (mbar) (ANS, 2017). These ponds were chosen to represent the variability in flux compared to meteorological conditions due to their statistically significantly different fluxes when compared to each other (see full text). (Supplementary Figure S4 in Burke et al., 2019).

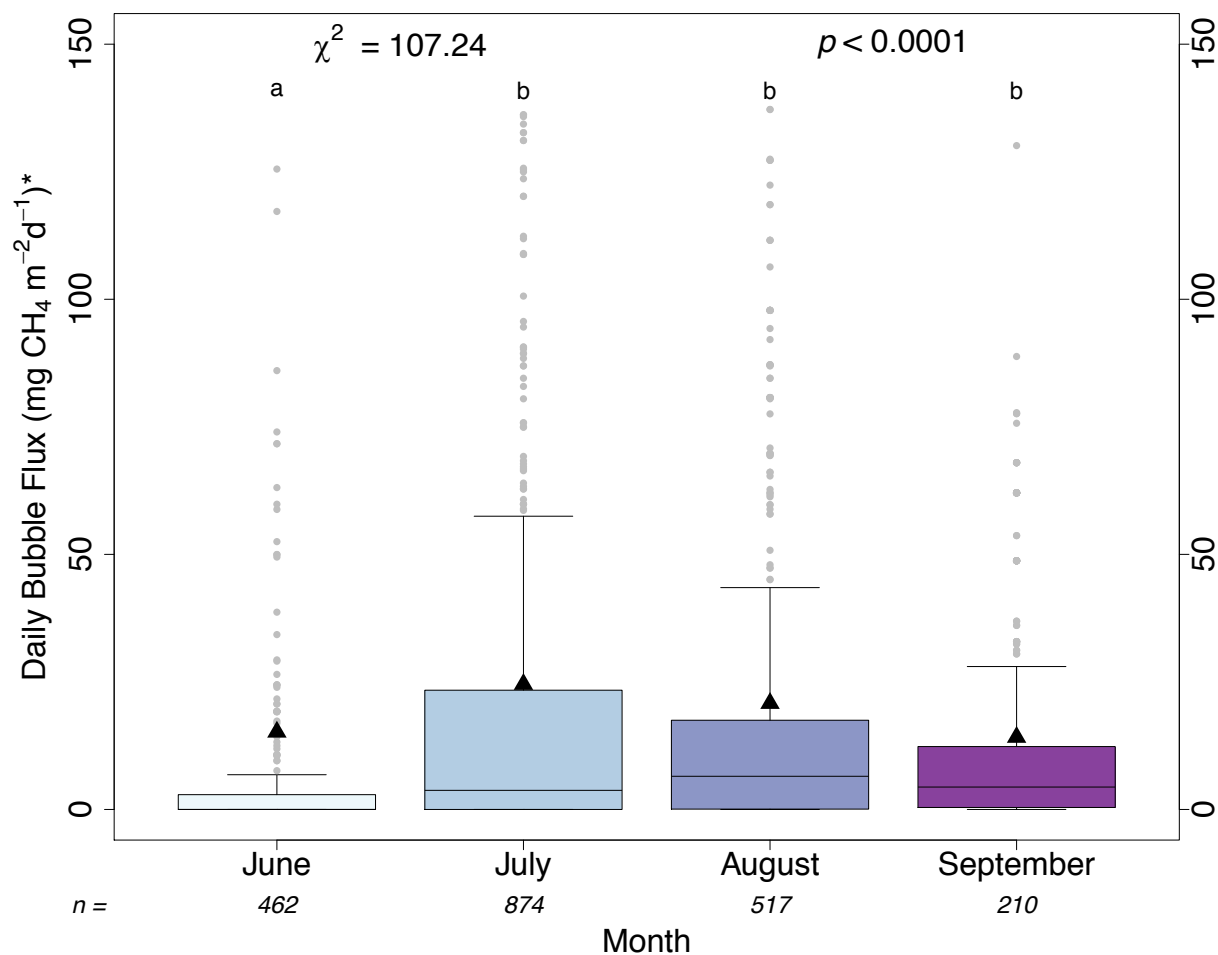


Figure A.5 Boxplot of variability in daily bubble flux ($\text{mg CH}_4 \text{ m}^{-2} \text{ d}^{-1}$) between months. Mean daily ebullitive flux per month is represented as solid black triangles over each box plot. To show true variability in the data, the y axis was plotted between 0 and 150 $\text{mg CH}_4 \text{ m}^{-2} \text{ d}^{-1}$ and outliers larger than 140 $\text{mg CH}_4 \text{ m}^{-2} \text{ d}^{-1}$ were omitted for clarity. Lowercase letters represent pairwise differences between sampling seasons (Dunn's test, $\alpha = 0.05$) and results of the Kruskal-Wallis rank sum test is plotted as χ^2 and p . (Supplementary Figure S5 in Burke et al., 2019).

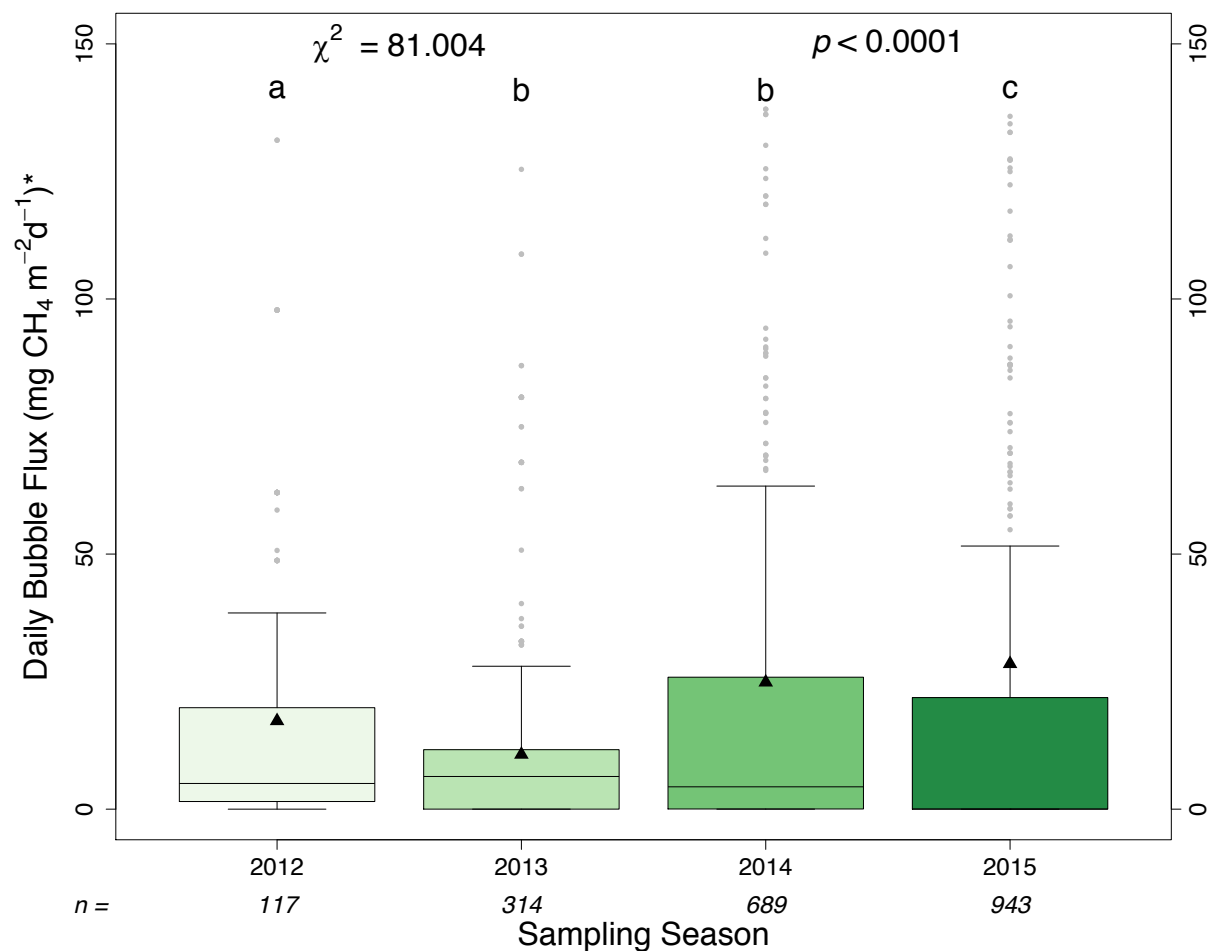


Figure A.6 Boxplot of variability in daily bubble flux (mg CH₄ m⁻² d⁻¹) between sampling seasons. Mean daily ebullitive flux per sampling season is represented as solid black triangles over each box plot. To show true variability in the data, the y axis was plotted between 0 and 150 mg CH₄ m⁻² d⁻¹ and outliers larger than 140 mg CH₄ m⁻² d⁻¹ were omitted for clarity. Lowercase letters represent pairwise differences between sampling seasons (Dunn's test, $\alpha = 0.05$) and results of the Kruskal-Wallis rank sum test is plotted as χ^2 and p . (Supplementary Figure S6 in Burke et al., 2019).

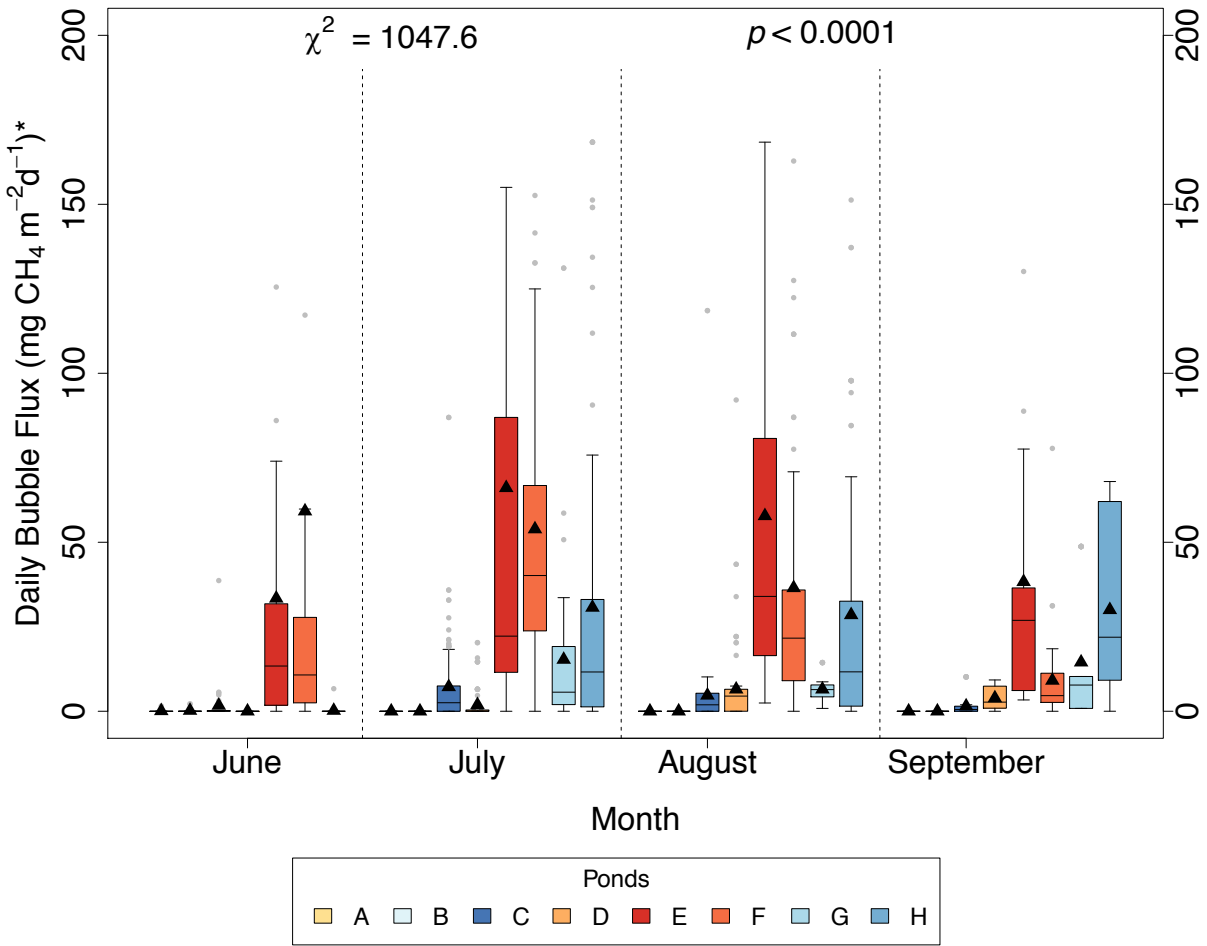


Figure A.7 Boxplot of variability in daily bubble flux ($\text{mg CH}_4 \text{ m}^{-2} \text{ d}^{-1}$) for each pond within months. Small grey circles represent outlier values. Mean daily ebullitive flux of each pond per month is represented as solid black triangles over each box plot. To show true variability in the data, the y axis was plotted between 0 and 200 $\text{mg CH}_4 \text{ m}^{-2} \text{ d}^{-1}$ and outliers larger than 190 $\text{mg CH}_4 \text{ m}^{-2} \text{ d}^{-1}$ were omitted for clarity. Results of the Kruskal-Wallis rank sum test is plotted as χ^2 and p . (Supplementary Figure S7 in Burke et al., 2019).

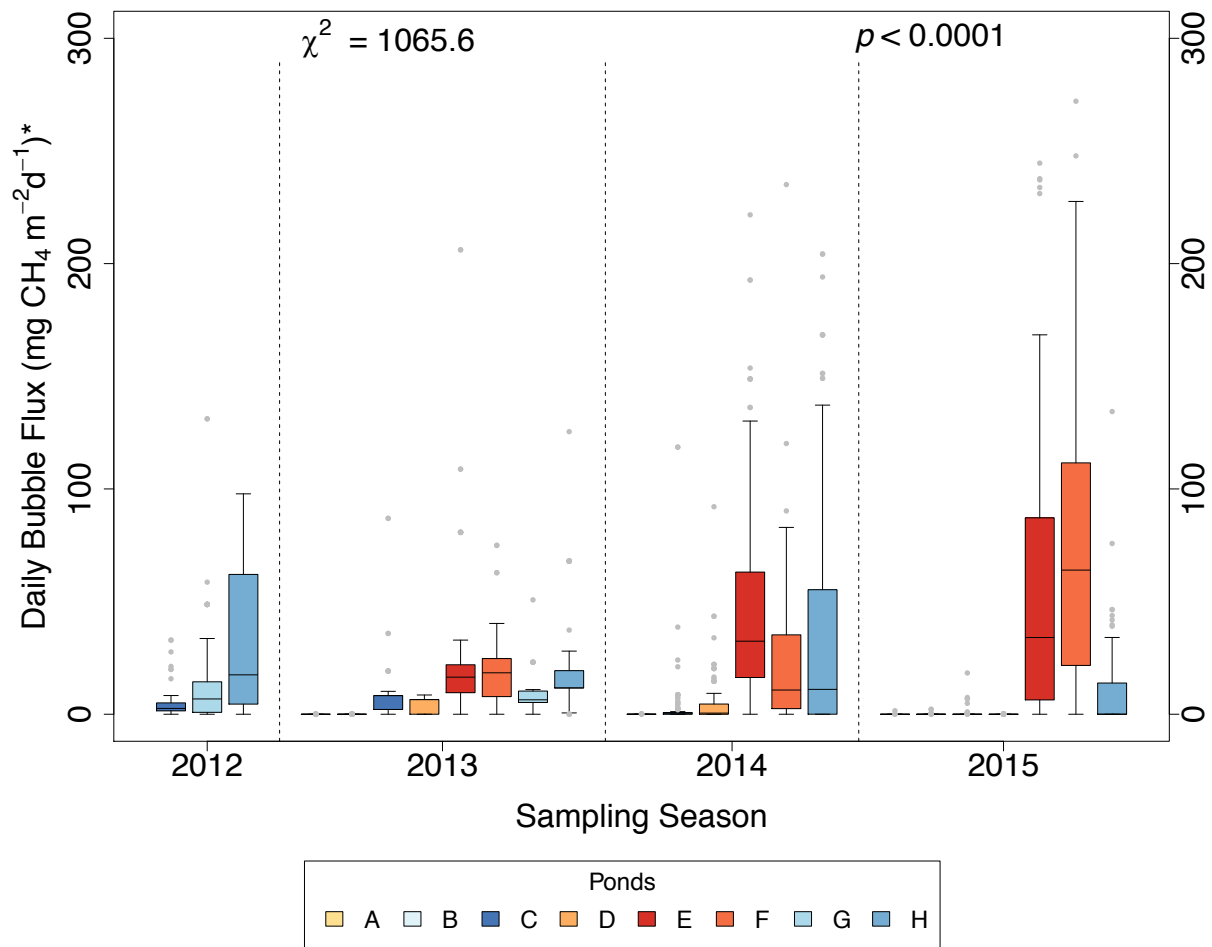


Figure A.8 Boxplot of variability in daily bubble flux ($\text{mg CH}_4 \text{ m}^{-2} \text{ d}^{-1}$) within ponds between sampling seasons. Small grey circles represent outlier values. Mean daily ebullitive flux of each pond per sampling season is represented as solid black triangles over each box plot. To show true variability in the data, the y axis was plotted between 0 and 300 $\text{mg CH}_4 \text{ m}^{-2} \text{ d}^{-1}$ and outliers larger than 290 $\text{mg CH}_4 \text{ m}^{-2} \text{ d}^{-1}$ were omitted for clarity. Results of the Kruskal-Wallis rank sum test is plotted as χ^2 and p . (Supplementary Figure S8 in Burke et al., 2019)

Table A.1 Pond water table depth (WTD, cm) and dissolved oxygen (DO, mg L⁻¹) from 22 July 2013 and from the average of weekly surveys conducted during 2014 field season. In 2013, all ponds were surveyed for WTD. In 2014, all ponds except for G, were measured for WTD and DO. (Supplementary Table S1 in Burke et al., 2019).

Pond	WTD (cm)		[DO] mg L ⁻¹
Year Measured	2013	2014	2014
A	25	19.5	13.28
B	16	20	12.6
C	41	29.2	11.69
D	52	29.5	12.48
E	91	78	12.53
F	34	51	10.67
G	47	-	-
H	47	35.8	13.16

Table A.2 Association between SWR, T_{air}, T_{pond}, and ΔP₅ on ebullitive flux using Kendall's rank correlation test. (Supplementary Table S2 in Burke et al., 2019).

x	y	z	<i>p</i>	<i>τ</i>
SWR	flux	-3.09	0.001	-0.05
T _{air}		5.97	< 0.0001	0.09
T _{pond}		-5.86	< 0.0001	-0.13
ΔP ₅		-3.45	0.0005	-0.05

Table A.3 Pairwise comparisons across months within each pond from a Dunn's Test following the Bonferroni method ($\alpha = 0.05$). Significance of p is indicated by *. (Supplementary Table S3 in Burke et al., 2019).

Pond A			Pond D			Pond G		
		p			p			p
June	July	1	June	July	1	July	August	1
June	August	1	June	August	0.0000*	July	September	1
July	August	1	July	August	0.0059*	August	September	1
June	September	1	June	September	0.0000*			
July	September	1	July	September	0.0085*			
August	September	1	August	September	1			
Pond B			Pond E			Pond H		
June	July	1	June	July	1	June	July	0.0000*
June	August	1	June	August	0.0899	June	August	0.0000*
July	August	1	July	August	1	July	August	1
June	September	1	June	September	1	June	September	0.0000*
July	September	1	July	September	1	July	September	1
August	September	1	August	September	1	August	September	1
Pond C			Pond F					
August	September	1	June	July	0.5507			
July	August	1	June	August	1			
July	September	1	July	August	1			
June	August	0.5703	June	September	1			
June	July	0.0408	July	September	0.0000*			
June	September	1	August	September	0.0968			

Table A.4 Pairwise comparisons across ponds within months from a Dunn's Test following the Bonferroni method ($\alpha = 0.05$). Significance of p is indicated by *. (Supplementary Table S4 in Burke et al., 2019).

June			July			August			September		
		p			p			p			p
Pond E	Pond F	1	Pond E	Pond F	1	Pond E	Pond F	1	Pond E	Pond F	0.2789
Pond E	Pond D	0.0000*	Pond E	Pond D	0.0000*	Pond E	Pond D	0.0000*	Pond E	Pond D	0.0017*
Pond F	Pond D	0.0000*	Pond F	Pond D	0.0000*	Pond F	Pond D	0.0000*	Pond F	Pond D	1
Pond E	Pond A	0.0000*	Pond E	Pond A	0.0000*	Pond E	Pond A	0.0000*	Pond E	Pond A	0.0000*
Pond F	Pond A	0.0000*	Pond F	Pond A	0.0000*	Pond F	Pond A	0.0000*	Pond F	Pond A	0.0015*
Pond D	Pond A	1	Pond D	Pond A	1	Pond D	Pond A	0.0057*	Pond D	Pond A	0.1266
Pond E	Pond B	0.0000*	Pond E	Pond B	0.0000*	Pond E	Pond B	0.0000*	Pond E	Pond B	0.0000*
Pond F	Pond B	0.0000*	Pond F	Pond B	0.0000*	Pond F	Pond B	0.0000*	Pond F	Pond B	0.0033*
Pond D	Pond B	1	Pond D	Pond B	1	Pond D	Pond B	0.0654	Pond D	Pond B	0.2288
Pond A	Pond B	1	Pond A	Pond B	1	Pond A	Pond B	1	Pond A	Pond B	1
Pond E	Pond H	0.0000*	Pond E	Pond G	0.0601	Pond E	Pond G	0.0000*	Pond E	Pond G	1
Pond F	Pond H	0.0000*	Pond F	Pond G	0.0001*	Pond F	Pond G	0.1466	Pond F	Pond G	1
Pond D	Pond H	1	Pond D	Pond G	0.0000*	Pond D	Pond G	1	Pond D	Pond G	1
Pond A	Pond H	1	Pond A	Pond G	0.0000*	Pond A	Pond G	0.0000*	Pond A	Pond G	0.0000*
Pond B	Pond H	1	Pond B	Pond G	0.0000*	Pond B	Pond G	0.0000*	Pond B	Pond G	0.0001*
Pond E	Pond C	0.0000*	Pond E	Pond H	0.6139	Pond E	Pond H	0.0001*	Pond E	Pond H	1
Pond F	Pond C	0.0000*	Pond F	Pond H	0.0005*	Pond F	Pond H	1	Pond F	Pond H	0.0723
Pond D	Pond C	1	Pond D	Pond H	0.0000*	Pond D	Pond H	0.0011*	Pond D	Pond H	0.0001*
Pond A	Pond C	1	Pond A	Pond H	0.0000*	Pond A	Pond H	0.0000*	Pond A	Pond H	0.0000*
Pond B	Pond C	1	Pond B	Pond H	0.0000*	Pond B	Pond H	0.0000*	Pond B	Pond H	0.0000*
Pond H	Pond C	1	Pond G	Pond H	1	Pond G	Pond H	1	Pond G	Pond H	1
			Pond E	Pond C	0.0000*	Pond E	Pond C	0.0000*	Pond E	Pond C	0.0000*
			Pond F	Pond C	0.0000*	Pond F	Pond C	0.0000*	Pond F	Pond C	0.0449
			Pond D	Pond C	0.0197*	Pond D	Pond C	1	Pond D	Pond C	1
			Pond A	Pond C	0.0107*	Pond A	Pond C	0.2206	Pond A	Pond C	1
			Pond B	Pond C	0.0003*	Pond B	Pond C	1	Pond B	Pond C	1
			Pond G	Pond C	1	Pond G	Pond C	0.0075*	Pond G	Pond C	0.0008*
			Pond H	Pond C	0.0001*	Pond H	Pond C	0.0000*	Pond H	Pond C	0.0000*

Table A.5 Pairwise comparisons across sampling seasons within ponds from a Dunn's Test following the Bonferroni method ($\alpha = 0.05$). Significance of p is indicated by *. (Supplementary Table S5 in Burke et al., 2019).

Pond A			Pond E		
		p			p
2013	2015	1	2013	2014	1
			2013	2015	1
			2014	2015	1
Pond B			Pond F		
2013	2014	1	2013	2014	1
2013	2015	1	2013	2015	0.58
2014	2015	1	2014	2015	0.0015*
Pond C			Pond G		
2012	2013	1	2012	2013	1
2012	2014	0.0407			
2013	2014	0.0000*	Pond H		
2012	2015	0.0000*	2012	2013	1
2013	2015	0.0000*	2012	2014	1
2014	2015	0.658	2013	2014	1
Pond D			2012	2015	0.0000*
2013	2014	1	2013	2015	0.0000*
2013	2015	0.0000*	2014	2015	0.0000*
2014	2015	0.0000*			

Table A.6 Pairwise comparisons across ponds within sampling seasons from a Dunn's Test following the Bonferroni method ($\alpha = 0.05$). Significance of p is indicated by *. (Supplementary Table S6 in Burke et al., 2019).

2012			2013			2014			2015		
		p			p			p			p
Pond G	Pond C	0.8399	Pond A	Pond B	1	Pond B	Pond C	1	Pond A	Pond B	1
Pond G	Pond H	0.4718	Pond A	Pond C	0.0000*	Pond B	Pond H	0.0000*	Pond A	Pond C	1
Pond H	Pond C	0.0000*	Pond A	Pond G	0.0000*	Pond D	Pond B	0.4499	Pond A	Pond H	0.7458
			Pond A	Pond H	0.0000*	Pond D	Pond C	1	Pond B	Pond C	1
			Pond B	Pond C	0.0000*	Pond D	Pond H	0.0001*	Pond B	Pond H	0.0223*
			Pond B	Pond G	0.0000*	Pond E	Pond B	0.0000*	Pond D	Pond A	1
			Pond B	Pond H	0.0000*	Pond E	Pond C	0.0000*	Pond D	Pond B	1
			Pond D	Pond A	0.0000*	Pond E	Pond D	0.0000*	Pond D	Pond C	1
			Pond D	Pond B	0.0010*	Pond E	Pond F	0.0090*	Pond D	Pond H	0.0001*
			Pond D	Pond C	1	Pond E	Pond H	0.0006*	Pond E	Pond A	0.0000*
			Pond D	Pond G	1	Pond F	Pond B	0.0000*	Pond E	Pond B	0.0000*
			Pond D	Pond H	0.0000*	Pond F	Pond C	0.0000*	Pond E	Pond C	0.0000*
			Pond E	Pond A	0.0000*	Pond F	Pond D	0.0000*	Pond E	Pond D	0.0000*
			Pond E	Pond B	0.0000*	Pond F	Pond H	1	Pond E	Pond F	1
			Pond E	Pond C	0.0418	Pond H	Pond C	0.0000*	Pond E	Pond H	0.0000*
			Pond E	Pond D	0.0000*				Pond F	Pond A	0.0000*
			Pond E	Pond F	1				Pond F	Pond B	0.0000*
			Pond E	Pond G	0.0696				Pond F	Pond C	0.0000*
			Pond E	Pond H	1				Pond F	Pond D	0.0000*
			Pond F	Pond A	0.0000*				Pond F	Pond H	0.0000*
			Pond F	Pond B	0.0000*				Pond H	Pond C	0.0075*
			Pond F	Pond C	0.1424						
			Pond F	Pond D	0.0000*						
			Pond F	Pond G	0.2291						
			Pond F	Pond H	1						
			Pond G	Pond C	1						
			Pond G	Pond H	0.4317						
			Pond H	Pond C	0.2745						

APPENDIX B: CHAPTER 2 SUPPLEMENTARY MATERIALS

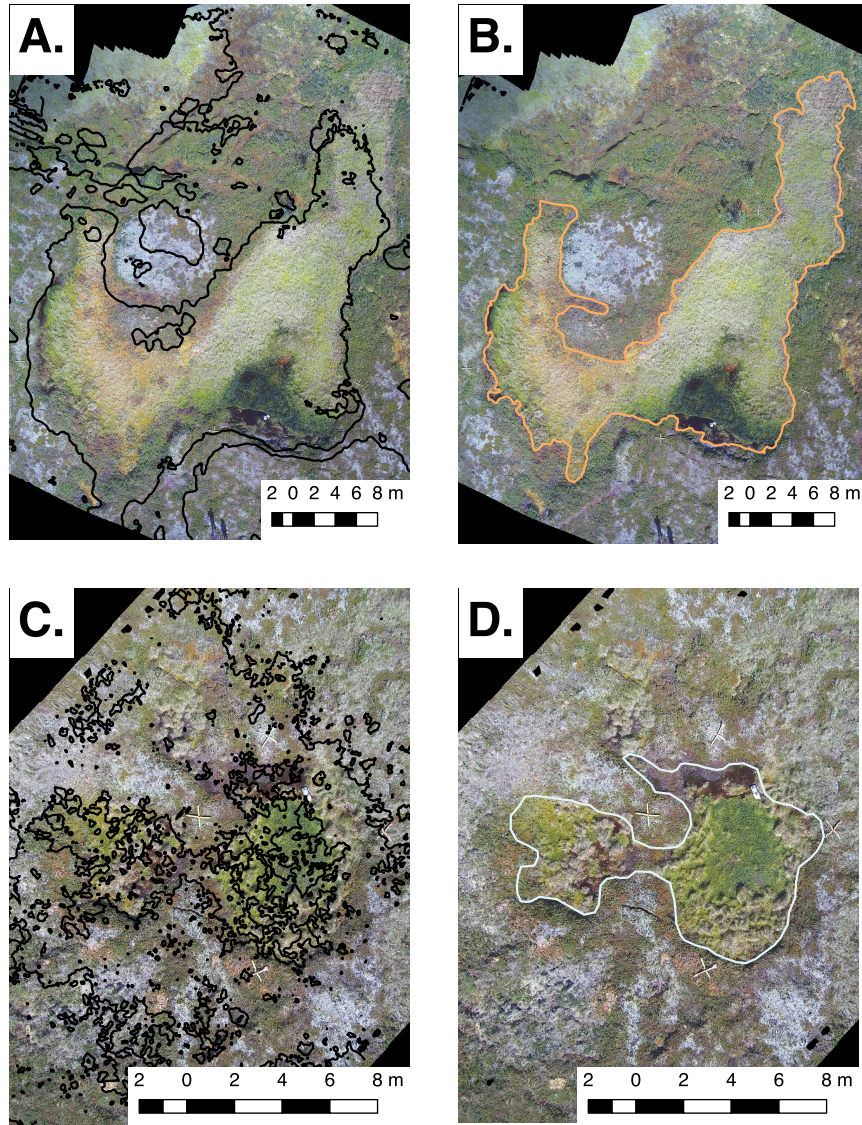


Figure B.1 Comparison of Contour line delineation of ponds using digital elevation models created using AgiSoft Photoscan. A.) Orthomosaic of Pond D showing 1m contour lines in black. B.) the hand-drawn delineation of the pond edge of Pond D. C) Orthomosaic of Pond B showing 1m contour lines in black. D.) the hand drawn delineation of the pond edge of Pond B.

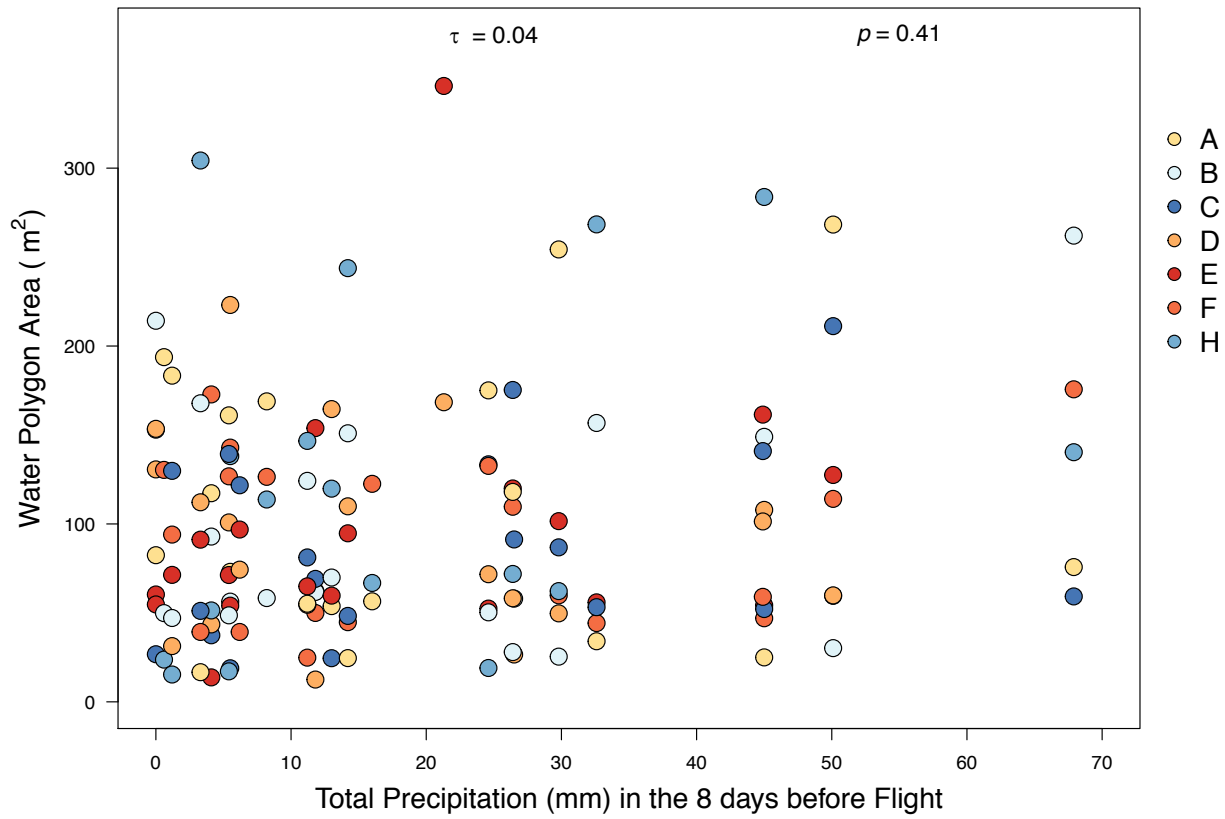


Figure B.2 Water polygon area (m²) of each pond in the study compared to the total precipitation accumulation (mm) in the eight days leading up to the UAS flight. Only quadcopter imagery is represented. Colors represent different ponds.

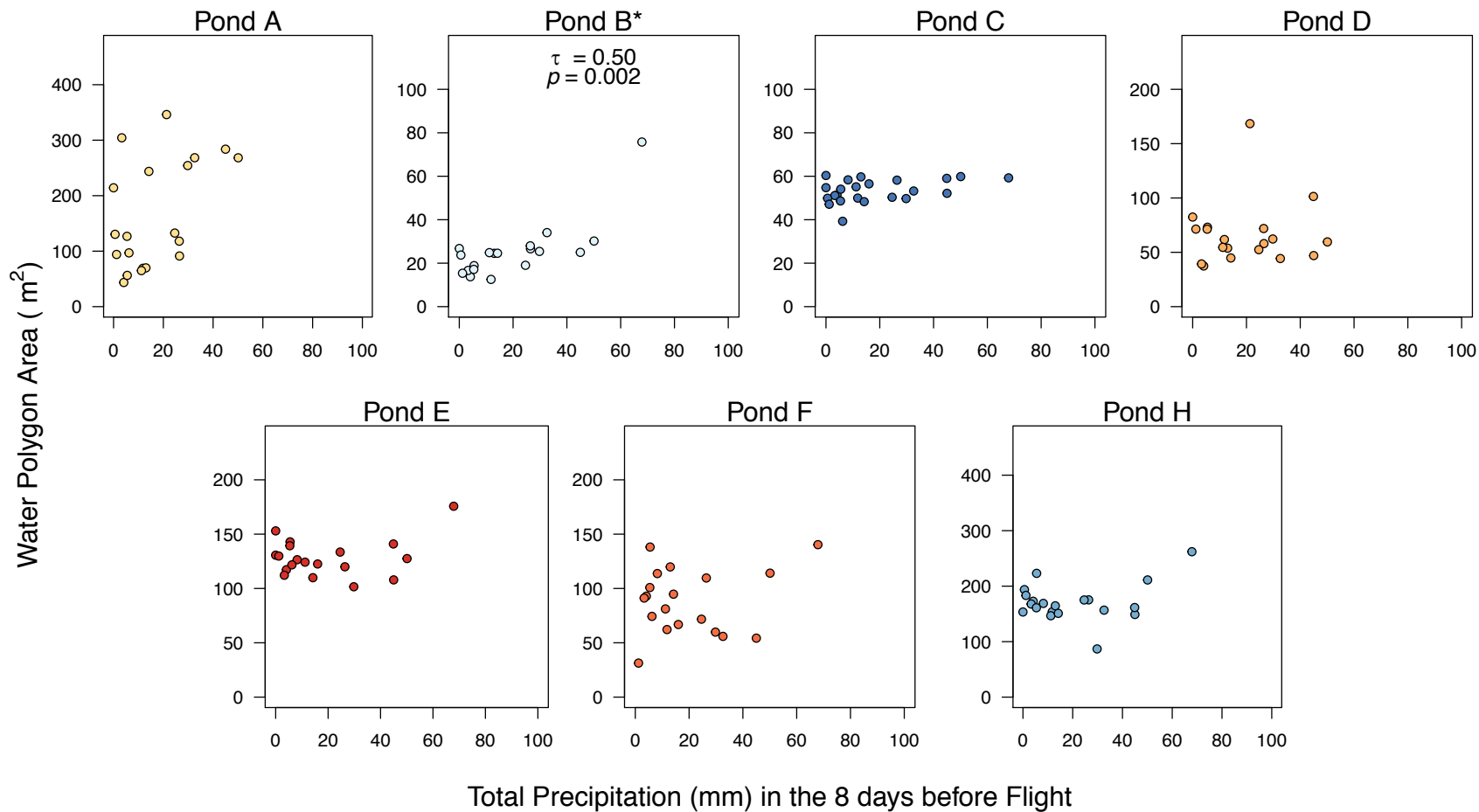


Figure B.3 Relationship between water polygon area and total precipitation accumulation before flight separated by pond. Ponds with significant relationships have * by their name. Significant results of nonparametric Kendall correlations are displayed as τ and p values.

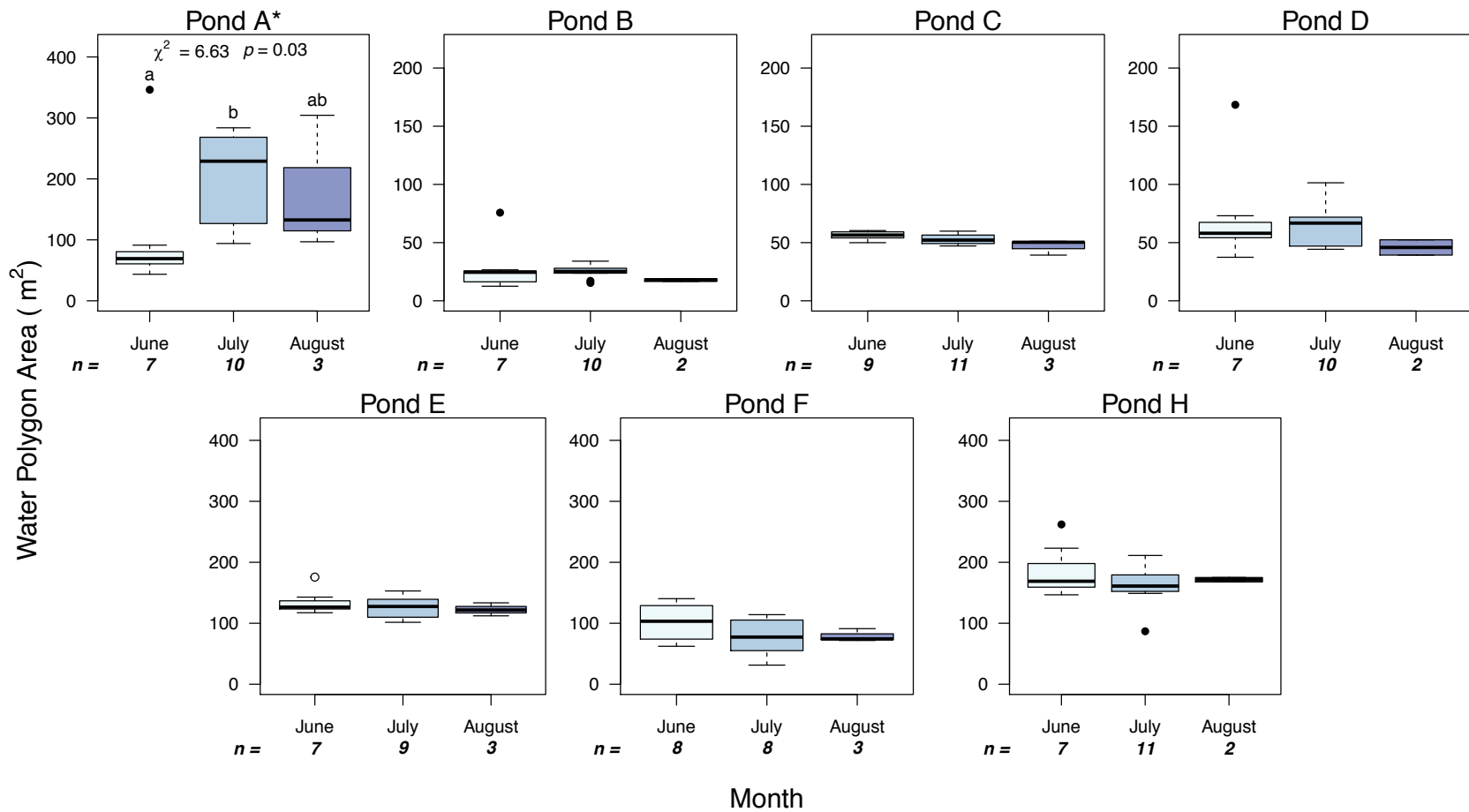


Figure B.4 Water Polygon area of quadcopter imagery collected during the growing season at Stordalen Mire during the 2016, 2017 and 2018 growing seasons, separated by month. Ponds with significant differences found between months are marked with a *. The lowercase letters indicate significant pairwise differences between months. The results of a Kruskal Wallis rank sums test are displayed as χ^2 and p values.

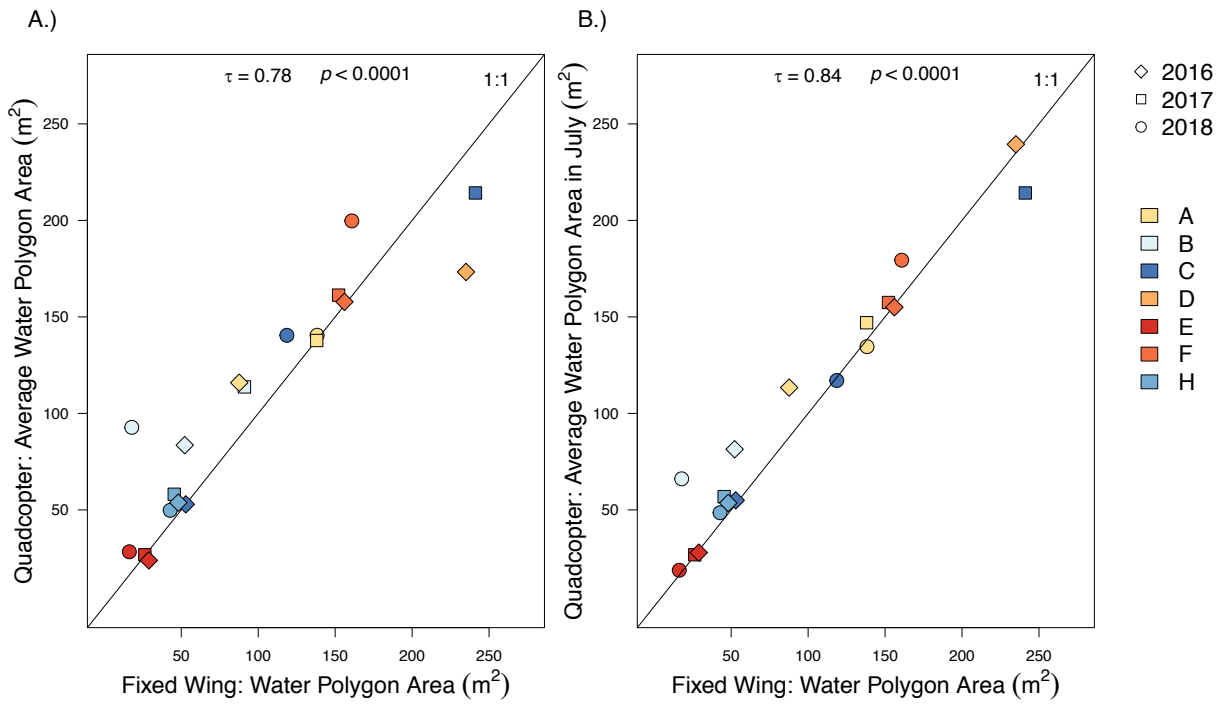


Figure B.5 Comparison of water polygon area measured from fixed wing imagery collected in July compared to the average water polygon area measured from quadcopter imagery collected throughout the growing season (A.) or only in July (B.). different symbols represent different sampling seasons, while different colors represent different ponds. Results of a Kendall correlation test is presented as τ and p values.

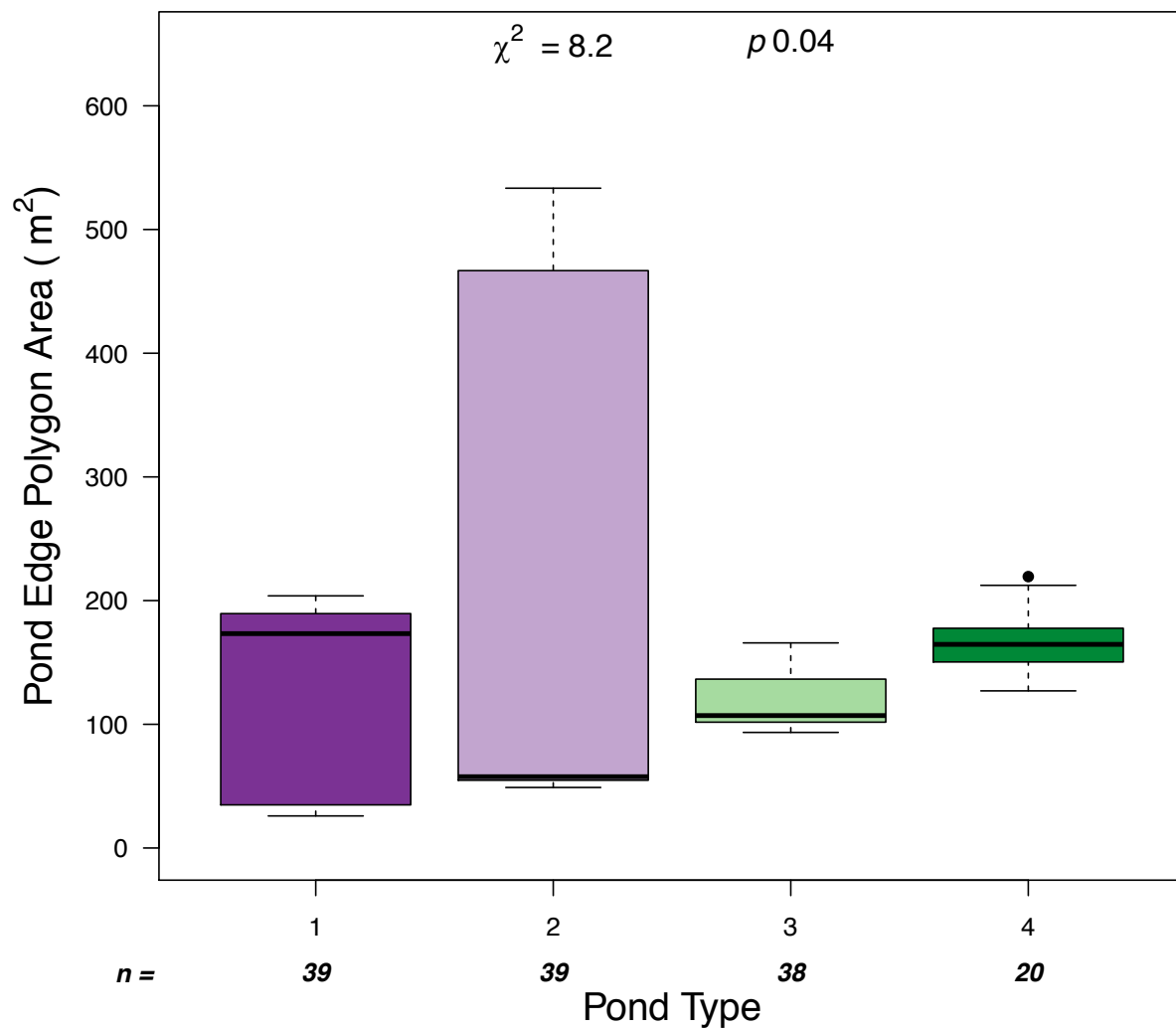


Figure B.6 Pond edge polygon area from quadcopter imagery among the different pond types. Solid black lines represent median values and solid black dots represent outliers. N values below each pond type represent the number of images included in each boxplot. The results of a Kruskal Wallis rank sums test are displayed as χ^2 and p values.

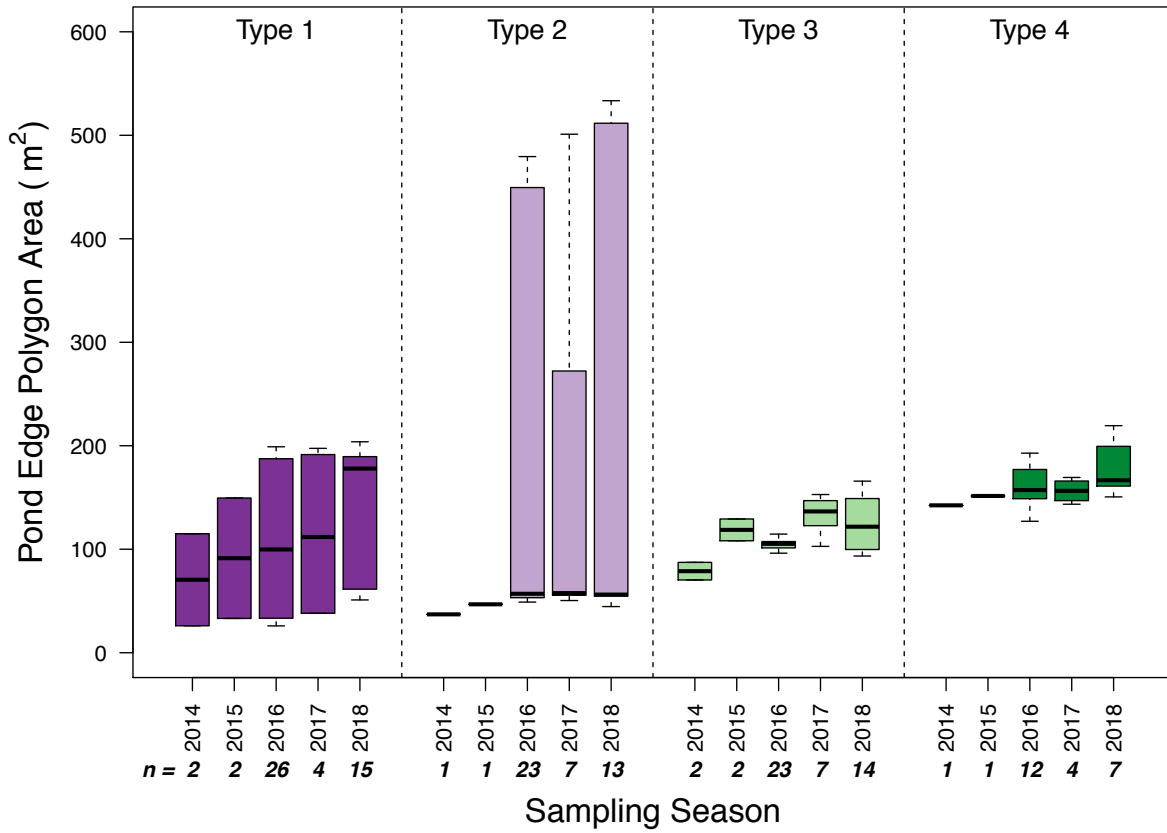


Figure B.7 Pond edge area of differing pond types by sampling season from imagery collected using the quadcopter UAS and fixed wing airplane. Black lines represent median values. N values represent the number of images included in each boxplot.

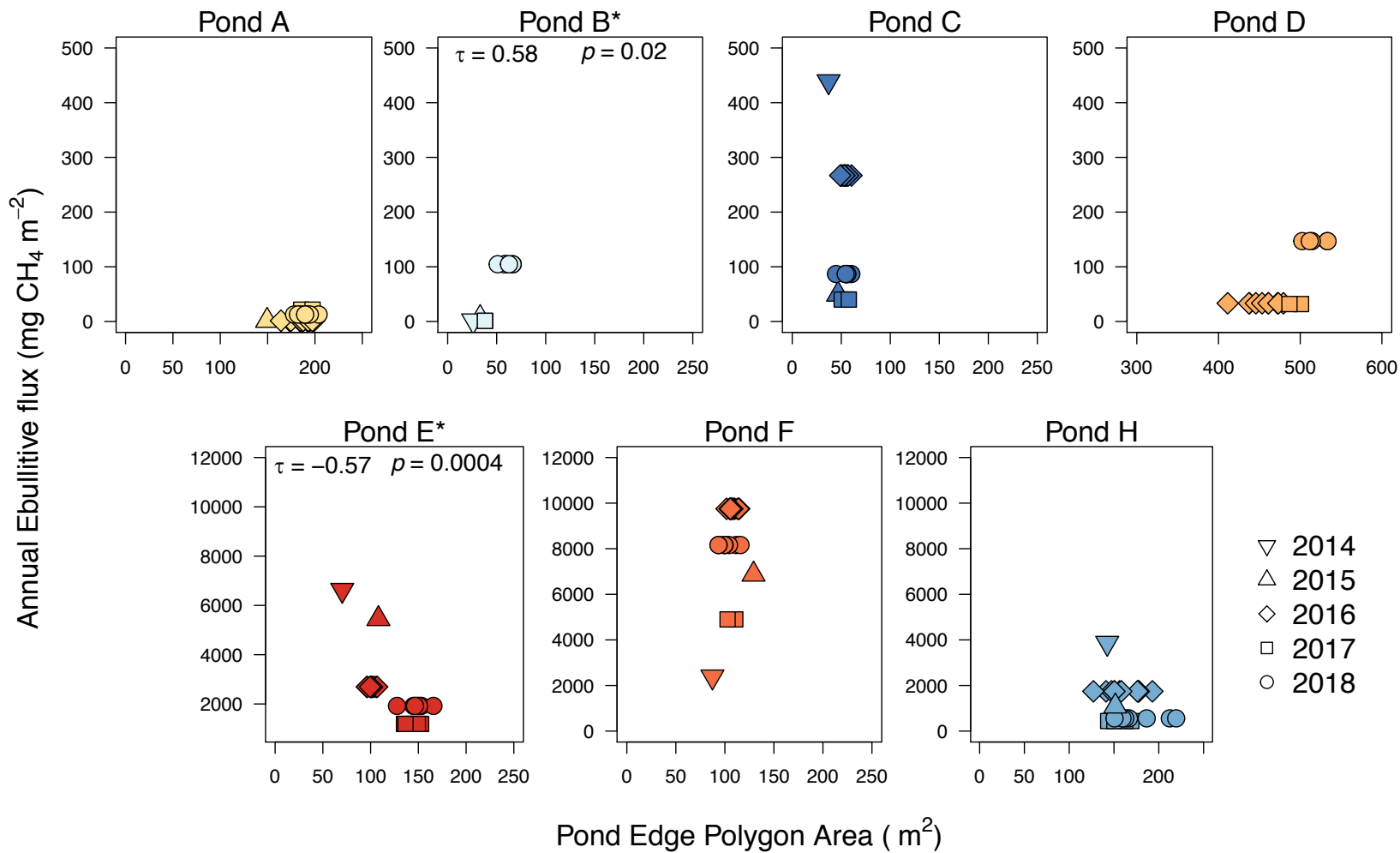


Figure B.8 Annual ebullitive flux (mg CH₄ m⁻²) compared to pond edge area (m²) from both quadcopter and fixed wing imagery of the seven ponds in this study. The different colors represent the different ponds and the different shapes represent differing sampling seasons. Ponds that show a significant relationship have a * by their name. Significant results of a Kendall correlation test are presented as τ and p values.

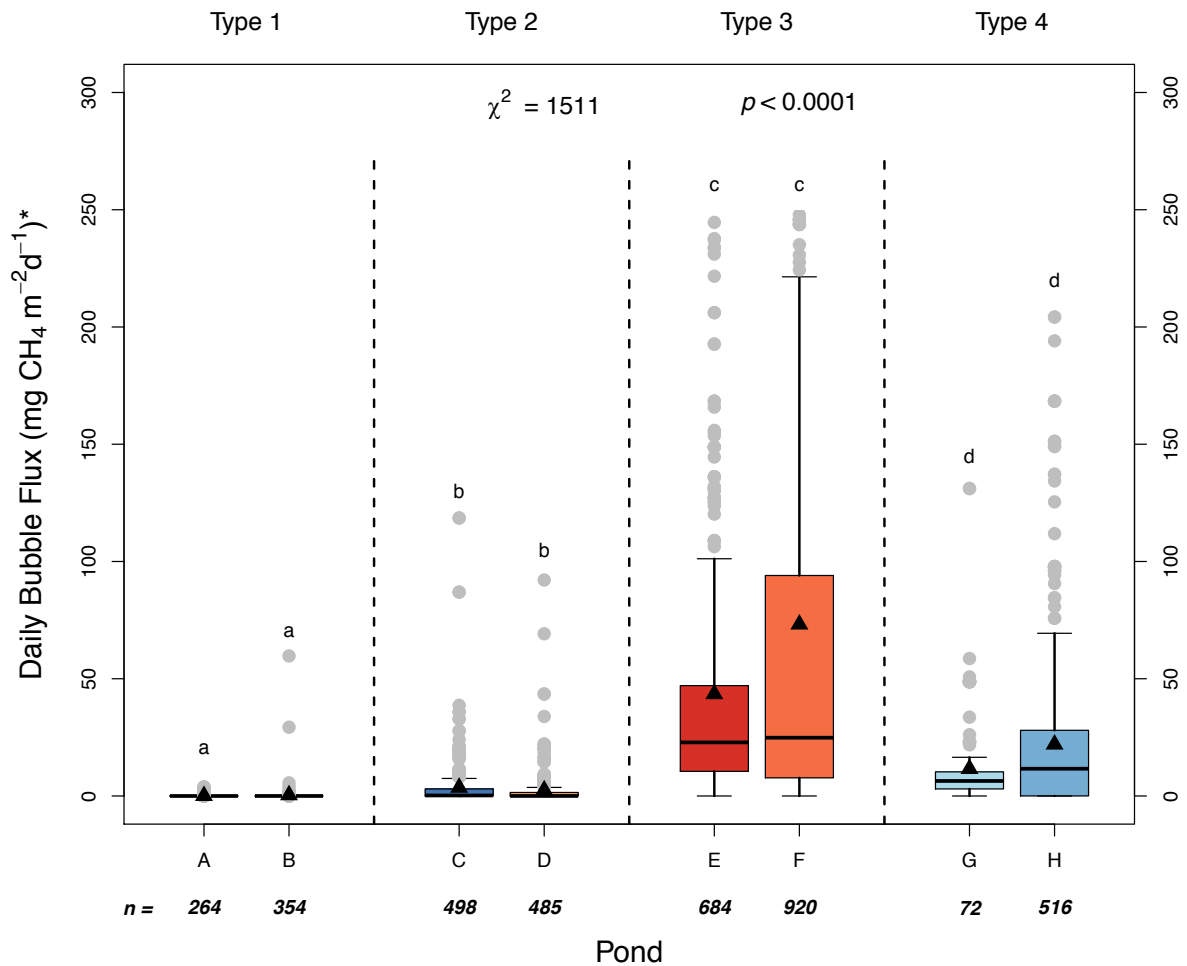


Figure B.9 Updated boxplots from Burke et al. (2019) to include all of the ebullitive measurements collected between 2012-2018 represented as daily bubble flux (mg CH₄ · m⁻² · day⁻¹). The different colors are used to distinguish ponds from each other. To show the real distribution of the data, the y axis was plotted between 0 and 300 mg CH₄ · m⁻² · day⁻¹, with outliers greater than 250 mg CH₄ · m⁻² · day⁻¹ omitted from this figure (n = 32). The number of measurements collected at each pond over the study period are in bold italics below each pond label. Solid triangles represent the mean daily bubble flux of each pond across the study period. Dark lines across each box represent median values, and small gray circles represent outliers. Lowercase letters represent significant differences between ponds. Results of the Kruskal-Wallis rank sum test noted as χ^2 and p . Ponds are divided up into types 1 to 4 based on their statistically different fluxes, and these types appear to correspond to physical differences (depth, vegetation presence, and hydrology; see Table 1.1 in Burke et al. 2019).

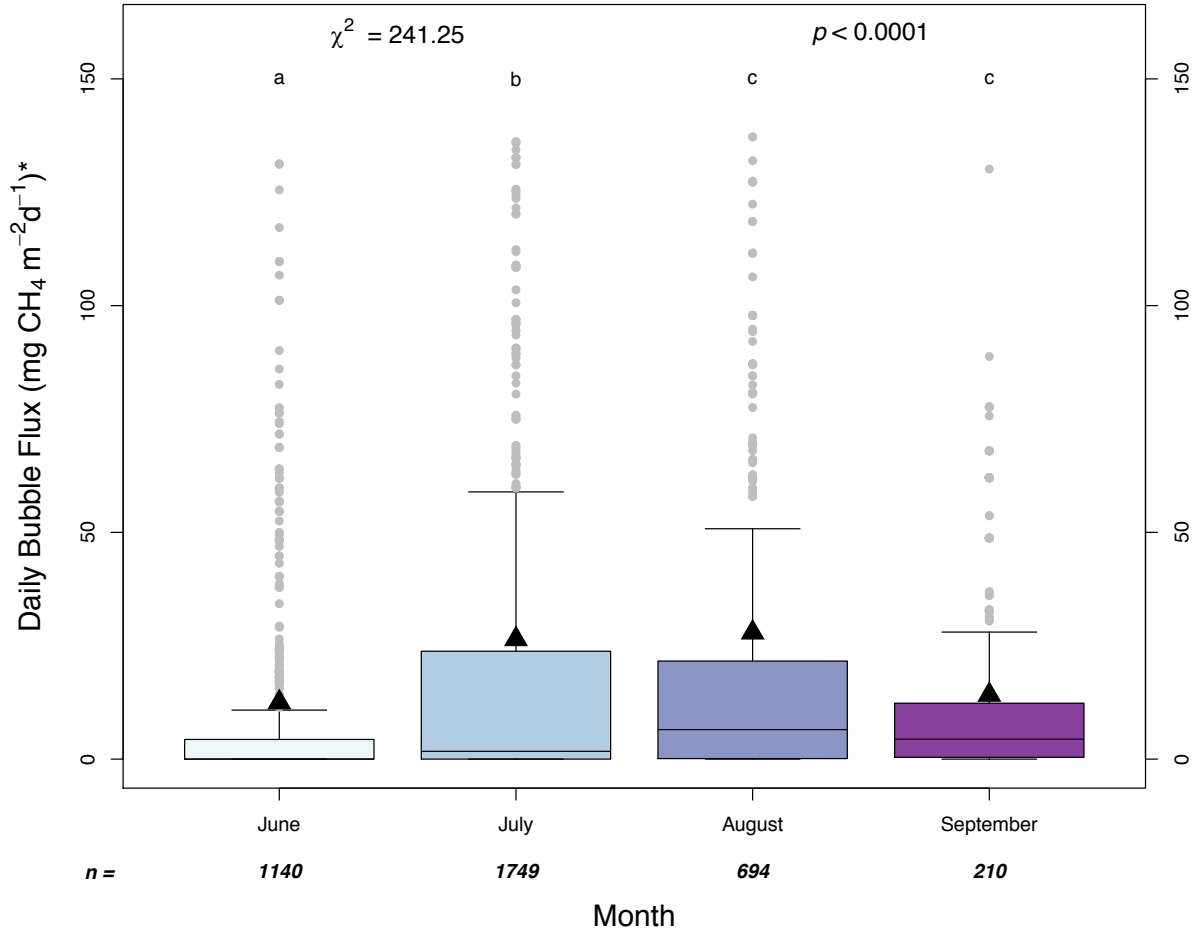


Figure B.10 Updated boxplots from Burke et al. (2019) of variability in daily bubble flux (mg CH₄ m⁻² d⁻¹) between months collected 2012-2018 sampling seasons. Mean daily ebullitive flux per month is represented as solid black triangles over each box plot. To show true variability in the data, the y axis was plotted between 0 and 150 mg CH₄ m⁻² d⁻¹ and outliers larger than 140 mg CH₄ m⁻² d⁻¹ were omitted for clarity (n = 126). Lowercase letters represent pairwise differences between sampling seasons (Dunn's test, $\alpha = 0.05$) and results of the Kruskal-Wallis rank sum test is plotted as χ^2 and p.

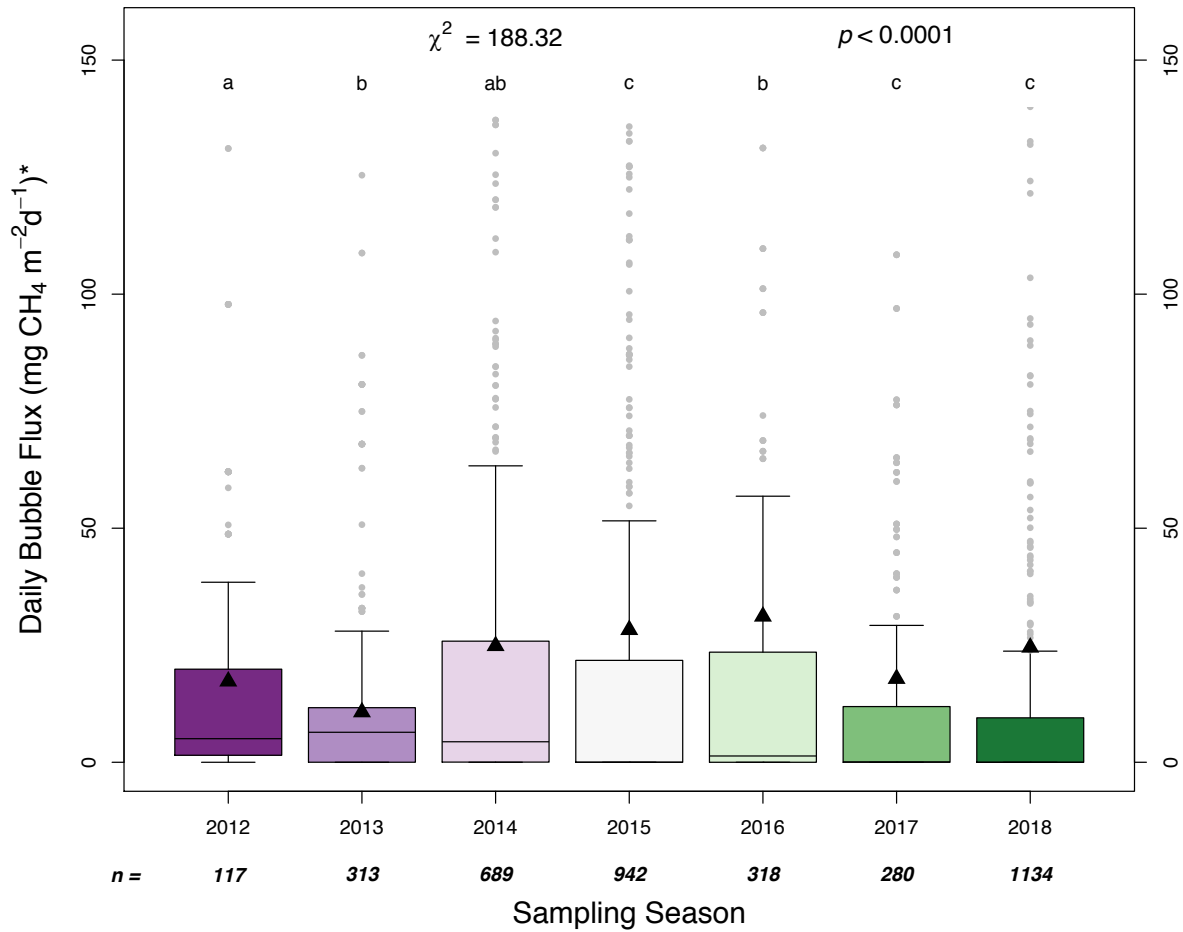


Figure B.11 Updated boxplots from Burke et al. (2019) showing the variability in daily bubble flux ($\text{mg CH}_4 \text{ m}^{-2} \text{ d}^{-1}$) between sampling seasons. Mean daily ebullitive flux per sampling season is represented as solid black triangles over each box plot. To show true variability in the data, the y axis was plotted between 0 and 150 $\text{mg CH}_4 \text{ m}^{-2} \text{ d}^{-1}$ and outliers larger than 140 $\text{mg CH}_4 \text{ m}^{-2} \text{ d}^{-1}$ were omitted for clarity ($n = 126$). Lowercase letters represent pairwise differences between sampling seasons (Dunn's test, $\alpha = 0.05$) and results of the Kruskal-Wallis rank sum test is plotted as χ^2 and p .

Table B.1 Table of mean tie point residuals for each image collected with the quadcopter during the 2016,2017 and 2018 field seasons. Bolded values denote which image from each year was considered the ‘Best of’ image, to which all other images of the same pond from that sampling season were georeferenced to. Italicized values show images that had a lower mean than the ‘Best of’ image, but these images were either distorted in the orthorectification process or were incomplete coverage of the pond.

Pond	Year	Flight Date	Mean of Tie Point Residuals	Pond	Year	Flight Date	Mean of Tie Point Residuals	Pond	Year	Flight Date	Mean of Tie Point Residuals	Pond	Year	Flight Date	Mean of Tie Point Residuals	
A	2016	12-Jun	3.694	C	2016	12-Jun	11.204	E	2016	12-Jun	3.644	H	2016	12-Jun	6.836	
		15-Jun	0.305			15-Jun	2.403			24-Jun	0.722			15-Jun	2.530	
		17-Jun	1.087			17-Jun	1.872			26-Jun	3.206			17-Jun	2.851	
		26-Jun	2.368			24-Jun	1.554			3-Jul	2.540			26-Jun	3.173	
		29-Jun	1.891			26-Jun	5.254			6-Jul	3.257			3-Jul	19.537	
		3-Jul	1.025			3-Jul	5.752			12-Jul	10.529			6-Jul	2.291	
		6-Jul	1.188			6-Jul	1.383			24-Jul	3.542			12-Jul	3.148	
		12-Jul	1.887			12-Jul	2.833			30-Jul	7.465			19-Jul	4.283	
		19-Jul	1.673			19-Jul	3.251			22-Aug	3.356			24-Jul	2.715	
		24-Jul	2.728			24-Jul	7.369			13-Jun	3.566			30-Jul	5.970	
	30-Jul	2.228	30-Jul		5.199	30-Jun	7.683		22-Aug	1.926						
	22-Aug	1.457	22-Aug		1.154	21-Jul	7.479		30-Jun	18.132						
	2017	26-Jul	3.078		2017	13-Jun	1.279		26-Jul	6.541	2017		21-Jul	12.522		
	2018	17-Jun	4.363		2017	30-Jun	7.510		17-Jun	1.316	26-Jul		15.566			
28-Jun		2.214	26-Jul	21-Jul	1.212	25-Jun	3.328	17-Jun	14.041							
5-Jul		3.325	17-Jun	3.299	11-Jul	5.147	25-Jun	19.159								
11-Jul		3.795	25-Jun	4.190	17-Jul	5.678	5-Jul	20.963								
17-Jul		2.130	5-Jul	2.733	1-Aug	4.595	11-Jul	19.192								
1-Aug		4.346	11-Jul	5.702	8-Aug	2.962	17-Jul	14.145								
8-Aug		3.529	17-Jul	1.172	12-Jun	17.656	1-Aug	11.845								
12-Jun		1.726	1-Aug	2.983	15-Jun	2.612										
B	2016	15-Jun	1.019	D	2016	17-Jun	8.077	F	2016	17-Jun	3.582		2016	17-Jun	3.582	
		17-Jun	0.727			24-Jun	6.522			24-Jun	6.522			26-Jun	3.483	
		26-Jun	2.161			26-Jun	10.975			26-Jun	3.483			3-Jul	3.045	
		29-Jun	1.907			15-Jun	22.039			3-Jul	3.045			6-Jul	1.794	
		3-Jul	1.719			17-Jun	7.422			6-Jul	1.794			12-Jul	3.756	
		6-Jul	1.981			26-Jun	12.129			12-Jul	3.756			19-Jul	3.088	
		12-Jul	2.162			29-Jun	11.134			19-Jul	3.088			24-Jul	7.072	
		19-Jul	1.942			3-Jul	11.450			24-Jul	7.072			30-Jul	5.780	
		24-Jul	0.889			6-Jul	13.917			22-Aug	1.712			2017	30-Jun	6.011
		30-Jul	0.423			12-Jul	13.883			17-Jun	2.975			17-Jun	2.975	
	22-Aug	2.104	19-Jul		16.155	25-Jun	2.425		25-Jun	2.425						
	2017	26-Jul	2.705		24-Jul	14.928	11-Jul		4.302	11-Jul	4.302					
	2018	17-Jun	2.248		30-Jul	14.760	17-Jul		2.954	17-Jul	2.954					
		25-Jun	2.401		22-Aug	9.075	1-Aug		5.020	1-Aug	5.020					
5-Jul		2.164	2017	21-Jul	3.753	8-Aug	0.717									
11-Jul		2.573	26-Jul	5.851												
17-Jul	1.176	17-Jun	4.023													
1-Aug	1.215	28-Jun	2.319													
		2018	11-Jul	10.155												
			17-Jul	11.917												
			<i>1-Aug</i>	<i>1.491</i>												

Table B.2 Monthly summary of meteorological variables for 2016 - 2018.

Data	June	July	August
P (mm)	50.6	89.1	59
Tair (°C)	7.77	12.9	10.44
SWR (W m-2)	200.2	187.4	119.4

Note: Total precipitation (mm), average air temperature (°C), and average shortwave radiation (W m-2) were calculated using data collected at Stordalen Mire by ICOS-Sweden, using their WeatherHawk system.

APPENDIX C: CHAPTER 3 SUPPLEMENTARY MATERIALS

Note: Plots for Appendix C continue on the next page.

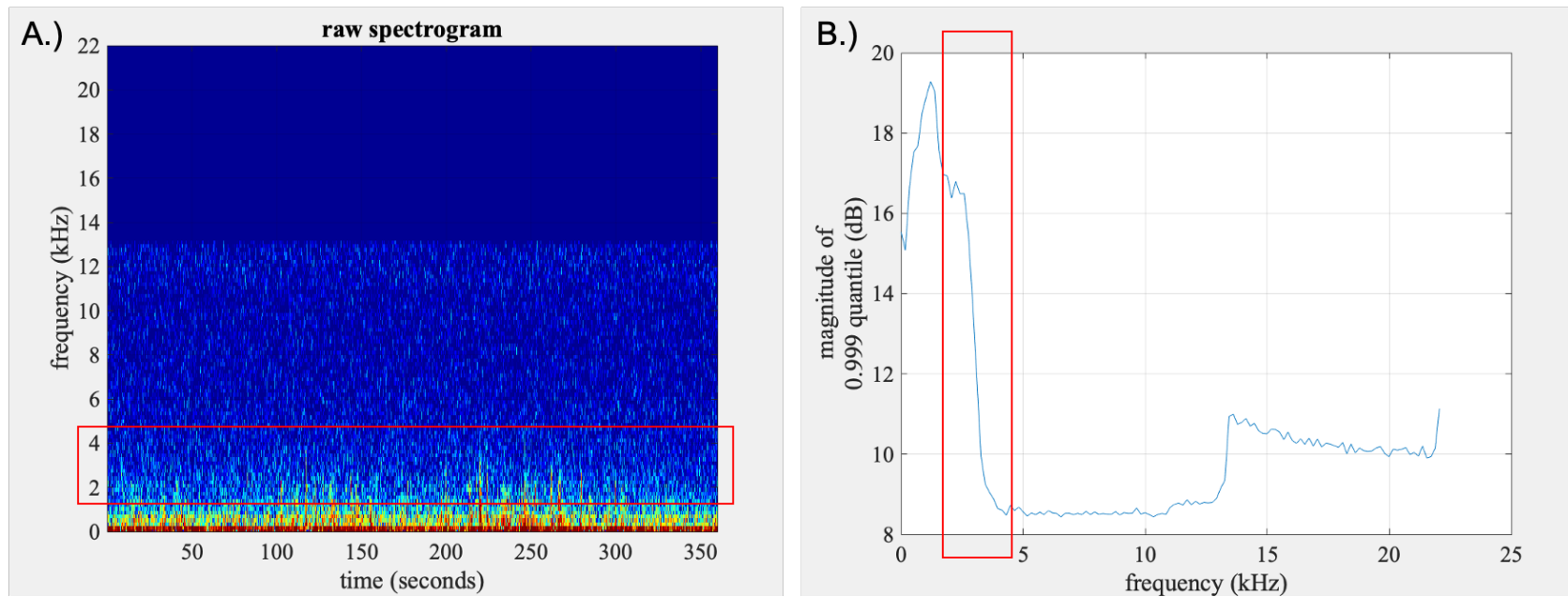


Figure C.1 MATLAB spectrogram of the raw data (A.) and the magnitude of the 99th quantile (dB) (B.) from a six-minute acoustic file showing the energy is concentrated in the lower frequencies. The red rectangles in both subplots represents the filtering window of 1500 – 4500 Hz used to focus the MATLAB processing on the portion of the acoustic data where most of the acoustic energy is focused. Note: Energy concentration in spectrograms vary between files.

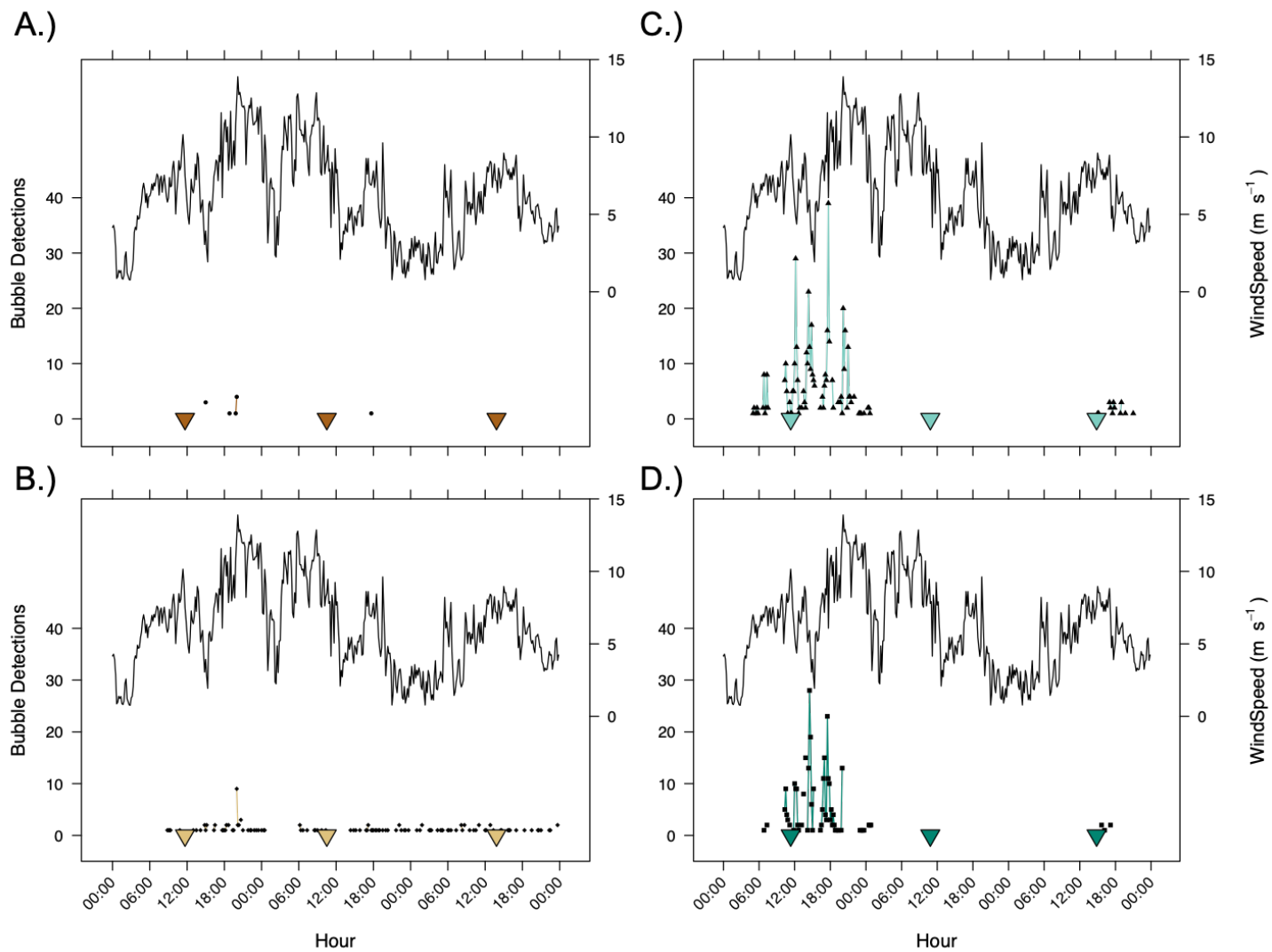


Figure C.2 Time series of bubble detected on a ten-minute timescale between 14 June and 16 June, 2018 in traps C1 and C2 (panels A. & B.), C.) trap H1 and D.) trap H2, distinguished from each other by color and symbol. Measured wind speed (m s⁻¹) is represented in each subplot as a solid black line. The volume of gas collected during this time period is represented in each subplot by the color-coded inverted triangles.

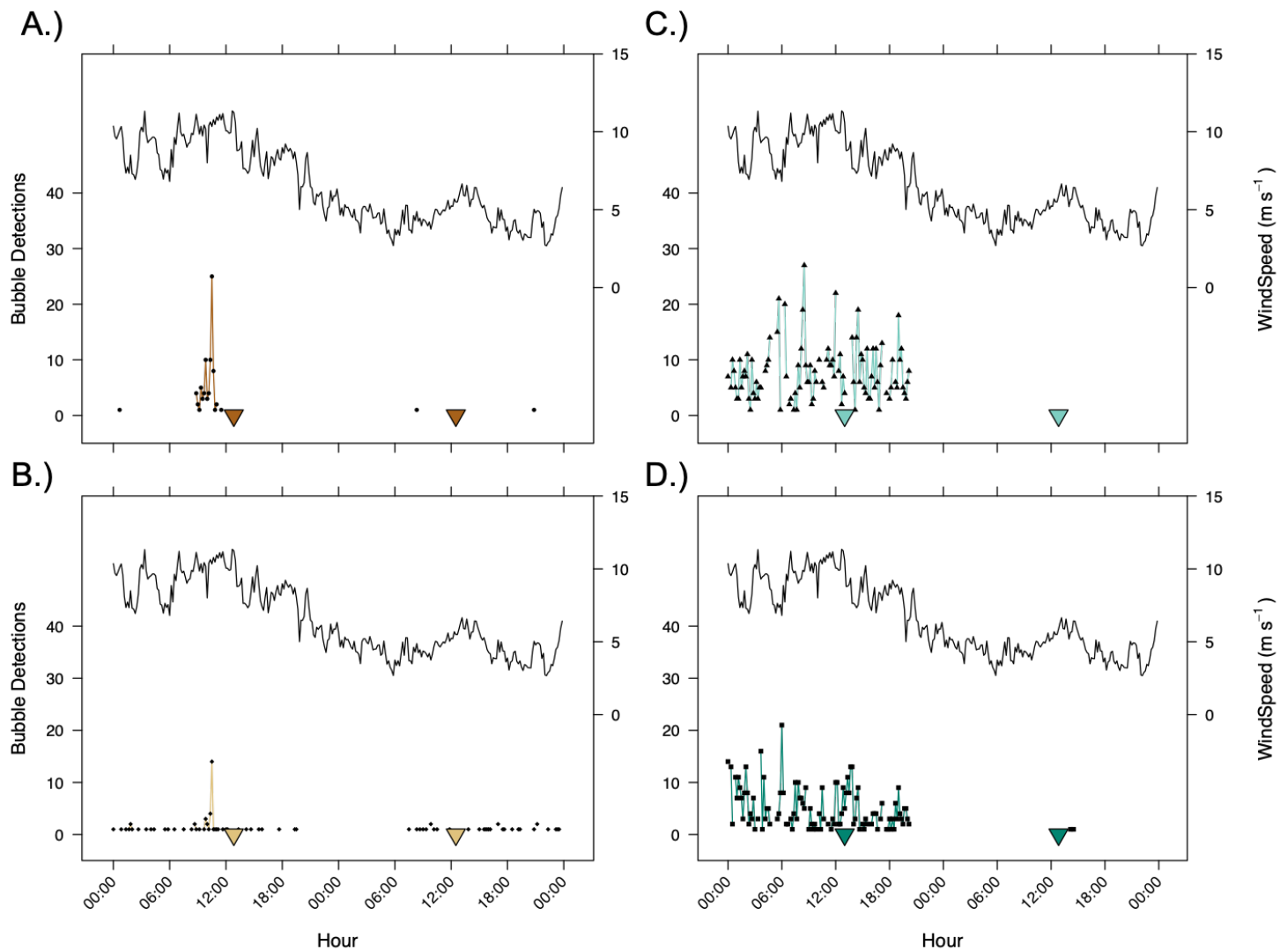


Figure C.3 Time series of bubble detected on a ten-minute timescale between 27 June and 29, June, 2018 in traps C1 and C2 (panels A. & B.), C.) trap H1 and D.) trap H2, distinguished from each other by color and symbol. Measured wind speed (m s^{-1}) is represented in each subplot as a solid black line. The volume of gas collected during this time period is represented in each subplot by the color-coded inverted triangles.

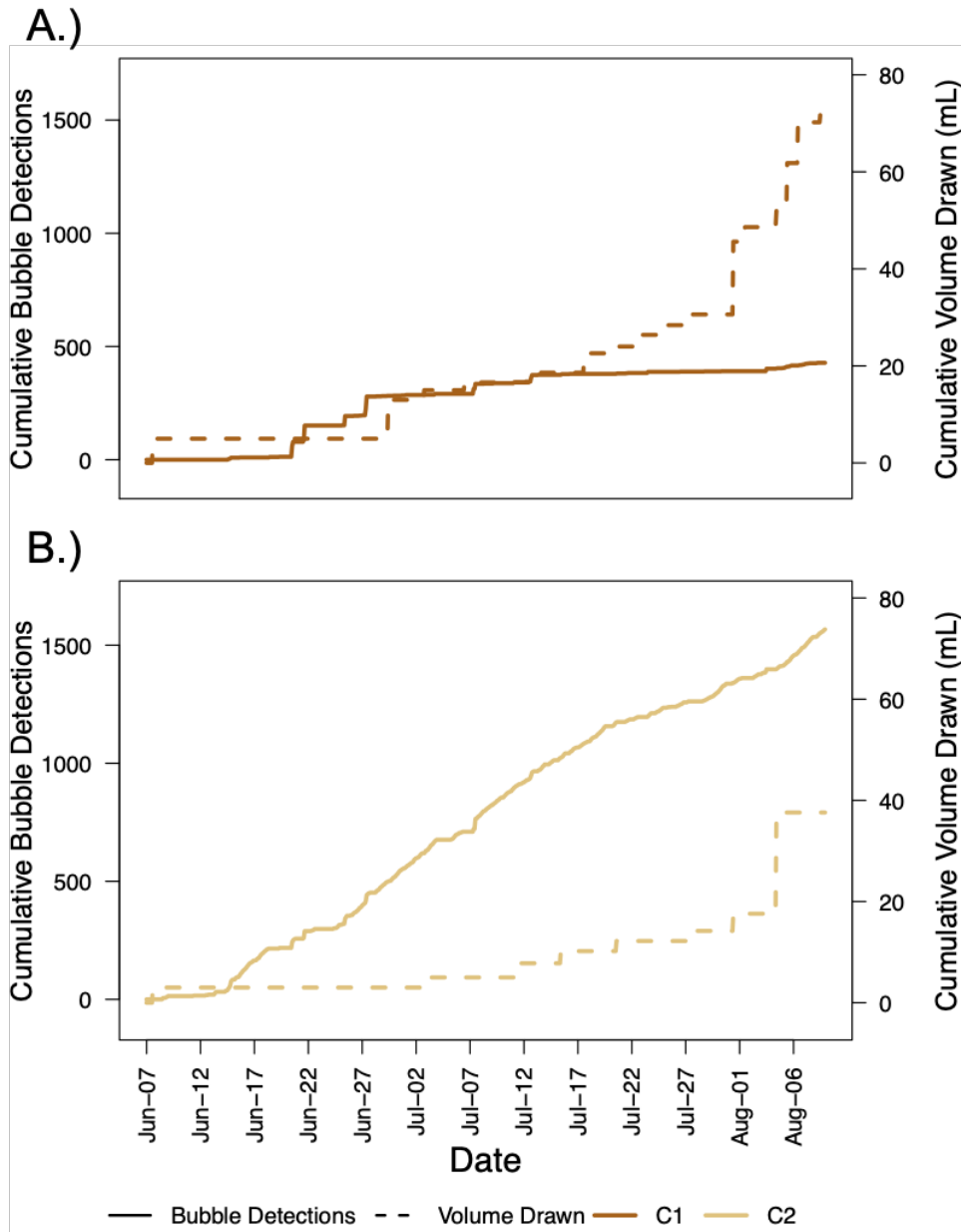


Figure C.4 Timeseries of cumulative bubble detections (solid line) and cumulative volume collected from each bubble trap (dashed line) for trap C1 (panel A.) and trap C2 (panel B.).

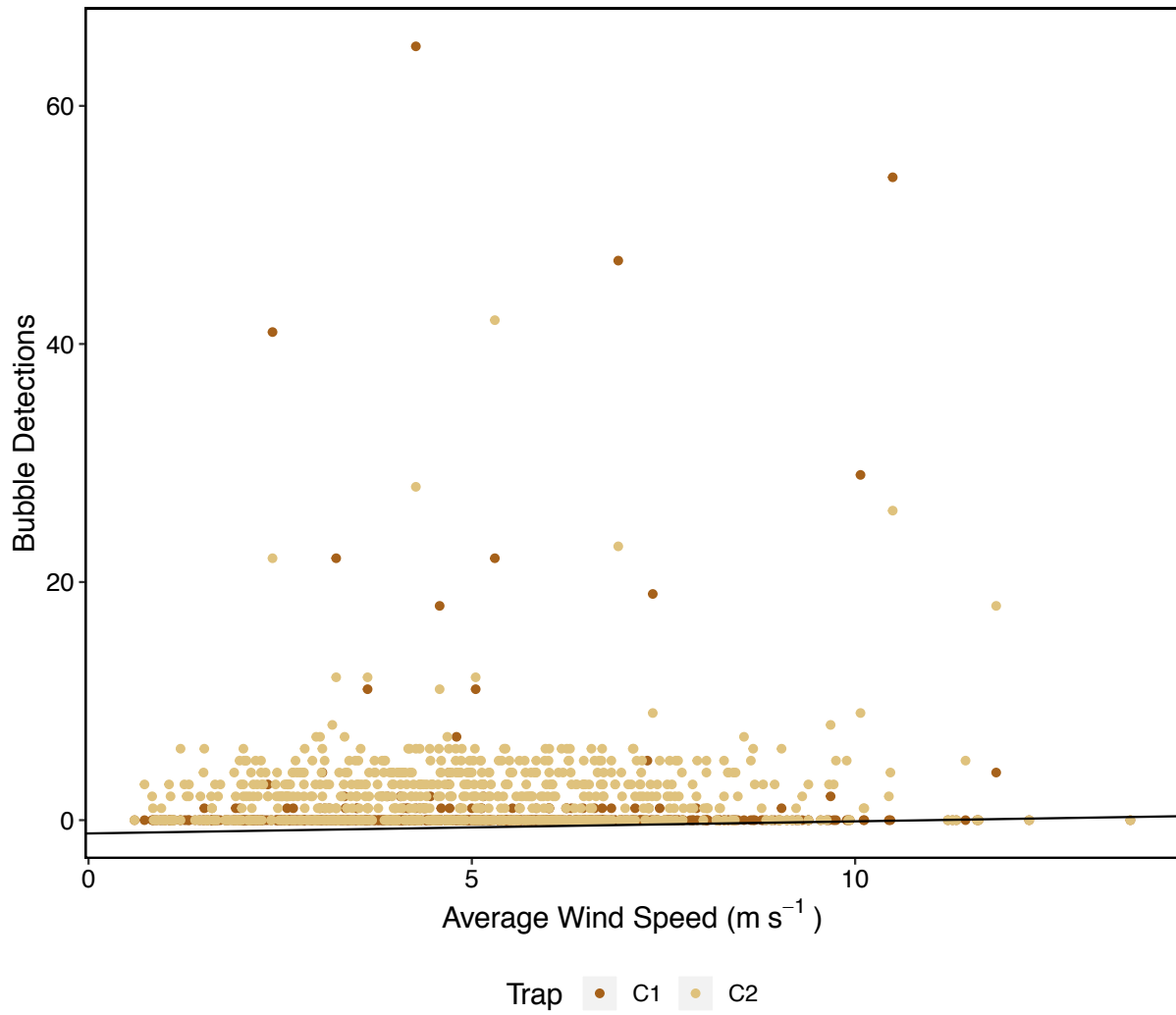


Figure C.5 Scatterplot showing the relationship between bubble detections and average WS (m s⁻²). Detections from each trap are distinguished by color. The solid black line represents the model fit for model 2.

Table C.1 Generalized linear mixed effects results for models 1-5. $R^2_{GLMM(m)}$ is the variance explained by the fixed effects, $R^2_{GLMM(c)}$ is the variance explained by the entire model (fixed + random effects); lognormal approximation was used (MuMIn package; Bartón, 2019). Values with “em dash” are blank due to lack of output for model level p values.

Model	Model Equation	Model Estimate	p value	Random Effects	$R^2_{GLMM(m)}$	$R^2_{GLMM(c)}$
1	BubDet _{2hr} ~ $\beta + k \times \text{trap}$	—	—	(1 doy)	0.36	0.83
	β	-1.7184	<0.0001			
	$k \times \text{trap}$	2.1978	< 0.0001			
2	BubDet _{2hr} ~ $\beta + k \times \text{WS}$	—	—	(1 doy) + (1 trap)	0.01	0.84
	β	-1.11753	0.17101			
	$k \times \text{WS}$	0.10162	0.00225			
3	BubDet _{2hr} ~ $\beta + k \times T_{\text{air}}$	—	—	(1 doy) + (1 trap)	0.1	0.87
	β	-2.06931	0.0129			
	$k \times T_{\text{air}}$	0.11624	< 0.0001			
4	BubDet _{2hr} ~ $\beta + k \times \text{SWR}$	—	—	(1 doy) + (1 trap)	0.04	0.84
	β	-1.0328007	0.196			
	$k \times \text{SWR}$	0.0019412	< 0.0001			
5	BubDet _{2hr} ~ $\beta + k_1 \times T_{\text{air}} + k_2 \times \text{SWR}$	—	—	(1 doy) + (1 trap)	0.09	0.85
	β	-1.8513463	0.025455			
	$k_1 \times T_{\text{air}}$	0.0748452	0.0004			
	$k_2 \times \text{SWR}$	0.0014117	< 0.0001			

Table C.2 Linear model results for models 6. Values with “em dash” are blank due to lack of output for model level estimates or fixed effect level adjusted r² values.

Model	Model Equation	Model Estimate	p value	adjusted R ²
6	$\text{BubDet}_{2\text{hr}} \sim \beta + k \times \text{predBubDet}_{2\text{hr}}$	—	< 0.0001	0.09347
	β	0.74075	< 0.0001	—
	$k \times \text{predBubDet}_{2\text{hr}}$	0.34949	< 0.0001	—